

The Structural and Metamorphic
Evolution of the Neoproterozoic
Basement in Jebel Ja'alan, East Oman

Thesis submitted in accordance with the requirements of the University of
Adelaide for an Honours Degree in Geology

Brandon Luke Alessio

November 2015



THE UNIVERSITY
of ADELAIDE

THE STRUCTURAL AND METAMORPHIC EVOLUTION OF THE NEOPROTEROZOIC BASEMENT IN JEBEL JA'ALAN, EAST OMAN

RUNNING TITLE: NEOPROTEROZOIC EVOLUTION OF JEBEL JA'ALAN

ABSTRACT

Jebel Ja'alan (east Oman) displays some of the best exposed and easternmost basement rock in the country. It comprises metasedimentary and intrusive igneous rocks, interpreted to have been generated within the Mozambique Ocean at the margin of Neoproterozoic India. The metamorphic conditions experienced by the basement and implications these conditions have for tectonic models of the region were, until now, poorly understood. The aim of this paper is to constrain these conditions in order to test the hypothesis that the basement of Jebel Ja'alan formed in a Neoproterozoic volcanic arc and unravel the relationship between the structural and metamorphic evolution of the region.

Phase equilibria modelling constrains peak metamorphic conditions to c. 670–700 °C and 4.5–6 kbar, following a clockwise P – T path. These conditions are not exclusive to an arc environment but are suggested to represent one due to current and previous interpretations of basement formation based on its geochemistry. U–Pb monazite age data of Hassan Schist samples yields a weighted average age of 833 ± 15 Ma, interpreted to be the age of near peak metamorphism, and is supported by ^{40}Ar – ^{39}Ar muscovite age data, which yields a plateau age of 830 ± 6 Ma. The age data collected is shown to be older than that previously gathered for basement in the country's south and is interpreted to represent the Tonian accretion of arc terranes. Mapping of structures in Jebel Ja'alan reveals two phases of deformation, the first involving north-south directed compression, interpreted on the basis of field and petrographic observations to have occurred contemporaneous to or slightly after peak metamorphism. The second phase of deformation involved east-west directed compression, timing of this is difficult to constrain though the reported presence of similar structures within the overlying sedimentary rock suggests the deformation occurred after the Maastrichtian.

KEYWORDS

Structure; Metamorphism; Geochronology; Pseudosection; Oman; Arabian-Nubian Shield; Jebel Ja'alan; Neoproterozoic

TABLE OF CONTENTS

List of Figures and Tables	3
Introduction	7
Geological Setting	10
Arabian-Nubian Shield and Oman	10
Geology of Oman and Jebel Ja'alan	11
Methods	14
Geochronology	14
LA-ICP-MS in-situ monazite U-Pb geochronology	14
⁴⁰ Ar– ³⁹ Ar muscovite geochronology	15
Bulk-rock and mineral geochemistry	15
Bulk-rock geochemistry using X-Ray Fluorescence (XRF).....	15
Mineral chemistry via electron microprobe.....	16
Phase equilibria modelling	16
Petrography.....	16
Pressure–temperature pseudosections	16
Structural geology	18
Stereographic projections	18
Observations and Results	18
Stratigraphic units.....	18
Structural geology	21
Structural map and cross sections.....	21
Stereonet	25
Geochronology	26
LA-ICP-MS in-situ monazite U-Pb geochronology	26
⁴⁰ Ar– ³⁹ Ar muscovite geochronology	30
Metamorphic geology.....	32
Petrology.....	32
Hassan Schist.....	34
Ali Gneiss	35
Mineral chemistry.....	35
Temperature–Amount Pseudosections	41
Temperature–Amount (Fe ₂ O ₃) Pseudosections	42
Temperature–Amount (H ₂ O) Pseudosections	45
Pressure–temperature pseudosections	48

Discussion.....	53
Pressure–Temperature–time evolution	53
Thermal Gradient and Tectonic Setting.....	56
Structural regime and timing	57
Implications for the Arabian-Nubian Shield and Omani basement.....	58
Conclusions	64
Acknowledgments	65
References	65
Appendix A: Sample summary.....	69
Appendix B: Geochronology	70
Appendix C: Bulk rock and mineral geochemistry	83
Appendix D: Phase equilibria modelling	105
Appendix E: Structural geology	105

LIST OF FIGURES AND TABLES

Figure 1. Location map of Jebel Ja'alan, with study area indicated by the black dashed box and roads indicated by the red dashed lines. Red areas represent Neoproterozoic crystalline basement, while blue areas represent Phanerozoic sedimentary cover sequences. Inset (adapted from Shackleton and Ries (1990)) shows the greater east Oman area, location of outcropping basement rock within the region, and location of Jebel Ja'alan within Oman (adjacent to red star).....	9
Figure 2. Field photographs from the study area. a) Parasitic folding of Hassan Schist with limb, axial plane, and hinge measurements displayed; b) Hassan Schist showing large observable change in foliation direction; c) Deformed face of Ali Gneiss, displaying small scale folding of a pre-existing gneissic foliation; d) Rock face of Ali Gneiss perpendicular to the one shown in c), containing a sigma clast that indicates a top to the northeast sense of movement.....	20
Figure 3. Structural and lithological map of the study area. The area is located 50km south of Sur and 15km north of Jalan Bani Buali, within Jebel Ja'alan, east Oman. Grid references refer to WGS84 datum (Zone 40N) and UTM coordinates. Average U–Pb monazite ages are displayed within boxes and are shown on the map proximal to the location where the corresponding sample was taken. Accompanying lithological descriptions are provided in Table 2, while accompanying cross sections are provided in Figure 4. Sampling localities, with accompanying coordinates are provided in Appendix A.	22
Figure 4. North-south (top right) and west-east (bottom) cross sectional diagrams of Jebel Ja'alan study area, with geological map (top left). Subsurface foliation direction, interpreted from field measurements is indicated by dashed grey lines. North-south cross section shows Ali Gneiss being thrust over Hassan Schist, with interpreted subsurface intrusion of Kamil Granodiorite. West-east cross section shows Hassan Schist being thrust over Ali Gneiss, with intrusions of Ja'alan Granite.....	24
Figure 5. Stereographic projections (Lower hemisphere, equal area) of structural features for domains in the Jebel Ja'alan study area. a) Dip and dip-direction of Hassan Schist foliations plotted as great circles (grey) and poles (black). Profile plane and pole is shown in red; b) Dip and dip-direction of Hassan Schist axial planes (minor folds) plotted as great circles; c) Plunge and plunge direction of Hassan Schist aggregate mineral lineations plotted as points; d) Dip and dip-direction of Ali Gneiss foliations plotted as great circles (grey) and poles (black). Profile plane and pole is shown in red; e) Dip and dip-direction of Ali Gneiss axial planes (minor folds) plotted as great circles; f) Dip and plunge direction of Ali Gneiss aggregate mineral lineations plotted as points.	25
Figure 6. Mineral Liberation Analysis (MLA) thin section map of sample JA15-06, showing a backscattered electron mosaic of the sample (left), and MLA map of the sample (right). The map shows that monazite is present within the matrix of the sample, rather than as inclusions. Also note that minerals in the interpreted peak assemblage of qtz–pl–ms–sil–bt–ilm–mt ± st can all be observed to have been subjected to deformation.....	28
Figure 7. U–Pb Concordia diagrams for monazite grains with a 2σ data point error ellipses. Individual data points are indicated by blue ellipses. Samples correspond to: a) Hassan Schist (JA15-04) with weighted mean ²⁰⁶ Pb/ ²⁰⁷ Pb age of 845 ± 19 Ma; b) Hassan Schist (JA15-06) with weighted mean ²⁰⁶ Pb/ ²³⁸ U age of 830.1 ± 7.3 Ma; c)	

Hassan Schist (JA15-40) with weighted mean $^{206}\text{Pb}/^{238}\text{U}$ age of 838 ± 11 Ma, obtained by excluding two young analyses interpreted to represent either radiogenic Pb loss or a limited phase of monazite growth; d) Hassan schist (JA15-43) with no weighted mean calculated due to low number (N=3) of grain analyses. 29

Figure 8. Probability density plot for monazite grains found within Hassan Schist. Ages are plotted as: a) $^{206}\text{Pb}/^{207}\text{Pb}$, weighted average of 845 ± 19 Ma; b) $^{206}\text{Pb}/^{238}\text{U}$, weighted average of 830.1 ± 7.3 ; c) $^{206}\text{Pb}/^{238}\text{U}$ weighted average of 838 ± 11 ; d) $^{206}\text{Pb}/^{238}\text{U}$, with no weighted average calculated due to low number (N=3) of grain analyses. 30

Figure 9. ^{40}Ar - ^{39}Ar muscovite age data plot for Ja'alan Granite sample JA15-03. The sample displays a weighted average plateau age of 831 ± 15 Ma (MSWD 0.30), which is interpreted as the crystallisation age of the granite. 31

Figure 10. ^{40}Ar - ^{39}Ar muscovite age data plot for Ja'alan Granite sample JA15-04. The sample displays a weighted plateau age of 830 ± 6 Ma (MSWD 0.22). 32

Figure 11. Photomicrographs of petrological relationships within the Hassan Schist and Ali Gneiss units. a) JA15-04 (Hassan Schist) showing fabric defined by biotite and muscovite, biotite and muscovite in contact with quartz, and inclusions of biotite within quartz. b) JA15-06 (Hassan Schist) showing large muscovite grains, interpreted to form part of the peak assemblage, sillimanite rosettes, separation of muscovite and sillimanite by quartz, and the replacement of large muscovite grains with very fine muscovite grains, interpreted to signify the breakdown of muscovite. c) JA15-06 (Hassan Schist) showing staurolite within the muscovite-biotite-quartz-sillimanite matrix, sillimanite rosettes, and fabric defined by biotite and muscovite. d) JA15-36 (Ali Gneiss) showing inclusions of biotite and muscovite within quartz, replacement of large muscovite grains with finer muscovite grains, crosshatch twinning in plagioclase, and separation of biotite and muscovite by quartz. e) JA15-36 (Ali Gneiss) showing fabric defined by muscovite, biotite and sillimanite, inclusions of biotite within quartz, inclusions of quartz within biotite and muscovite, and replacement of large muscovite grains with finer muscovite grains. f) JA15-36 (Ali Gneiss) showing separation of biotite and plagioclase by quartz, and replacement of large muscovite grains with finer muscovite grains. g) JA15-41 (Hassan Schist) showing replacement of large muscovite grains with finer muscovite grains, sillimanite rosettes, and separation of muscovite and sillimanite by quartz. h) JA15-43 (Hassan Schist) showing fabric defined by biotite, muscovite and sillimanite wrapping around quartz and larger muscovite grains, plagioclase featuring simple twinning and quartz inclusions, and randomly oriented biotite separated by quartz. i) JA15-43 (Hassan Schist) showing a strong fabric defined by biotite, muscovite and sillimanite which wraps around quartz grains, replacement of large muscovite grains with finer muscovite grains, separation of muscovite and biotite by quartz, and inclusions of quartz in biotite. Abbreviations from Whitney and Evans (2010). 33

Figure 12. Microprobe image showing the compositional transect undertaken on a garnet grain in Hassan Schist sample JA15-41. Accompanying end-member cation values are provided in Table 4. 38

Figure 13. Microprobe image showing the compositional transect undertaken on a garnet grain in Hassan Schist sample JA15-43. Accompanying end member cation values are provided in Table 5. 40

Figure 14. T - M_{O} pseudosection for sample JA15-36. Compositions given are in mol%. The red line represents the Fe_2O_3 value used for P - T modelling of sample JA15-36. ... 42

Figure 15. T - M_{O} pseudosection for sample JA15-04 (and by proxy JA15-43). Compositions given are in mol%. The red line for JA15-04 represents the Fe_2O_3 value

used for P - T modelling of sample JA15-04, while the blue line represents the Fe_2O_3 value used for P - T modelling of sample JA15-43. 43

Figure 16. T - $M_{\text{H}_2\text{O}}$ pseudosection calculated for samples JA15-04. Compositions given are in mol%. The red line represents the H_2O value used for P - T modelling of sample JA15-04. Abundance contours for muscovite and biotite are plotted within the interpreted peak field, and show that this assemblage is compositionally relatively insensitive to the amount of H_2O present. 45

Figure 17. T - $M_{\text{H}_2\text{O}}$ pseudosection calculated for samples JA15-43. Compositions given are in mol%. The red line represents the H_2O value used for P - T modelling of sample JA15-43. 46

Figure 18. T - $M_{\text{H}_2\text{O}}$ pseudosection calculated for samples JA15-36. Compositions given are in mol%. The red line represents the H_2O value used for P - T modelling of sample JA15-36. 47

Figure 19. Calculated P - T pseudosection for sample JA15-04 from Hassan Schist. Bulk composition used for modelling is given in the top of the diagram and expressed as mole%. The field muscovite–biotite–ilmenite–plagioclase–magnetite–sillimanite–quartz– H_2O indicates the peak assemblage, with the dashed white oval indicating inferred peak P - T conditions based on the measured chemistry of muscovite. Interpreted prograde and retrograde P - T paths are shown by the grey arrows, with a solid line indicating increased confidence of path trajectory. Coloured dashed lines represent compositional variable contours of muscovite $x(\mu)$ ($= \text{Fe}^{2+}/(\text{Fe}^{2+} + \text{Mg})$ cations), $y(\mu)$ ($= \text{Al}^{\text{VI}}$) and biotite $y(\text{bi})$ ($= \text{Al}^{\text{VI}}$). 49

Figure 20. Calculated P - T pseudosection for sample JA15-43 from Hassan Schist. Bulk composition used for modelling is given in the top of the diagram and expressed as mole percent. The field muscovite–biotite–ilmenite–plagioclase–magnetite–sillimanite–garnet–quartz– H_2O corresponds to the peak assemblage, with the dashed white oval indicating inferred peak P - T conditions. Interpreted prograde and retrograde P - T paths are shown by the grey arrows, with a solid line indicating increased confidence of path trajectory. Coloured dashed lines represent compositional variable contours of muscovite $x(\mu)$ ($= \text{Fe}^{2+}/(\text{Fe}^{2+} + \text{Mg})$ cations), $y(\mu)$ ($= \text{Al}^{\text{VI}}$) and garnet $x(\text{g})$ ($= \text{Fe}^{2+}/(\text{Fe}^{2+} + \text{Mg})$ cations). 50

Figure 21. Calculated P - T pseudosection for sample JA15-36 from Ali Gneiss. Bulk composition used for modelling is given in the top of the diagram and expressed as mole percent. The field muscovite–biotite–sillimanite–ilmenite–plagioclase–K-feldspar–quartz–melt indicates the peak assemblage. The interpreted retrograde P - T path is shown by the grey arrow. Coloured dashed lines represent compositional variable contours of muscovite $x(\mu)$ ($= \text{Fe}^{2+}/(\text{Fe}^{2+} + \text{Mg})$ cations), $y(\mu)$ ($= \text{Al}^{\text{VI}}$) and biotite $y(\text{bi})$ ($= \text{Al}^{\text{VI}}$). 52

Figure 22. Summary of interpreted P - T paths from the Arabian-Nubian Shield, Oman, and locations related to the Mozambique belt. Paths are displayed upon background adapted from (Brown 2007a). Abbreviations: BS = blueschist; AEE = amphibole-epidote-eclogite facies; E-HPG = eclogite-high-pressure granulite; G = granulite facies; UHTM = ultrahigh-temperature metamorphic part of the granulite facies. P - T path references: Saudi Arabia: Abu-Alam *et al.* (2014); Kenya: Hauzenberger *et al.* (2004); Tanzania: Herms and Schenk (1998); Zambia: John *et al.* (2004); Southern India (a): Collins *et al.* (2007); Southern India (b): Brandt *et al.* (2011); Egypt (c): Fritz *et al.* (2002); Egypt (d): Abu El-Enen (2011). 61

Figure 23. Time-space plot for Terranes in the Arabian-Nubian Shield and locations within Oman, with a gap between locations signifying a >800 km gap between the closest basement outcrops. A location map of terranes displayed in the plot is presented in Figure 24. It can be observed that both protolith ages and timing of suturing of terranes decreases to the modern day east of the ANS, reflecting amalgamation of younger arc terranes. The opposite trend can be seen within the Omani basement, with ages decreasing towards the modern day west. Furthermore, it can also be seen that accretion in Oman finished earlier than in the ANS, reflected in the earlier deposition of sediments. Ages in the ANS are from Johnson *et al.* (2011), Mirbat ages from

Rantakokko <i>et al.</i> (2014)	62
Figure 24. Location map of the Arabian-Nubian Shield (ANS) and Oman (adapted from Blades <i>et al.</i> (2015)). The map shows terranes and locations used for the time-space plot presented in Figure 23.	63
Table 1. Summary of previous geochronological data for crystalline basement lithologies within Oman, adapted from (Rantakokko <i>et al.</i> 2014). Ages in Ma \pm 2 σ . WR: Whole rock, Mineral abbreviations from (Whitney & Evans 2010). References: a) (Bowring <i>et al.</i> 2007); b) (Mercolli <i>et al.</i> 2006); c) (Rantakokko <i>et al.</i> 2014); d) (Gass <i>et al.</i> 1990); e) (Worthing 2005).....	13
Table 2. Summary and description of lithologies in the Jebel Ja'alan study area.....	23
Table 3. Average mineral chemistry values measured for biotite, muscovite, and garnet in samples used in phase diagram calculations accompanied by relevant average compositional variable values.....	37
Table 4. End-member cation values for spot analyses in the compositional transect of a garnet grain in Hassan Schist sample JA15-41.....	39
Table 5. End-member cation values for spot analyses in the compositional transect of a garnet grain in Hassan Schist sample JA15-43.....	41

INTRODUCTION

Jebel Ja'alan (east Oman) is one of few discrete exposures of basement in the country. These exposures preserve complex histories of magmatic, metamorphic and deformational events (Gass *et al.* 1990, Mercolli *et al.* 2006, Rantakokko *et al.* 2014) that offer an insight into palaeogeography of the region during the Neoproterozoic, a time of significant Earth evolution (e.g. Collins & Pisarevsky 2005, Meert & Lieberman 2008, Pisarevsky *et al.* 2008). Based upon its geochemistry, many authors have interpreted an intra-oceanic volcanic arc setting for the basement of Oman (Gass *et al.* 1990, Mercolli *et al.* 2006, Bowring *et al.* 2007, Rieu *et al.* 2007, Rantakokko *et al.* 2014), with suggestions that these arcs formed within the Mozambique Ocean, proximal to or at the margin of Neoproterozoic India (Johnson & Woldehaimanot 2003, Kröner & Stern 2004, Rantakokko *et al.* 2014). While geochemical data for the Omani basement are suggestive of a volcanic arc setting, no studies have yet attempted to constrain the metamorphic conditions experienced by the basement during formation. Metamorphic rocks record the pressure–temperature–time evolution (P – T – t path) of the crust, which may be characterised as the thermal gradient a rock has experienced during metamorphism. Thermal gradients can differentiate between a number of different tectonic settings and thus can be used to constrain the particular setting a given rock was in (Brown 2007b). Such fundamental information is critical for testing hypotheses regarding both the tectonic setting of the basement during formation, and the relationship between the Omani basement and Arabian-Nubian Shield.

This study primarily aims to constrain the conditions and timing of metamorphism of metasedimentary units in the Jebel Ja'alan area, east Oman (Fig. 1), in order to test the

hypothesis that the region represented a Neoproterozoic volcanic arc and unravel the relationship between the structural and metamorphic evolution of the region. Pressure–temperature (P – T) conditions will be interpreted via thermodynamic modelling of metamorphic mineral assemblages, assisted by mineral chemistry data. The timing of metamorphism will be constrained from both ^{40}Ar – ^{39}Ar muscovite and in-situ U–Pb monazite geochronological data. Furthermore, this study aims to determine the nature and relative timing of structures in the Jebel Ja'alan basement, in order to develop a more detailed framework of understanding for the area. Structural and lithological mapping in conjunction with cross sectional diagrams and stereographic projections will be used to determine the nature of structures in the Jebel Ja'alan area. The relative timing of structures will be interpreted using the aforementioned geochronological data. The results of this study will be interpreted in the context of the tectonic evolution of Oman, Gondwana and the evolution of the Indian Ocean.

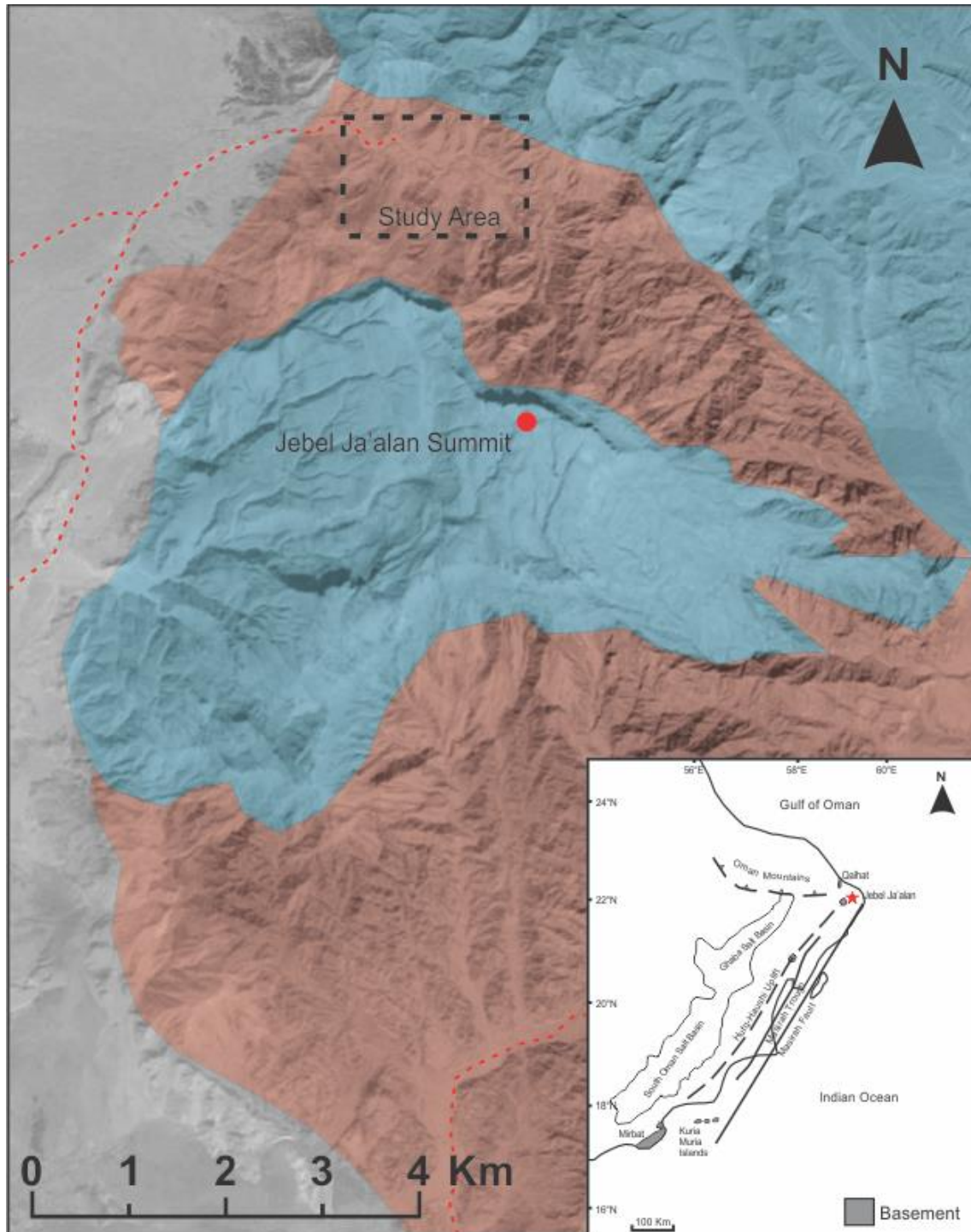


Figure 1. Location map of Jebel Ja'alan, with study area indicated by the black dashed box and roads indicated by the red dashed lines. Red areas represent Neoproterozoic crystalline basement, while blue areas represent Phanerozoic sedimentary cover sequences. Inset (adapted from Shackleton and Ries (1990)) shows the greater east Oman area, location of outcropping basement rock within the region, and location of Jebel Ja'alan within Oman (adjacent to red star).

GEOLOGICAL SETTING

Arabian-Nubian Shield and Oman

Several authors have recognised the similarities between the basement rocks of Oman, with that of Yemen and the Arabian-Nubian Shield (ANS). Many of these authors have suggested that Oman represents an eastern extension of the ANS (Gass *et al.* 1990, Collins & Pisarevsky 2005, Worthing 2005, Stern & Johnson 2010, Rolandone *et al.* 2013, Rantakokko *et al.* 2014), which was described by Johnson *et al.* (2011) as a collage of Neoproterozoic juvenile arcs, younger sedimentary and volcanic basins, granitoid intrusions, and enclaves of pre-Neoproterozoic crust. Though it is important to note that the absence of basement outcrop between Oman and the Arabian Shield of Saudi Arabia prevent any direct connection between the two (Johnson & Woldehaimanot 2003, Collins & Pisarevsky 2005, Rantakokko *et al.* 2014). Crustal growth of the ANS is interpreted to have occurred from c. 870–600 Ma (Johnson & Woldehaimanot 2003, Meert 2003, Kröner & Stern 2004, Stern & Johnson 2010), with volcanic arcs being formed on the relatively juvenile crust of the Mozambique Ocean. (Johnson & Woldehaimanot 2003, Meert 2003, Kröner & Stern 2004, Rantakokko *et al.* 2014). Amalgamation of these arc terranes and associated ophiolitic remnants, which form the majority of the ANS, is believed to have occurred as early as 800 Ma (Johnson & Woldehaimanot 2003, Meert 2003), via arc-arc convergence and terrane suturing (Johnson & Woldehaimanot 2003). It is interpreted that the age of the arc terranes decreases to the east of the modern day ANS (Johnson *et al.* 2011). These terranes that comprise the ANS are thought to have accreted onto the East Saharan craton during the late Cryogenian-Ediacaran (Meert 2003, Li *et al.* 2008, Johnson *et al.* 2011). This later accretion is in contrast to Omani basement, though similar processes are interpreted to

have occurred within Oman, they are thought to have ceased in the Cryogenian (Mercolli *et al.* 2006, Rantakokko *et al.* 2014). Instead while accretion in the ANS continued during the late Neoproterozoic, we see deposition of relatively undeformed sedimentary sequences in Oman at this time (Allen 2007, Rieu *et al.* 2007) suggested to represent a rift sequence followed by a passive margin succession (Allen 2007).

Geology of Oman and Jebel Ja'alan

Jebel Ja'alan is located in Oman's northeast, approximately 50 km south of the town of Sur (Fig. 1). The basement rocks throughout Oman outcrop in only a few places (Fig. 1), though lithologies are similar in the different inliers. It is possible to observe in most of the basement inliers greenschist to amphibolite facies metamorphic rocks that are complexly deformed and intruded by dioritic to granitic rock, which have then been cut by dyke swarms (Gass *et al.* 1990, Johnson & Woldehaimanot 2003, Mercolli *et al.* 2006, Allen 2007, Rantakokko *et al.* 2014). Additionally the areas of basement within Oman display different yet reliable ages as shown in Table 1. Rieu *et al.* (2007) mentions U–Pb ages of granite intrusions in Jebel Ja'alan ranging from 830–825 Ma, while Stern and Johnson (2010) note that Jebel Ja'alan contains basement rock coeval or slightly older than what is interpreted for basement in the better studied Mirbat region (Table 1). Jebel Ja'alan forms a north-south trending structural high as indicated by Immenhauser *et al.* (2000) and Filbrandt *et al.* (1990). It is interpreted by Filbrandt *et al.* (1990) as the northern expression of the Huqf-Haushi uplift, a NNE-SSW trending crustal arc (Fig. 1), postulated to have formed from obduction of Oman's eastern ophiolites (Ries & Shackleton 1990, Immenhauser *et al.* 2000), which terminates against the North Ja'alan fault (Worthing 2005). The basement rock exposed in Jebel Ja'alan is unconformably overlain by younger sediments ranging from Cretaceous to

Eocene in age (Filbrandt *et al.* 1990). These sediments are suggested by Würsten *et al.* (1991) to have been deposited after Late Cretaceous denudation of the basement.

Table 1. Summary of previous geochronological data for crystalline basement lithologies within Oman, adapted from (Rantakokko *et al.* 2014). Ages in Ma \pm 2 σ . WR: Whole rock. Mineral abbreviations from (Whitney & Evans 2010). References: a) (Bowring *et al.* 2007); b) (Meccolli *et al.* 2006); c) (Rantakokko *et al.* 2014); d) (Gass *et al.* 1990); e) (Worthing 2005).

Region	Lithology	TNd	Sm/Nd	U/Pb age	K/Ar age	Rb/Sr age	Pb/Pb age	Reference
<i>Mirbat</i>	<i>Late intrusives</i>							
	Mirbat dyke		757 \pm 61			655 \pm 89		e
	Leger Granite			726 \pm 1				a
	Pegmatitic vein in basement			809 \pm 1				a
	Pegmatite dyke					799 \pm 24 (Ms)		b
	Granite to pegmatite dyke					743 \pm 7 (Ms)	725 \pm 41 (Grt)	b
	<i>Tonalite complexes</i>							
	Fusht tonalitic gneiss	960		783 \pm 7			788 \pm 27 (Pl)	b
	Hadbin leucocratic tonalite	940		786 \pm 6			795 \pm 13 (Ttn)	b
	Hadbin leucocratic tonalite				788 \pm 13			b
	<i>Sadh complex</i>							
	Banded gneiss				813 \pm 12			b
	Banded biotite gneiss	910		816 \pm 12				b
	Mahall Hbl-bearing Bt-gneiss	950		799 \pm 7				b
	<i>Juffa complex</i>							
	Two mica gneiss	1040		812 \pm 10		828 \pm 13 (WR)	809 \pm 17 (Grt)	b
	Granitic gneiss			831 \pm 7				c
	Biotite gneiss			821 \pm 16				c
	Hbl gabbro/diorite			796 \pm 14				c
	Intermediate Gneiss			816 \pm 5				c
<i>Jebel Ja'alan</i>	Igneous suite					850 \pm 27		d
	Ali Gneiss					773 \pm 34		d
	Mafic Dyke				430 \pm 20			d
<i>Kuria Muria Islands</i>	Igneous suite					772 \pm 8		d

METHODS

Seventeen samples were collected from the Jebel Ja'alan area in eastern Oman, with a sampling strategy outlined in Appendix A. This was done in conjunction with structurally mapping a 5x10 km area of the region and producing accompanying cross sections.

Geochronology

LA-ICP-MS IN-SITU MONAZITE U–PB GEOCHRONOLOGY

U–Pb age data were obtained from in-situ monazite grains from four thin section samples. The thin sections and grains were imaged on a Phillips XL30 Scanning Electron Microscope (SEM) and then analysed via LA-ICP-MS, using an Agilent 7500cs and NewWave UP213 Laser Ablation System. Ablation of monazites was performed in a He-Ablation atmosphere with a frequency of 5 Hz. A spot size of 10 μm was used for all samples. The acquisition time for all samples was 80 seconds total, with 30 seconds of background acquisition, 10 seconds of the laser firing with the shutter close to ensure beam stabilisation, and 40 seconds of sample ablation. Isotopes measured were ^{204}Pb , ^{206}Pb , ^{207}Pb , and ^{238}U for dwell times of 10, 15, 30, and 15ms, respectively. Age estimates for grains were obtained using the program *GLITTER* (Jackson *et al.* 2004). Elemental fractionation and mass bias were corrected using the monazite MADEL (TIMS normalisation data: $^{207}\text{Pb}/^{206}\text{Pb} = 491 \pm 2.7 \text{ Ma}$, $^{206}\text{Pb}/^{238}\text{U} = 518.37 \pm 0.99 \text{ Ma}$, $^{207}\text{Pb}/^{235}\text{U} = 513.13 \pm 0.19 \text{ Ma}$; Payne *et al.* 2008). Data accuracy was monitored using monazite standard 94-222/Bruna-NW (c. 450 Ma; Payne *et al.* 2008). Throughout this study MADEL yielded weighted mean ages of $^{207}\text{Pb}/^{206}\text{Pb} = 492 \pm 14 \text{ Ma}$, $^{206}\text{Pb}/^{238}\text{U} = 518 \pm 5.2 \text{ Ma}$, $^{207}\text{Pb}/^{235}\text{U} = 513 \pm 4.8 \text{ Ma}$ (n=29). As a secondary

standard, 94-222 yielded weighted mean ages of $^{207}\text{Pb}/^{206}\text{Pb} = 464 \pm 16 \text{ Ma}$, $^{206}\text{Pb}/^{238}\text{U} = 443 \pm 5.1 \text{ Ma}$, $^{207}\text{Pb}/^{235}\text{U} = 445 \pm 5.2 \text{ Ma}$ (n=25).

^{40}Ar – ^{39}Ar MUSCOVITE GEOCHRONOLOGY

Four samples of muscovite were used for ^{40}Ar – ^{39}Ar dating. Grains were separated using a paper shaking technique (Appendix B), then hand-picked and sent to the Western Australian Argon Isotope Facility, Curtin University, Perth, Western Australia. Samples were loaded into wells and bracketed by small wells that included Fish Canyon sanidine (FCs) used as a neutron monitor for which an age of $28.305 \pm 0.036 \text{ Ma}$ (1σ) was assigned based on the calibrations by Jourdan and Renne (2007) and Renne *et al.* (2010). The samples were irradiated in the Hamilton McMaster University nuclear reactor (Canada). The correction factors for interfering isotopes were $(^{39}\text{Ar}/^{37}\text{Ar})\text{Ca} = 7.30 \times 10^{-4}$ ($\pm 11\%$), $(^{36}\text{Ar}/^{37}\text{Ar})\text{Ca} = 2.82 \times 10^{-4}$ ($\pm 1\%$) and $(^{40}\text{Ar}/^{39}\text{Ar})\text{K} = 6.76 \times 10^{-4}$ ($\pm 32\%$). Samples were step heated using a 110W Spectron Laser Systems, with a continuous Nd-YAG (IR: 1064 nm) laser. Ar isotopes were measured in static mode using a MAP 215-50 mass spectrometer, with a Balzers SEV 217 electron multiplier primarily using nine to ten cycles of peak-hopping.

Bulk-rock and mineral geochemistry

BULK-ROCK GEOCHEMISTRY USING X-RAY FLUORESCENCE (XRF)

Whole-rock geochemical analyses for phase equilibria modelling of two samples were undertaken using XRF analysis at Bureau Veritas Minerals, Perth, Western Australia. Major elements were analysed on fused beads using a lithium tetraborate flux, as described by Kil and Jung (2015). Additionally, two samples were made into fused

disks, following the method outlined in Appendix C. and sent to a CSIRO laboratory, for X-ray Fluorescence (XRF) analysis.

MINERAL CHEMISTRY VIA ELECTRON MICROPROBE

Chemical compositions of muscovite, plagioclase, K-feldspar, garnet and biotite used to further constrain P - T conditions were obtained using a CAMECA SX 5 microprobe following the method outlined in Appendix C. A beam current of 20 nA and accelerating voltage of 15 kV was used for all point analyses.

Phase equilibria modelling

PETROGRAPHY

Seventeen thin sections were made polished and uncovered by Continental Instruments, India (Appendix B). A petrographic analysis was undertaken on each thin section using an Olympus BH-2 optical microscope, with Hassan Schist sample JA15-06 receiving further analysis using a Mineral Liberation Analyser (MLA) attached to a FEI Quanta 600 SEM.

PRESSURE-TEMPERATURE PSEUDOSECTIONS

P - T pseudosections were created using the phase equilibrium modelling program *THERMOCALC* v. 3.37 with the internally consistent thermodynamic dataset of Holland and Powell (2011), ds62. Pseudosections were calculated for the geologically realistic system of MnNCKFMASHTO (MnO–Na₂O–CaO–K₂O–FeO–MgO–Al₂O₃–SiO₂–H₂O–TiO₂–Fe₂O₃). Activity–composition (a-x) models considered come from Powell *et al.* (2014) and White *et al.* (2014). Major element whole rock geochemical compositions obtained using XRF analysis recalculated to molar oxide percent

(Appendix D) were used for modelling. In the following calculations the bulk composition of sample JA15-04 has been used as a proxy for the composition of JA15-43 due to their similarity in preserved mineral assemblage and similarity in measured mineral compositions. Calculations in *THERMOCALC* are based on the user specifying the stable mineral assemblage, then calculating all the individual lines and points, where lines (field boundaries) represent the zero abundance of a phase and points represent the zero abundance of two phases. The initial stable assemblage is determined by performing a Gibbs energy minimisation calculation at a set P - T condition. The diagram is built up and around from that initial assemblage and involves many trial and error calculations in order to determine which phases appear or disappear as a function of pressure, temperature and/or composition. In addition, the so-called 'starting guesses' (values for variables with which *THERMOCALC* commences its iterative least-squares calculation for a line or point) require regular updating as the pseudosection is calculated in different parts of P - T - X space (X = composition). Therefore, a single diagram commonly comprises >100–200 total line and point calculations, and the user is actively (intellectually), rather than passively, involved in all calculations done to create a single diagram (often taking over a week per single diagram). The abundances of H_2O and Fe_2O_3 (oxidation state) in a whole rock geochemical analysis are the most uncertain (e.g. Korhonen et al. 2012; Kelsey & Hand 2015) as they cannot be directly measured during routine geochemical (XRF) analysis (Fitton & Gill 1970, Kelsey & Hand 2015, Morrissey *et al.* 2015). Appropriate H_2O and Fe_2O_3 ('O') contents for P - T pseudosections were evaluated using T - M_O (Figs. 14, 15) and T - M_{H_2O} (Figs. 16, 17, 18) pseudosections, where ' M ' refers to amount. Chosen H_2O and O amounts are shown in Figures 14-18, and were chosen for the P - T modelling of samples as they correspond to

the calculated stability of the interpreted peak metamorphic assemblage observed in the rocks.

Structural geology

STEREOGRAPHIC PROJECTIONS

Lower hemisphere equal area stereographic projections were created for structural data using the *STEREONET 9* program, based on algorithms described by Cardozo and Allmendinger (2013), and Allmendinger *et al.* (2011).

OBSERVATIONS AND RESULTS

Stratigraphic units

Eight lithologies were encountered in the Jebel Ja'alan study area, which are summarised in Table 2. It can be seen in the map presented as Figure 3 that there are two lithologies occupying the majority of the study area, the Hassan Schist and Ali Gneiss (Fig. 3). The Hassan Schist is a metapelite comprised of fine grained (<0.75mm) $qtz-pl-bt-ms-sil-ilm-mt-chl \pm st \pm grt$ with occurrences of coarse grained (1–2mm) $qtz-pl$ and a fabric defined by $bt-ms-sil$. The Ali Gneiss is comprised of fine to medium grained (0.3–1mm) $bt-ms-qtz-pl-sil-ilm-kfs$ with medium to coarse grained (0.7–3mm) qtz . The protolith of the Ali Gneiss is uncertain, the inclusion of sillimanite in its mineralogy as well as previous interpretations by Immenhauser *et al.* (2000), suggest it to be a paragneiss. However, Thorpe (2015) observed a predominantly igneous appearance of zircon grains within the Ali Gneiss, with a very low spread of related U–Pb ages attributed to the crystallisation age of an interpreted igneous protolith. Both lithologies show evidence for partial melting having occurred, albeit in

small areas. The Ali Gneiss and Hassan Schist have both been observed to be intruded by granite bodies, designated collectively as the Ja'alan Granite. Additionally, the Hassan Schist has also been observed to host relatively small granodiorite intrusions, which have been designated as the Kamil Granodiorite, and a pair of chl-pl-cpx dolerite dykes running parallel to each other. Small lenses of other units have been observed in the Ali Gneiss, the first of which being a ttn-bt-sil-st \pm ms schist observed in the south of the study area. The second of these units found within the Ali Gneiss is a para-amphibolite, observed in two areas to the south and east of the study area. The basement rock is unconformably overlain by bioclastic limestones of the Simsima formation, interpreted to be of Maastrichtian age (c. 66–72 Ma) by (Filbrandt *et al.* 1990) due to the presence of rudist fossils.

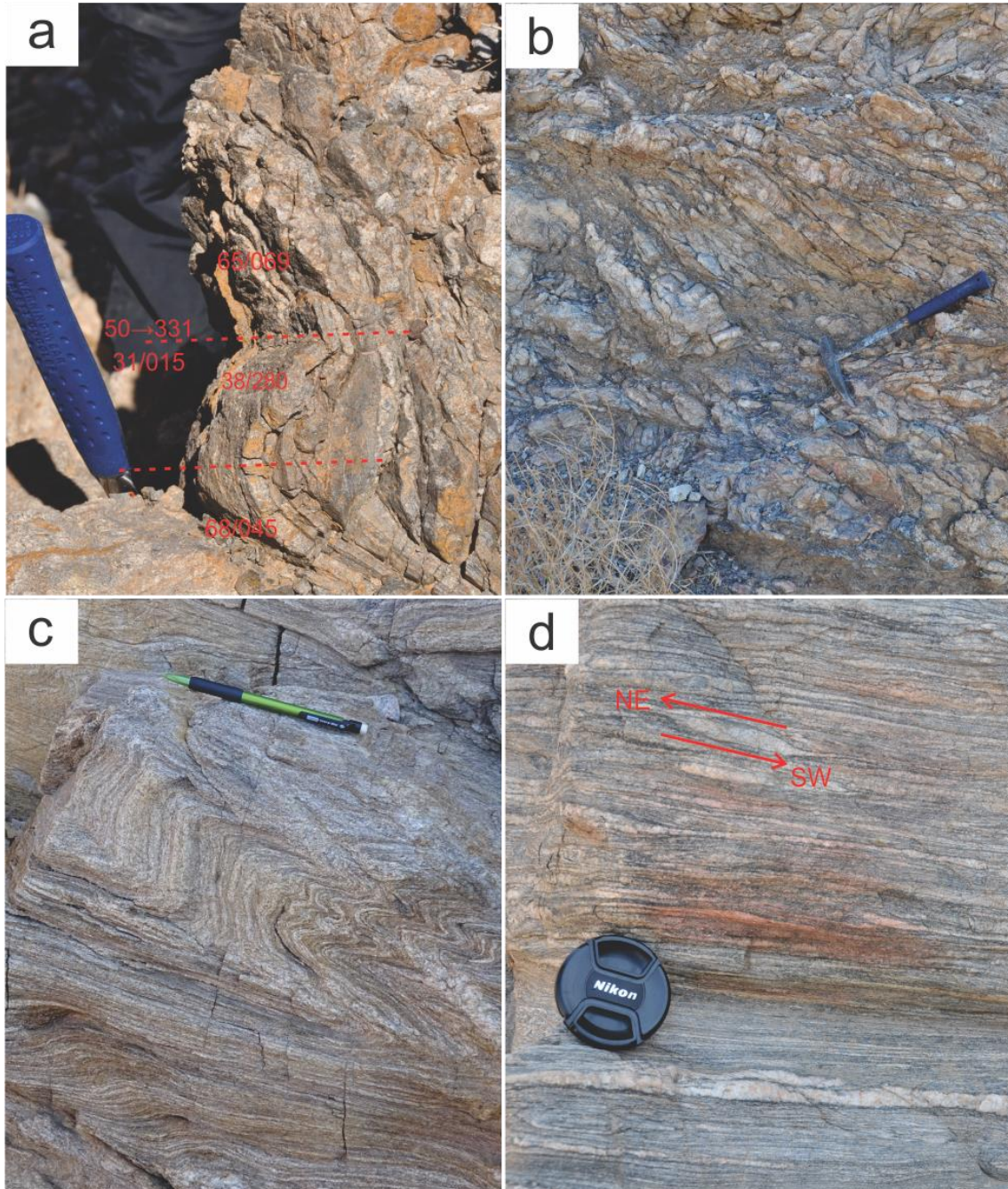


Figure 2. Field photographs from the study area. a) Parasitic folding of Hassan Schist with limb, axial plane, and hinge measurements displayed; b) Hassan Schist showing large observable change in foliation direction; c) Deformed face of Ali Gneiss, displaying small scale folding of a pre-existing gneissic foliation; d) Rock face of Ali Gneiss perpendicular to the one shown in c), containing a sigma clast that indicates a top to the northeast sense of movement.

Structural geology

STRUCTURAL MAP AND CROSS SECTIONS

Structural and lithological data collected from Jebel Ja'alan are presented as both a map (Fig. 3) and cross sections (Fig. 4). Lithological mapping shows two key domains, the first being comprised largely of the Hassan Schist and located to the north and west of the area. The second is comprised primarily of the Ali Gneiss, and is located to the south and east of the mapping area. These domains are structurally juxtaposed, with the Ali Gneiss thrust over the Hassan Schist (Fig. 4) along the east-west boundary between both units. In contrast, it is interpreted that the Hassan Schist is thrust over the Ali Gneiss along the north-south trending boundary of both units (Fig. 4), based upon collected structural data and observed relationships between the domains along the east-west boundary. It can be seen that both structural domains contain intrusions of Ja'alan Granite, while intrusions of Kamil Granodiorite and dolerite have only been observed within the Hassan Schist, though this may be attributed to the relatively small size of these intrusions hindering efforts to find them within gneiss. Furthermore, the structural data are suggestive of two phases of folding. The first of which is interpreted to be a series of approximately east to northeast trending folds, while the second is interpreted, with varying confidence relating to the abundance and attributes of structural data, to be a pair of approximately north-south trending folds.

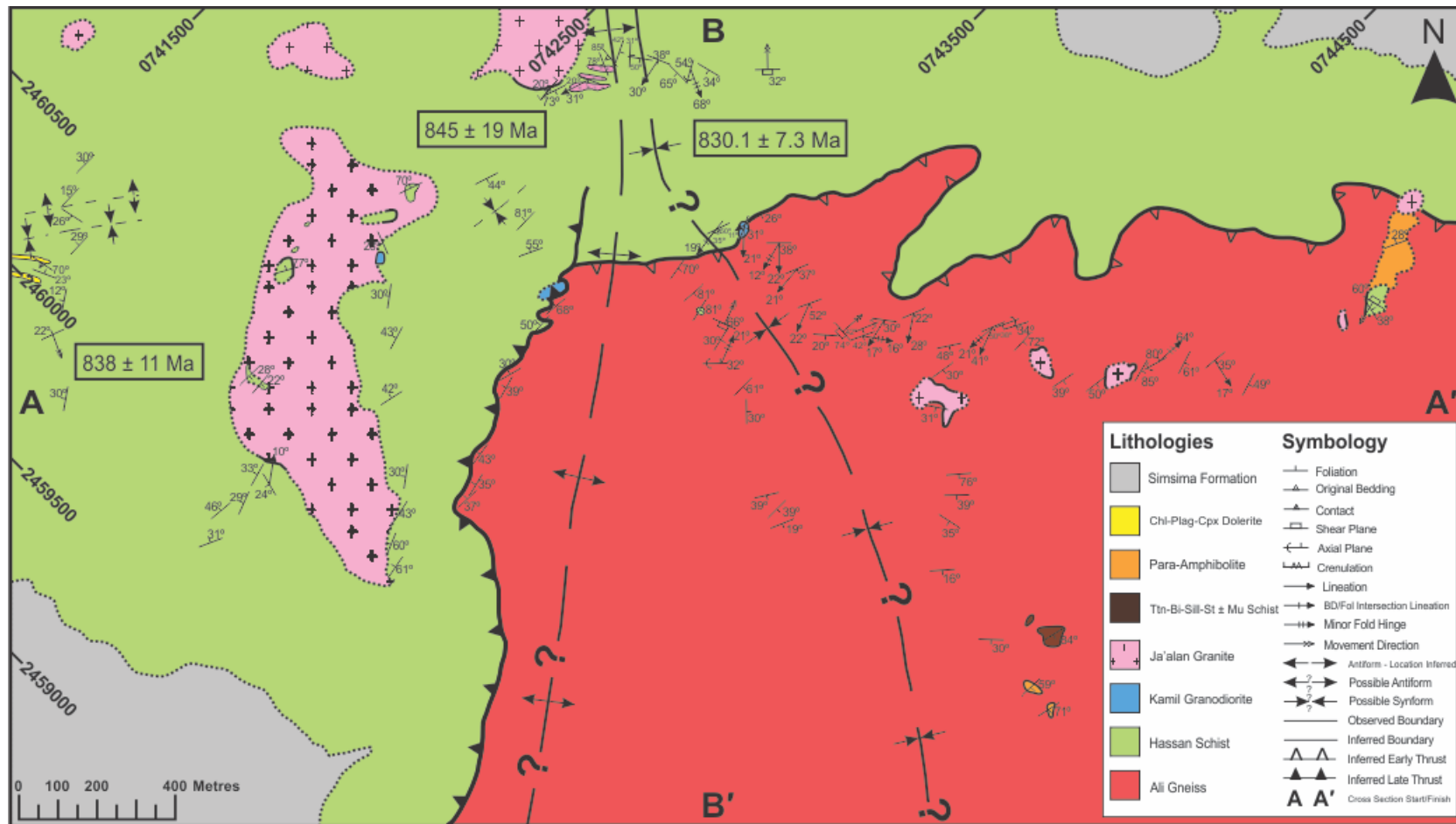


Figure 3. Structural and lithological map of the study area. The area is located 50km south of Sur and 15km north of Jalan Bani Buali, within Jebel Ja'alan, east Oman. Grid references refer to WGS84 datum (Zone 40N) and UTM coordinates. Average U-Pb monazite ages are displayed within boxes and are shown on the map proximal to the location where the corresponding sample was taken. Accompanying lithological descriptions are provided in Table 2, while accompanying cross sections are provided in Figure 4. Sampling localities, with accompanying coordinates are provided in Appendix A.

Table 2. Summary and description of lithologies in the Jebel Ja'alan study area.

Lithological unit	Mineralogy	Textural and structural features	Additional characteristics
Simsima formation (Filbrandt <i>et al.</i> 1990)	Pale yellow to grey bioclastic limestones	-	Rudist fossils and benthonic foraminifera constrain the formation's age as Maastrichtian. Observed to unconformably overlie basement rock in the southwest and north east corners of the mapping area.
Chl-Pl-Cpx Dolerite	Fine to medium grained (.2-1mm) pl-cpx-chl.	Cpx and pl grains are significantly deformed, with few cpx grains displaying a distinct crystal form. Pericline twinning exhibited in several pl grains.	Occurs as dykes which crosscut all other basement lithologies in Jebel Ja'alan region.
Para-Amphibolite	Coarse (1-4mm) hbl (60-70%) -cpx-pl with minor bi.	Reaction texture present indicating breakdown of pl.	Restricted to two outcrops observed within the Ali gneiss in the south and east of the mapping area.
Ttn-bi-sill-st ± mu Schist	Coarse (1-2mm) pl-qtz with medium to fine (.2-1) pl-qtz-st-sil-bt-ttn and minor py-ms.	Pervasive reaction textures present throughout rock showing features indicating breakdown of pl and bt. Ttn grains abundant throughout rock as well-defined and relatively undeformed crystals.	Localised to south of mapping area observed as a single outcrop within the Ali Gneiss.
Ja'alan Granite	Coarse (1-2mm) qtz-pl-kfs-ms-grt.	Coarse, granoblastic texture.	Found dispersed within the mapping area as bodies of various size. Intrude both the Hassan Schist and Ali Gneiss.
Kamil Granodiorite	Coarse grained (1-3mm) qtz-grt-pl with finer (<.75mm) bt-kfs. Coarser (3-5mm) grt phenocrysts are observed in a relatively finer qtz-pl-kfs-bt groundmass.	Coarse overall texture with finer bt and kfs. Reaction texture throughout rock showing the breakdown of pl. Varying degrees of deformation within grt phenocrysts.	Found as small intrusions within the Hassan schist, often bordering the Ali Gneiss.
Hassan Schist	Fine grained (<.75mm) qtz-pl-bt-ms-sil-ilm-mt-chl ± st ± grt with occurrences of coarse grained (1-2mm) qtz and pl. Peak assemblage qtz-pl-ms-sil-bt-ilm-mt ± grt ± st	Fabric defined by bt-ms-sil with an aggregate mineral lineation defined by bt. Schistose foliation present throughout rock with partial melting observed in small areas. Breakdown of muscovite is interpreted from thin-section samples.	Metapelitic unit which occupies a large portion of the north and western mapping area. Inferred to thrust over the Ali gneiss along the north-south boundary between the units.
Ali Gneiss	Fine to medium grained (.3-1mm) bt-ms-qtz-pl-sil-ilm-kfs with medium to coarse grained (.7-3mm) qtz.	Fabric defined by bt and ms, with an aggregate mineral lineation defined by bt. Gneissic foliation throughout rock with partial melting observed in small areas. Breakdown of muscovite is interpreted from thin-section samples.	Occupies a large portion of the south and eastern mapping area. Observed to thrust over the Hassan Schist along the east-west boundary between the units.

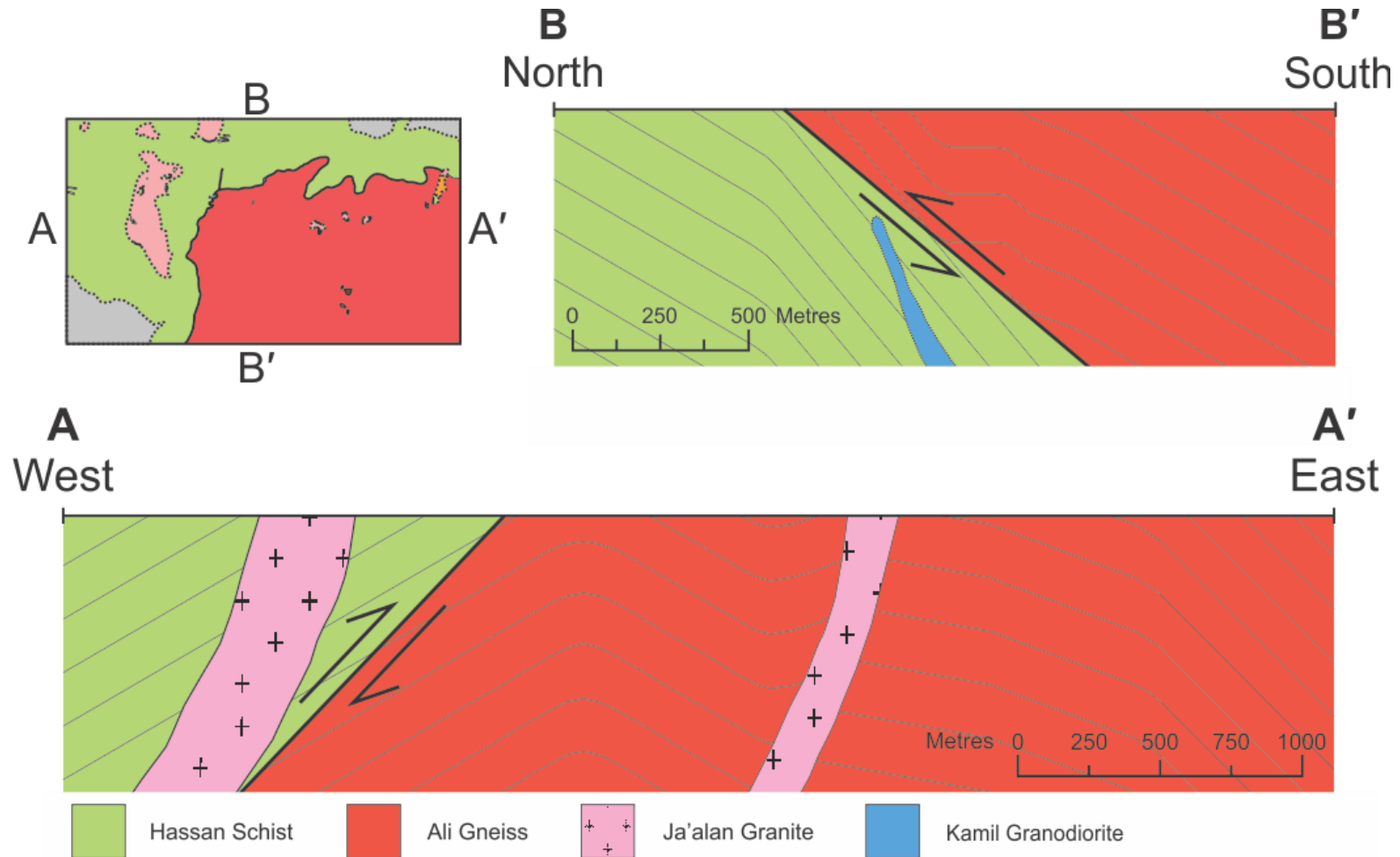


Figure 4. North-south (top right) and west-east (bottom) cross sectional diagrams of Jebel Ja'alan study area, with geological map (top left). Subsurface foliation direction, interpreted from field measurements is indicated by dashed grey lines. North-south cross section shows Ali Gneiss being thrust over Hassan Schist, with interpreted subsurface intrusion of Kamil Granodiorite. West-east cross section shows Hassan Schist being thrust over Ali Gneiss, with intrusions of Ja'alan Granite.

STEREONETS

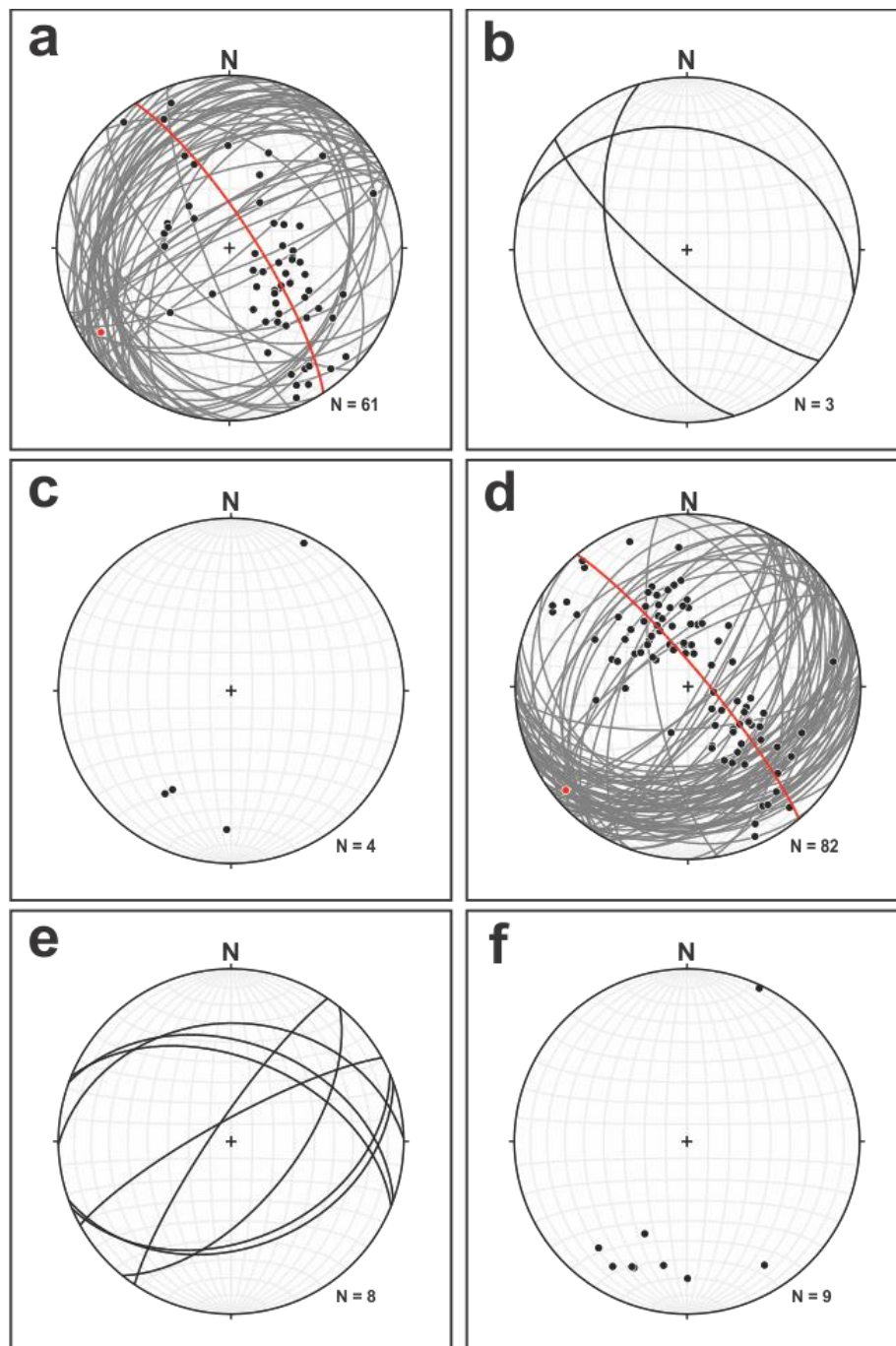


Figure 5. Stereographic projections (Lower hemisphere, equal area) of structural features for domains in the Jebel Ja'alan study area. a) Dip and dip-direction of Hassan Schist foliations plotted as great circles (grey) and poles (black). Profile plane and pole is shown in red; b) Dip and dip-direction of Hassan Schist axial planes (minor folds) plotted as great circles; c) Plunge and plunge direction of Hassan Schist aggregate mineral lineations plotted as points; d) Dip and dip-direction of Ali Gneiss foliations plotted as great circles (grey) and poles (black). Profile plane and pole is shown in red; e) Dip and dip-direction of Ali Gneiss axial planes (minor folds) plotted as great circles; f) Dip and plunge direction of Ali Gneiss aggregate mineral lineations plotted as points.

Structural data of foliations, axial planes and aggregate mineral lineation are presented in stereonet (Fig. 5). Foliation data from the Hassan Schist (Fig. 5a) and Ali Gneiss (Fig. 5d) show opposing groups of northwest and southeast dipping foliations, though with the presence of several close to vertical measurements observed within the Hassan Schist. Calculating the pole to a profile plane of foliation measurements results in a value of 12→237 for the Hassan Schist, and 08→230 for the Ali Gneiss. Measurements of minor fold axial planes within the Ali Gneiss (Fig. 5e) can be seen to be somewhat similar to the spread of foliation data. In comparison, the few measurements in the Hassan Schist (Fig. 5f) are more suggestive of approximately north-south trending folds. Measurements of aggregate mineral lineations in the Hassan Schist (Fig. 5c) and Ali Gneiss (Fig. 5f) display a similar trend of gently inclined south-southwest plunging lineations. It can be observed that the trend of these lineations are approximately 30° away from the calculated poles to profile planes of the Hassan Schist and Ali Gneiss foliation measurements.

Geochronology

LA-ICP-MS IN-SITU MONAZITE U–PB GEOCHRONOLOGY

In-situ U–Pb geochronology was undertaken on samples JA15-04, JA15-06, JA15-40, and JA15-43 from the Hassan Schist, with individual analyses provided in Appendix B. Monazite is abundant within the matrix of these samples (Fig. 6), though often at sizes unsuitable for geochronological analysis (<10µm). However, a total of 27 analyses were obtained from 26 grains located within the matrix. Data are displayed on Wetherill concordia plots (Fig. 7) and probability density plots of either $^{206}\text{Pb}/^{238}\text{U}$ or $^{206}\text{Pb}/^{207}\text{Pb}$ age (Fig. 8).

U–Pb analyses of sample JA15-04 (Fig. 7a) reveal a large spectrum of $^{206}\text{Pb}/^{238}\text{U}$ ages (c. 915–800 Ma). Due to this large range of ages, attempting to characterise the data with a $^{206}\text{Pb}/^{238}\text{U}$ weighted average proves ineffective. However, the $^{206}\text{Pb}/^{207}\text{Pb}$ weighted average yielded an age of 845 ± 19 Ma, with a 2σ confidence and a MSWD of 0.26, suggesting that the spread of data was due to limited open system behaviour of radiogenic Pb. Analyses of samples JA15-06 and JA15-40 (Fig. 7b and 7c, respectively) demonstrate relatively consistent $^{206}\text{Pb}/^{238}\text{U}$ ages in comparison to JA15-04. Sample JA15-06 contains two significantly younger analyses, which have been excluded from average age calculations and may represent radiogenic Pb loss and/or a later phase of limited monazite growth. Weighted $^{206}\text{Pb}/^{238}\text{U}$ averages have yielded ages with a 2σ confidence of 830 ± 7 Ma with a MSWD of 1.12 for sample JA15-06, and 838 ± 11 Ma with a MSWD of 0.13 for sample JA15-40. U–Pb analyses of sample JA15-43 (Fig. 7d) yield only 3 ages, due to the paucity of grains large enough to be dated. As such, an average age has not been calculated for the grains in this sample, rather this sample is solely to demonstrate the presence of similarly aged grains to those in the previous samples at this sampling locality.

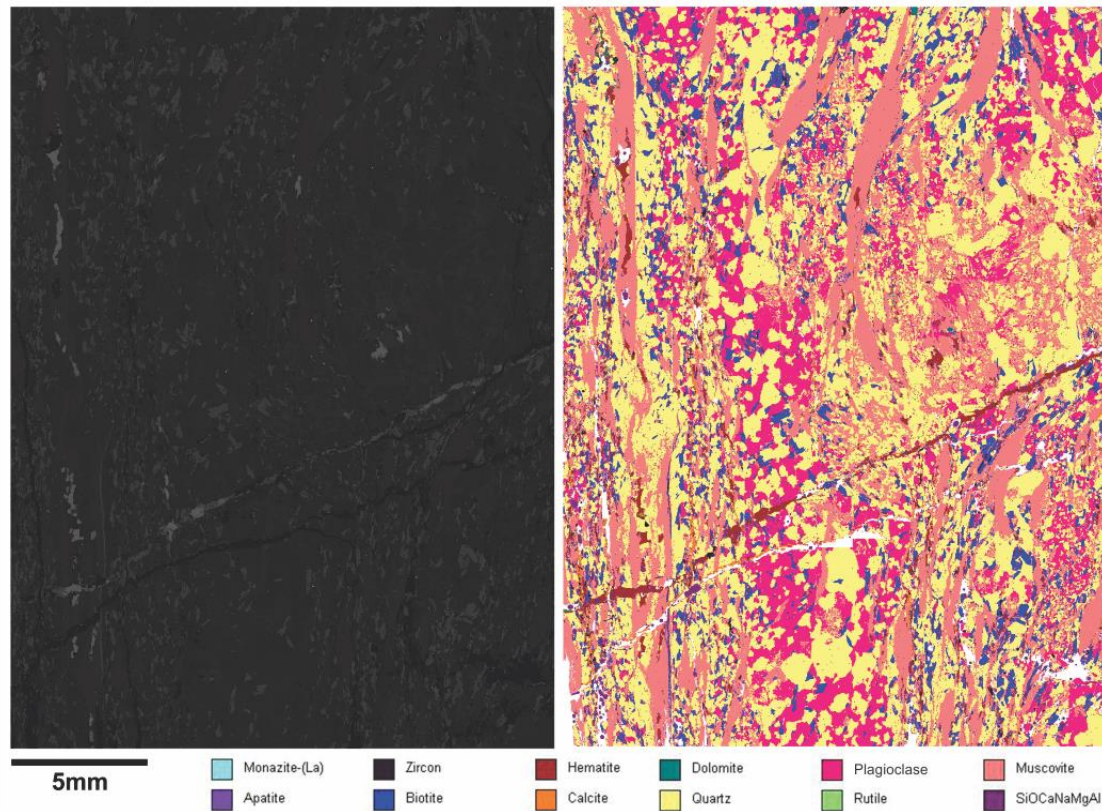


Figure 6. Mineral Liberation Analysis (MLA) thin section map of sample JA15-06, showing a backscattered electron mosaic of the sample (left), and MLA map of the sample (right). The map shows that monazite is present within the matrix of the sample, rather than as inclusions. Also note that minerals in the interpreted peak assemblage of $qtz-pl-ms-sil-bt-ilm-mt \pm st$ can all be observed to have been subjected to deformation.

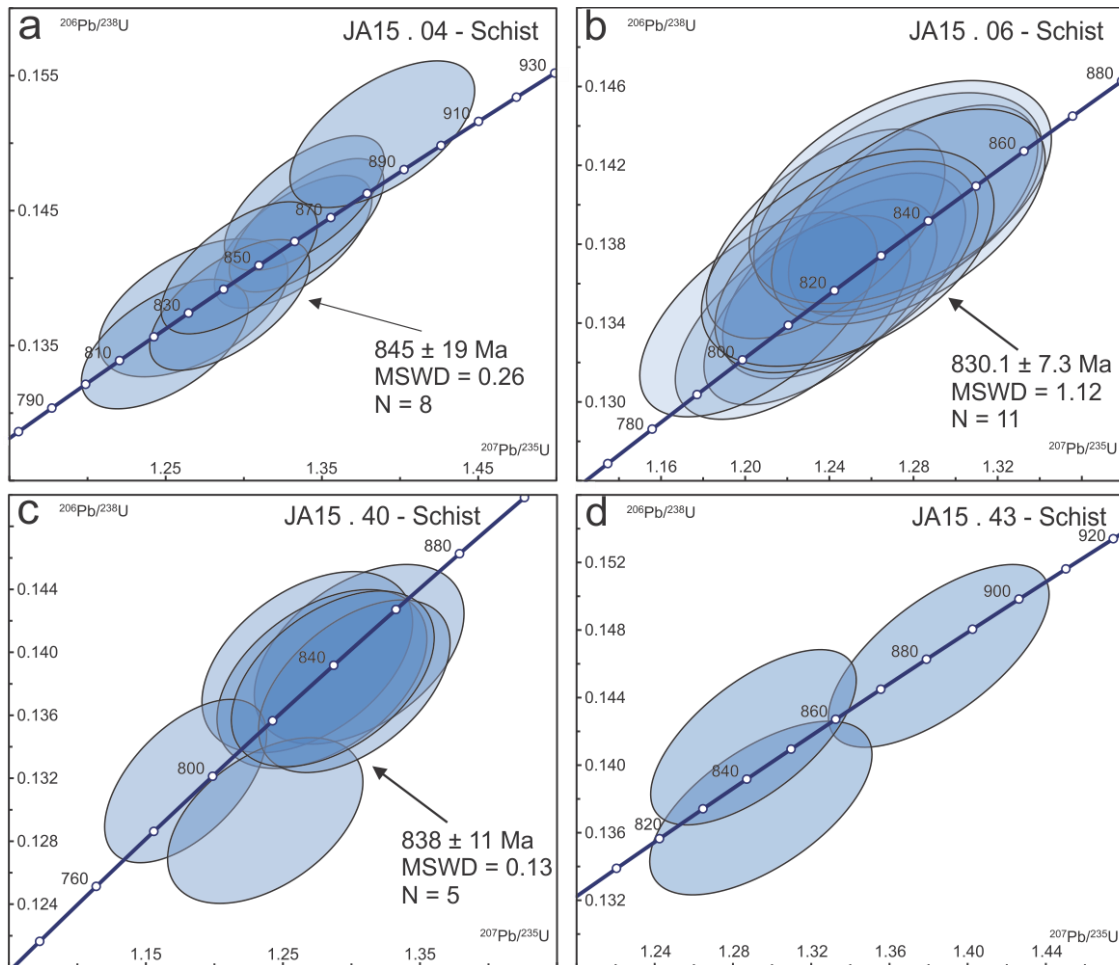


Figure 7. U–Pb Concordia diagrams for monazite grains with a 2σ data point error ellipses. Individual data points are indicated by blue ellipses. Samples correspond to: a) Hassan Schist (JA15-04) with weighted mean $^{206}\text{Pb}/^{207}\text{Pb}$ age of 845 ± 19 Ma; b) Hassan Schist (JA15-06) with weighted mean $^{206}\text{Pb}/^{238}\text{U}$ age of 830.1 ± 7.3 Ma; c) Hassan Schist (JA15-40) with weighted mean $^{206}\text{Pb}/^{238}\text{U}$ age of 838 ± 11 Ma, obtained by excluding two young analyses interpreted to represent either radiogenic Pb loss or a limited phase of monazite growth; d) Hassan schist (JA15-43) with no weighted mean calculated due to low number ($N=3$) of grain analyses.

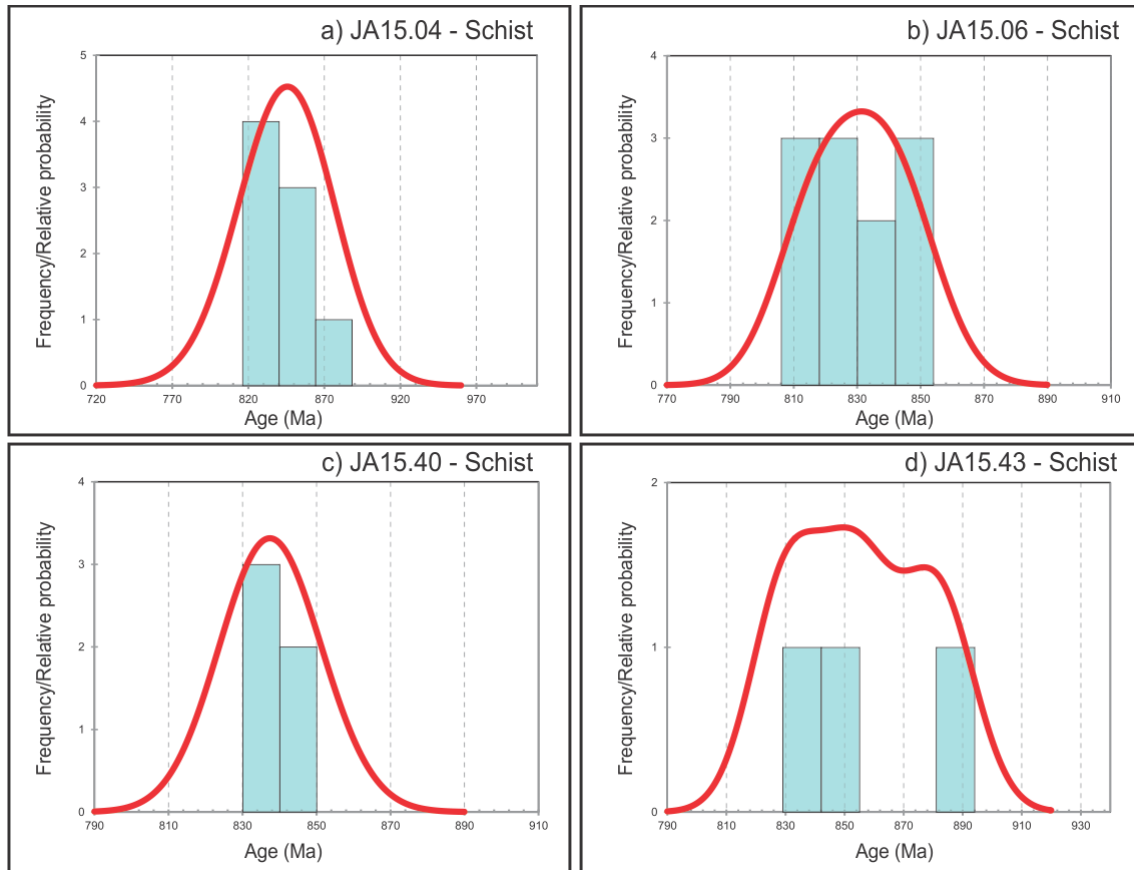


Figure 8. Probability density plot for monazite grains found within Hassan Schist. Ages are plotted as: a) $^{206}\text{Pb}/^{207}\text{Pb}$, weighted average of 845 ± 19 Ma; b) $^{206}\text{Pb}/^{238}\text{U}$, weighted average of 830.1 ± 7.3 ; c) $^{206}\text{Pb}/^{238}\text{U}$ weighted average of 838 ± 11 ; d) $^{206}\text{Pb}/^{238}\text{U}$, with no weighted average calculated due to low number ($N=3$) of grain analyses.

^{40}Ar – ^{39}Ar MUSCOVITE GEOCHRONOLOGY

^{40}Ar – ^{39}Ar data was obtained from muscovite grains within the Ja'alan granite, Hassan Schist, and Ali Gneiss (Appendix B). Ja'alan Granite sample JA15-03 (Fig. 9) displays a weighted average plateau age of 831 ± 15 Ma with a MSWD of 0.30, this age is interpreted to represent the crystallisation age of the granite. Hassan Schist sample JA15-04 (Fig. 10) displays a weighted average plateau age of 830 ± 6 Ma with a MSWD of 0.22, which is within error of the weighted average U–Pb monazite age determined for the same sample.

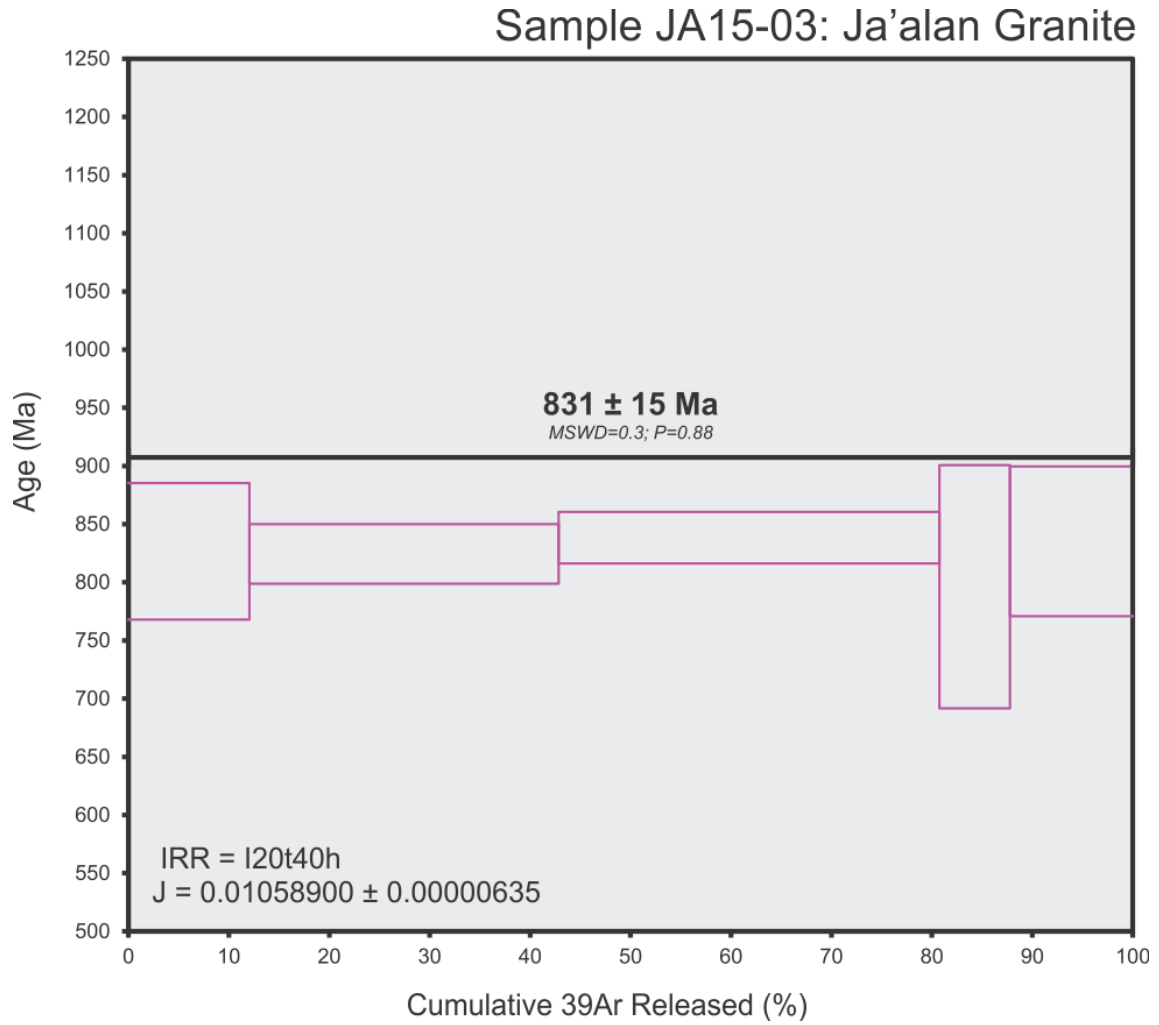


Figure 9. ^{40}Ar - ^{39}Ar muscovite age data plot for Ja'alan Granite sample JA15-03. The sample displays a weighted average plateau age of 831 ± 15 Ma (MSWD 0.30), which is interpreted as the crystallisation age of the granite.

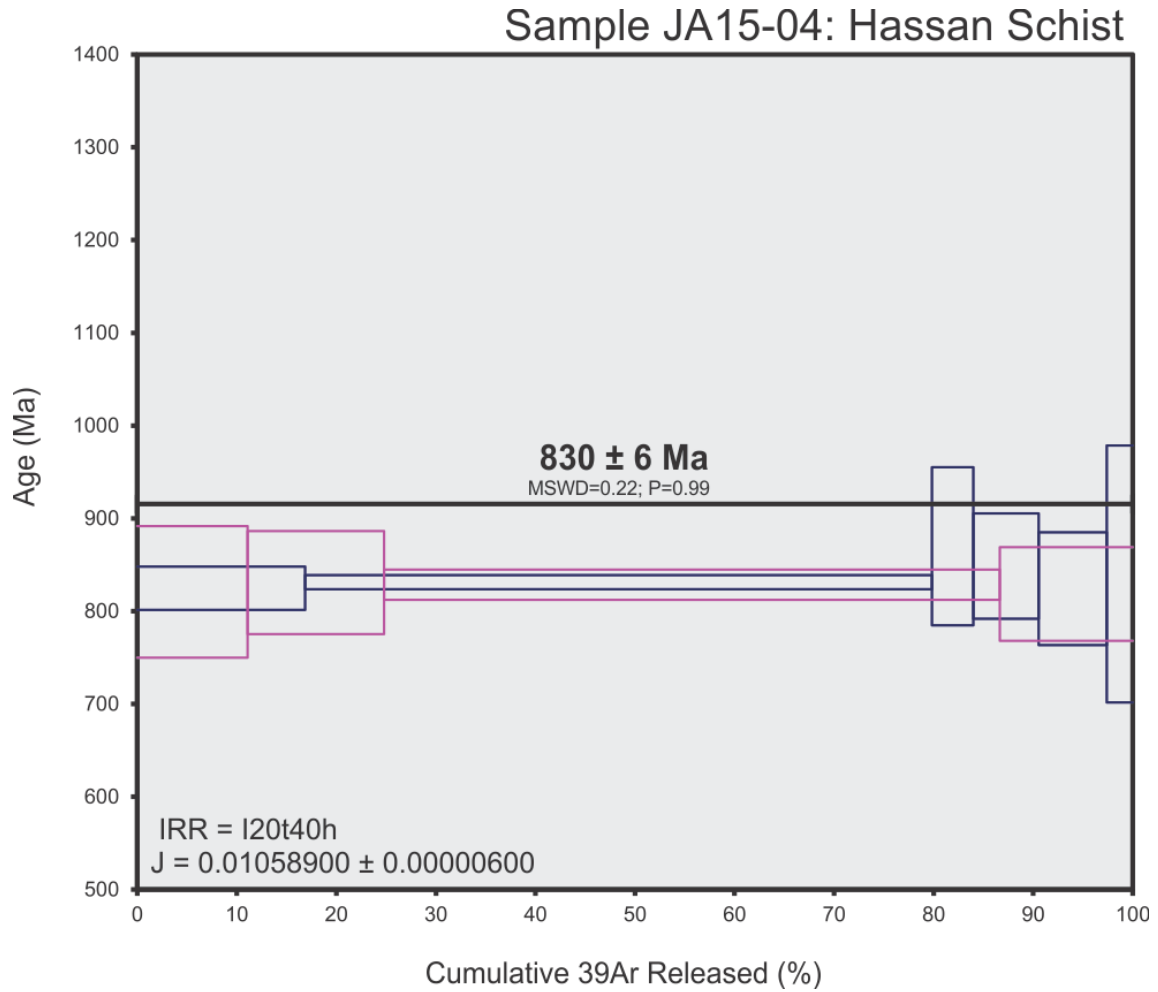


Figure 10. ⁴⁰Ar–³⁹Ar muscovite age data plot for Ja’alan Granite sample JA15-04. The sample displays a weighted plateau age of 830 ± 6 Ma (MSWD 0.22).

Metamorphic geology

PETROLOGY

A detailed petrographic analysis was undertaken on samples taken from the Hassan Schist and Ali Gneiss (Fig. 11). Peak and retrograde mineral assemblages have been interpreted on the basis of grain size and microstructural context.

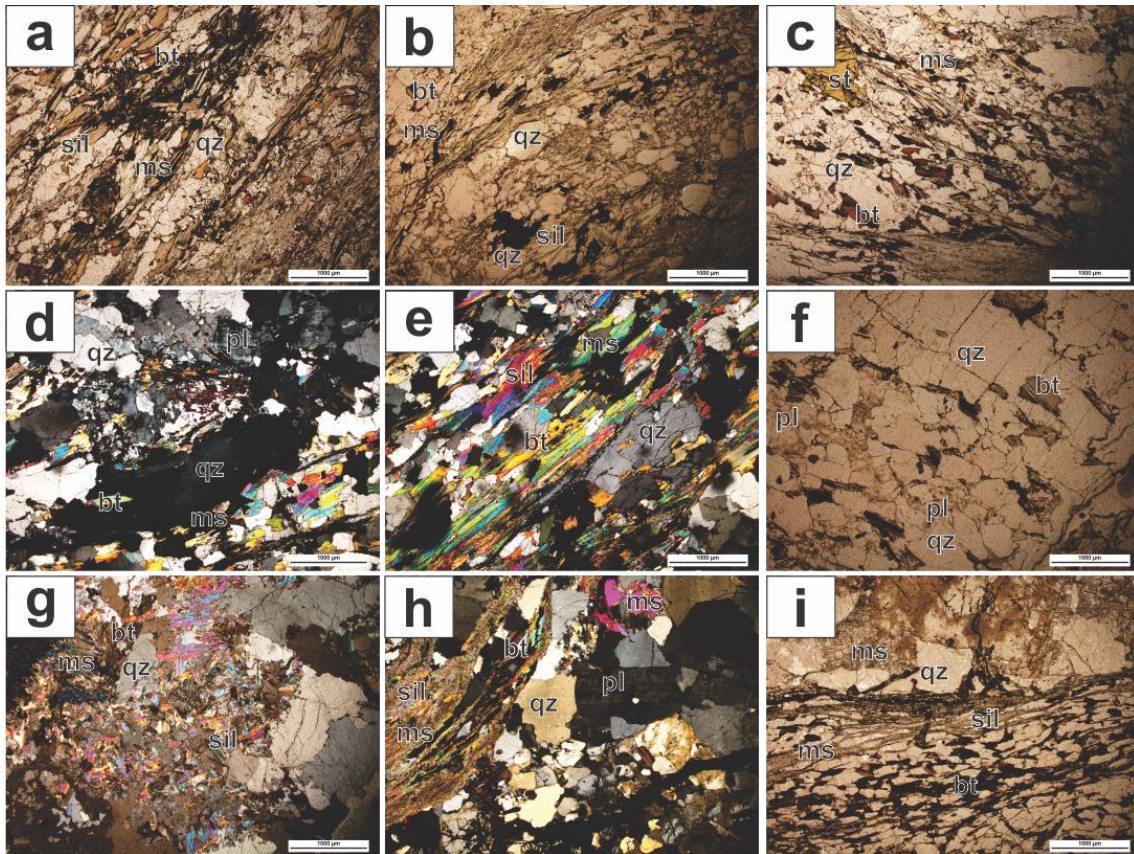


Figure 11. Photomicrographs of petrological relationships within the Hassan Schist and Ali Gneiss units. a) JA15-04 (Hassan Schist) showing fabric defined by biotite and muscovite, biotite and muscovite in contact with quartz, and inclusions of biotite within quartz. b) JA15-06 (Hassan Schist) showing large muscovite grains, interpreted to form part of the peak assemblage, sillimanite rosettes, separation of muscovite and sillimanite by quartz, and the replacement of large muscovite grains with very fine muscovite grains, interpreted to signify the breakdown of muscovite. c) JA15-06 (Hassan Schist) showing staurolite within the muscovite–biotite–quartz–sillimanite matrix, sillimanite rosettes, and fabric defined by biotite and muscovite. d) JA15-36 (Ali Gneiss) showing inclusions of biotite and muscovite within quartz, replacement of large muscovite grains with finer muscovite grains, crosshatch twinning in plagioclase, and separation of biotite and muscovite by quartz. e) JA15-36 (Ali Gneiss) showing fabric defined by muscovite, biotite and sillimanite, inclusions of biotite within quartz, inclusions of quartz within biotite and muscovite, and replacement of large muscovite grains with finer muscovite grains. f) JA15-36 (Ali Gneiss) showing separation of biotite and plagioclase by quartz, and replacement of large muscovite grains with finer muscovite grains. g) JA15-41 (Hassan Schist) showing replacement of large muscovite grains with finer muscovite grains, sillimanite rosettes, and separation of muscovite and sillimanite by quartz. h) JA15-43 (Hassan Schist) showing fabric defined by biotite, muscovite and sillimanite wrapping around quartz and larger muscovite grains, plagioclase featuring simple twinning and quartz inclusions, and randomly oriented biotite separated by quartz. i) JA15-43 (Hassan Schist) showing a strong fabric defined by biotite, muscovite and sillimanite which wraps around quartz grains, replacement of large muscovite grains with finer muscovite grains, separation of muscovite and biotite by quartz, and inclusions of quartz in biotite. Abbreviations from Whitney and Evans (2010).

Hassan Schist

Samples JA15-43, JA15-04, JA15-06 were collected within the mapping area from varying locations within the Hassan Schist (Appendix A). The samples contain quartz, plagioclase, biotite, muscovite and sillimanite with minor ilmenite, magnetite and chlorite. Sample JA15-06 also contains minor staurolite within the matrix, whereas sample JA15-43 contains garnet within the matrix. In all samples fine-grained (0.1–0.4 mm) biotite, muscovite and sillimanite define a pervasive fabric that wraps around quartz and feldspar grains, in addition to larger grains (1 mm) of muscovite. Muscovite that defines the fabric can be observed as aggregates of many fine muscovite grains which often resemble larger grains of muscovite, and are interpreted to have formed from the breakdown of these larger grains. Biotite, muscovite and sillimanite are able to be observed to be in direct contact with quartz. Inclusions of biotite in quartz and inclusions of quartz within biotite are additionally observed within this sample. Sillimanite is in contact with both quartz and fine-grained, fabric-defining muscovite. Chlorite is in visible contact with both larger grained (0.5–1.0 mm) biotite and muscovite. In sample JA15-43 fine-grained (0.2–0.3 mm) garnet is present with euhedral grain shape, albeit partially elongate, and contains inclusions of quartz. The matrix is comprised of fine (0.1–0.3 mm) anhedral quartz and subhedral plagioclase, with quartz forming the majority of the matrix. Sample JA15-43 has a coarse-grained (1–2 mm) matrix of quartz and plagioclase in addition to the finer-grained matrix observed for the other samples. The part of the interpreted peak mineral assemblage common to all three samples is quartz–plagioclase–muscovite–sillimanite–biotite–ilmenite–magnetite. In sample JA15-43 garnet is additionally included in the peak assemblage. Similarly, staurolite is additionally included in the peak assemblage of

sample JA15-06. Post-peak metamorphism in each sample is restricted, separation of biotite and muscovite by fine grained (0.1–0.3 mm) chlorite is observed within each sample, and is interpreted as retrograde alteration, implying chlorite is part of the stable retrograde assemblage.

Ali Gneiss

Sample JA15-36 was taken from the eastern mapped section of the Ali Gneiss (Appendix A). The sample contains quartz, muscovite, biotite, plagioclase, sillimanite, ilmenite and K-feldspar. It can be observed that fine- to medium- (0.3–1.0 mm) grained biotite and muscovite define a pervasive fabric that wraps around quartz and feldspar grains. Muscovite can additionally be seen to overprint this fabric. Zones of very fine-grained (<0.1 mm) muscovite are present within the sample, observed to be in contact with coarser-grained muscovite and quartz, and are interpreted to have resulted from the breakdown of muscovite grains within the rock. Biotite, muscovite and sillimanite are in contact with quartz, plagioclase, and K-feldspar, with inclusions of biotite in quartz and inclusions of quartz in biotite and muscovite. The matrix is predominantly comprised of medium- to coarse- (0.7–3.0 mm) grained anhedral quartz and fine- to medium- (0.2–0.7mm) grained anhedral plagioclase and K-feldspar. The inferred peak mineral assemblage for JA15-36 is quartz–muscovite–biotite–plagioclase–sillimanite–ilmenite–K-feldspar.

MINERAL CHEMISTRY

Full microprobe analyses for silicate minerals in samples JA15-04, JA15-36, JA15-41, and JA15-43 are given in Appendix C. Average mineral chemistry values for muscovite, biotite and garnet grains used to calculate compositional variable contours in

P-T pseudosections are provided in Table 3. Compositional transects were obtained for two garnet grains in Hassan Schist samples JA15-41 and JA15-43. Both transects show similar patterns of decreasing Mg from core to rim, and increasing Mn from core to rim (Figs. 12, 13; Tables 4, 5).

Table 3. Average mineral chemistry values measured for biotite, muscovite, and garnet in samples used in phase diagram calculations accompanied by relevant average compositional variable values.

Mineral	Muscovite	Biotite	Garnet	Muscovite	Biotite	Muscovite	Biotite
Sample	JA15-36	JA15-36	JA15-43	JA15-43	JA15-43	JA15-04	JA15-04
SiO ₂	51.99	36.89	36.39	48.75	29.59	46.69	33.74
TiO ₂	0.15	1.57	0.01	0.35	1.68	0.25	2.55
Al ₂ O ₃	29.77	19.39	20.70	35.66	21.26	37.40	19.02
Cr ₂ O ₃	0.01	0.01	0.02	0.03	0.03	0.02	0.03
FeO	1.85	12.98	30.25	1.20	23.45	0.78	21.72
MnO	0.01	0.41	8.48	0.01	0.25	0.00	0.18
MgO	1.34	13.34	2.35	0.64	9.02	0.39	7.05
ZnO	0.01	0.19	0.01	0.00	0.02	0.01	0.03
CaO	0.02	0.02	0.79	0.07	0.05	0.47	0.02
Na ₂ O	0.72	0.23	0.02	0.43	0.07	1.67	0.35
K ₂ O	10.34	9.22	0.00	7.82	3.43	7.16	9.06
Cl	0.01	0.03	0.00	0.01	0.03	0.02	0.04
F	0.04	0.44	0.05	0.01	0.14	0.00	0.27
Total	96.23	94.53	99.05	94.97	88.96	94.86	93.95
Compositional Variables							
y(bi)		0.42			0.44		0.40
x(mu)	0.53			0.54		0.53	
y(mu)	0.76			0.87		0.92	
x(gt)			0.88				

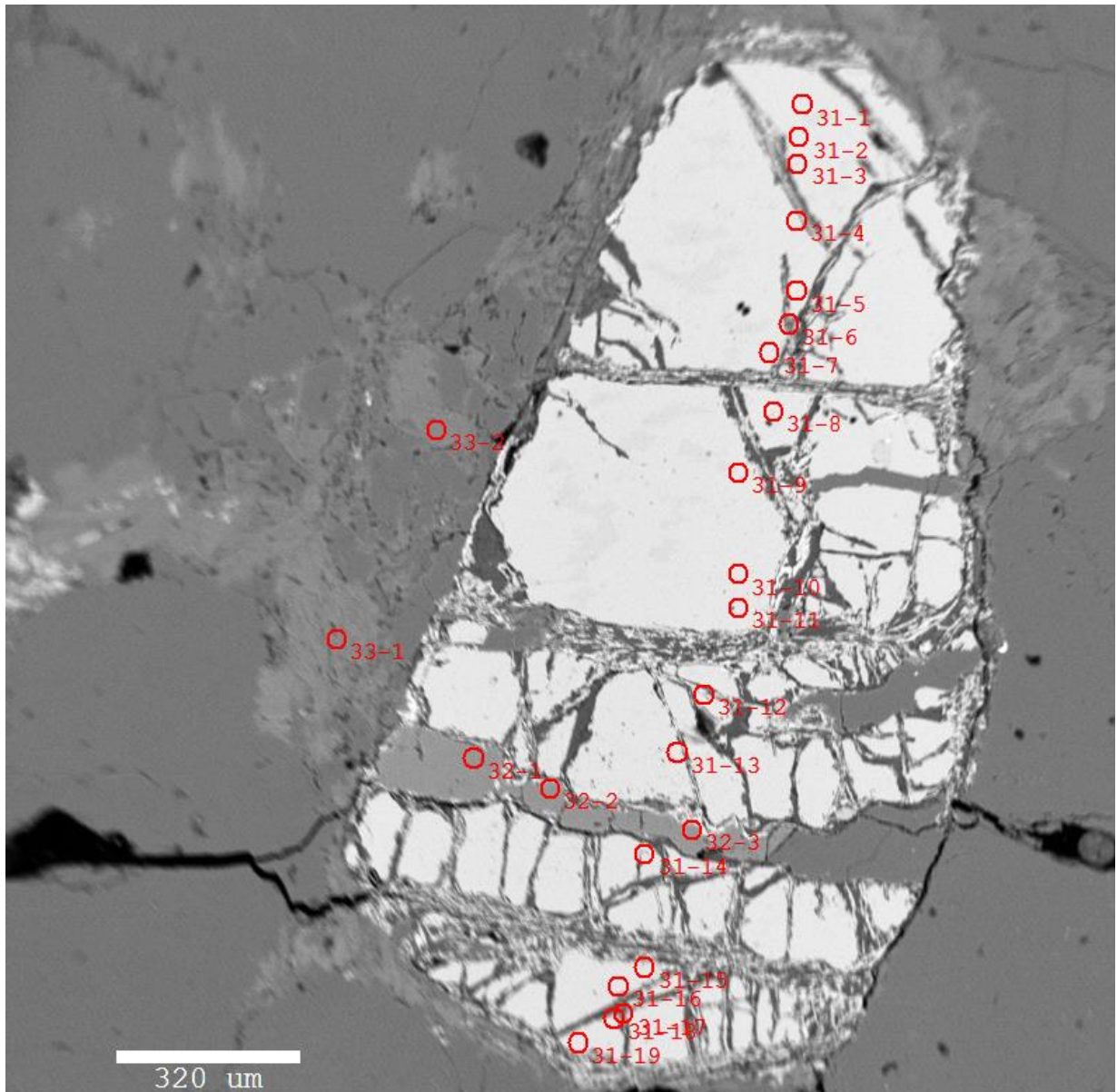


Figure 12. Microprobe image showing the compositional transect undertaken on a garnet grain in Hassan Schist sample JA15-41. Accompanying end-member cation values are provided in Table 4.

Table 4. End-member cation values for spot analyses in the compositional transect of a garnet grain in Hassan Schist sample JA15-41.

Spot Number	Ca	Fe²⁺	Mg	Mn
31-1	0.074	2.143	0.298	0.365
31-2	0.075	2.242	0.306	0.343
31-3	0.077	2.241	0.311	0.332
31-4	0.019	0.587	0.1	0.014
31-5	0.078	2.261	0.314	0.33
31-6	0.075	2.084	0.302	0.254
31-7	0.082	2.273	0.312	0.323
31-8	0.079	2.284	0.304	0.316
31-9	0.072	2.259	0.323	0.312
31-10	0.072	2.293	0.318	0.301
31-11	0.072	1.635	0.239	0.215
31-12	0.075	1.891	0.327	0.248
31-13	0.81	1.98	0.318	0.273
31-14	0.076	2.272	0.32	0.308
31-15	0.071	2.243	0.314	0.341
31-16	0.073	2.222	0.299	0.371
31-17	0.072	2.253	0.285	0.386
31-18	0.071	2.223	0.282	0.401
31-19	0.012	0.51	0.132	0.005

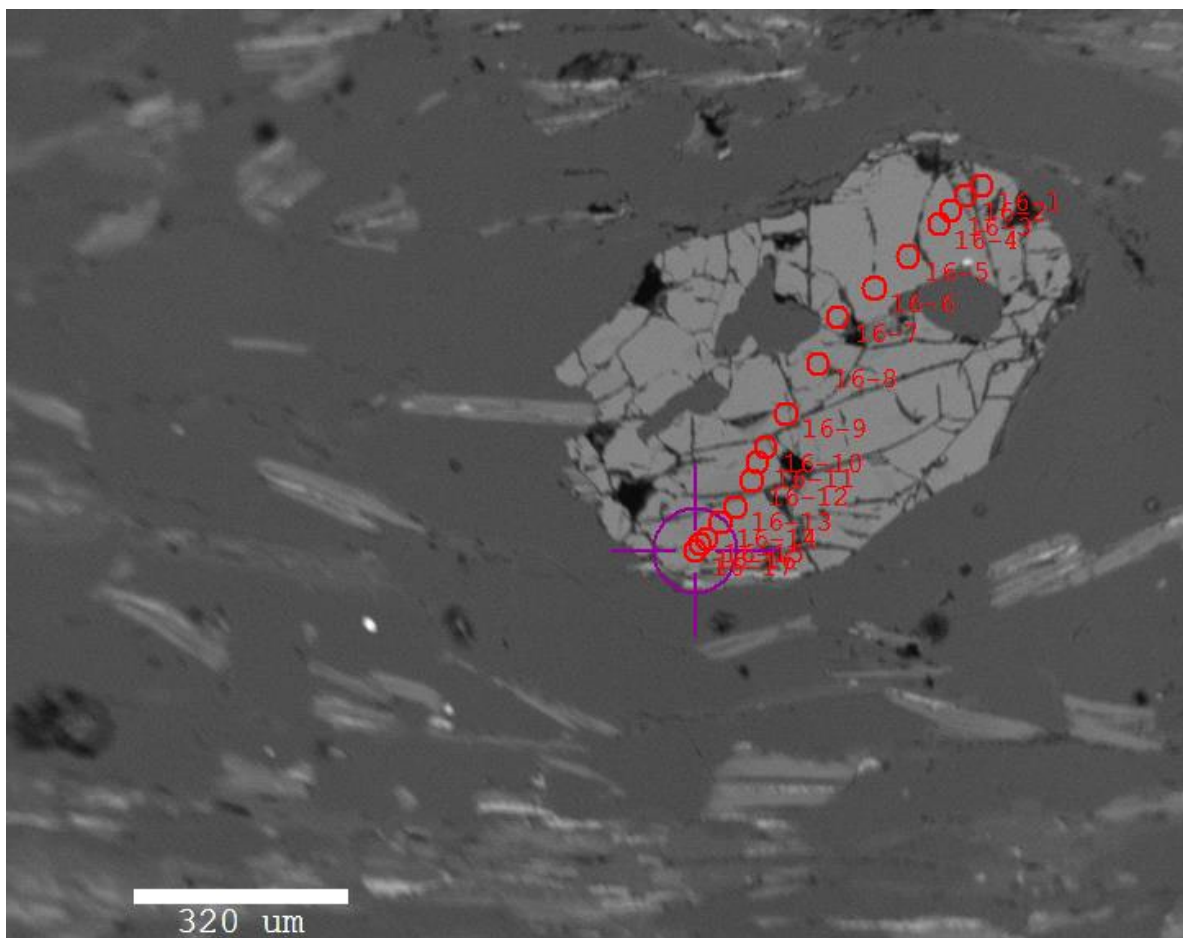


Figure 13. Microprobe image showing the compositional transect undertaken on a garnet grain in Hassan Schist sample JA15-43. Accompanying end member cation values are provided in Table 5.

Table 5. End-member cation values for spot analyses in the compositional transect of a garnet grain in Hassan Schist sample JA15-43.

Spot Number	Ca	Fe ²⁺	Mg	Mn
16-1	0.072	2.015	0.262	0.651
16-2	0.133	1.169	0.200	0.292
16-3	0.07	2.022	0.289	0.602
16-4	0.069	2.056	0.294	0.58
16-5	0.068	2.054	0.293	0.566
16-6	0.07	2.046	0.298	0.564
16-7	0.068	2.031	0.301	0.572
16-8	0.069	2.056	0.296	0.566
16-9	0.066	2.027	0.300	0.547
16-10	0.071	2.037	0.287	0.574
16-11	0.067	2.045	0.294	0.571
16-12	0.067	2.06	0.291	0.576
16-13	0.067	2.046	0.29	0.587
16-14	0.07	2.022	0.288	0.594
16-15	0.073	1.281	0.276	0.62
16-16	0.014	2.025	0.191	0.559
16-17	0.074	0.076	0.253	0.648

TEMPERATURE-AMOUNT PSEUDOSECTIONS

$T-M_0$ (Figs. 14, 15) and $T-M_{H_2O}$ (Figs. 16, 17, 18) pseudosections were calculated to determine appropriate H₂O and Fe₂O₃ ('O') contents for $P-T$ modelling of samples.

Temperature–Amount (Fe_2O_3) Pseudosections

Sample JA15-36
@ 5kbar

MnNCKFMASHTO

	H_2O	SiO_2	Al_2O_3	CaO	MgO	FeO	K_2O	Na_2O	TiO_2	MnO	O
$M_o(0)$	7.89	77.21	6.35	0.18	2.69	2.22	2.52	0.71	0.19	0.06	0.00
$M_o(1)$	7.95	77.79	6.40	0.18	2.71	2.23	2.53	0.71	0.19	0.06	0.75

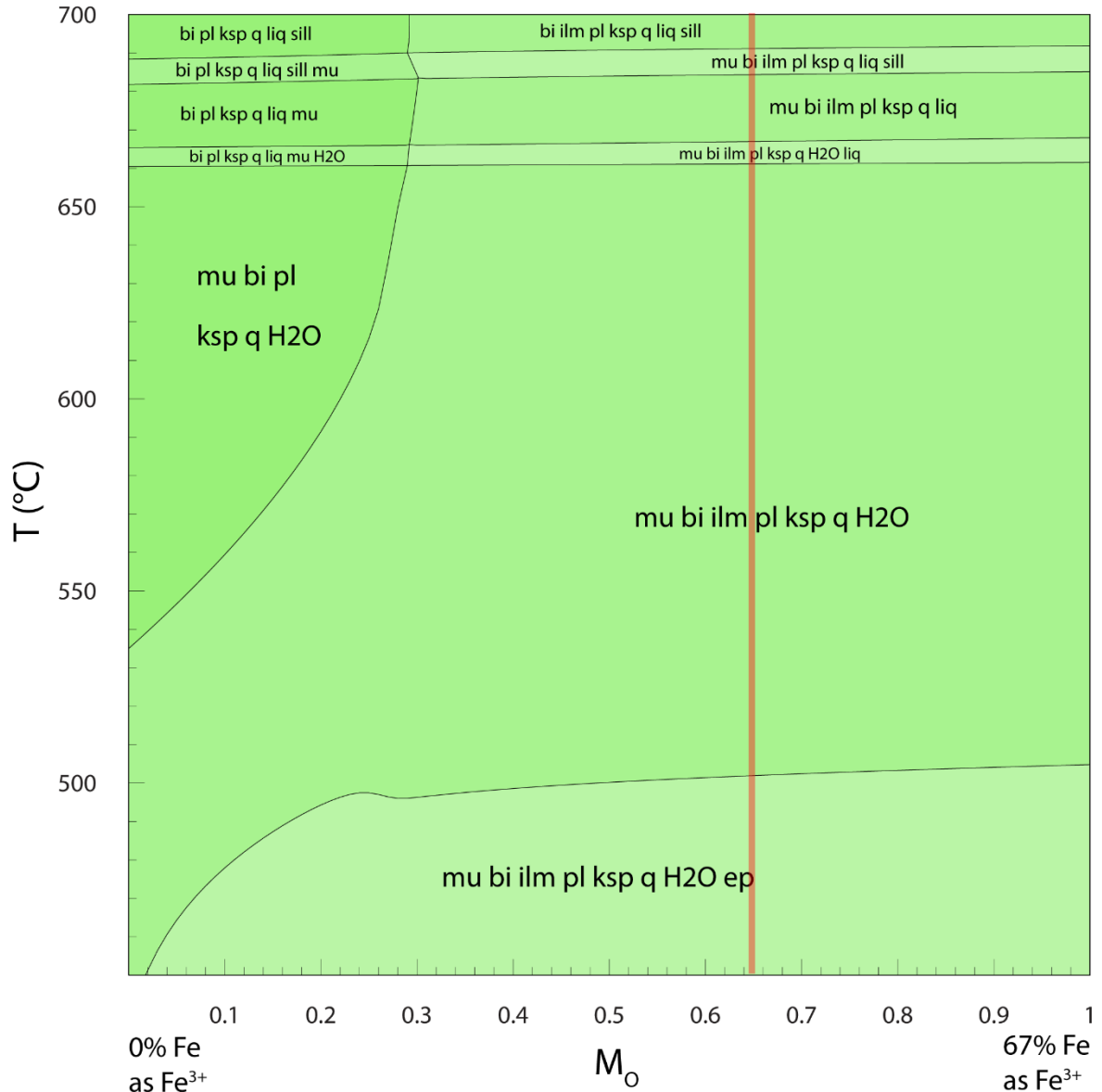


Figure 14. T – M_o pseudosection for sample JA15-36. Compositions given are in mol%. The red line represents the Fe_2O_3 value used for P – T modelling of sample JA15-36.

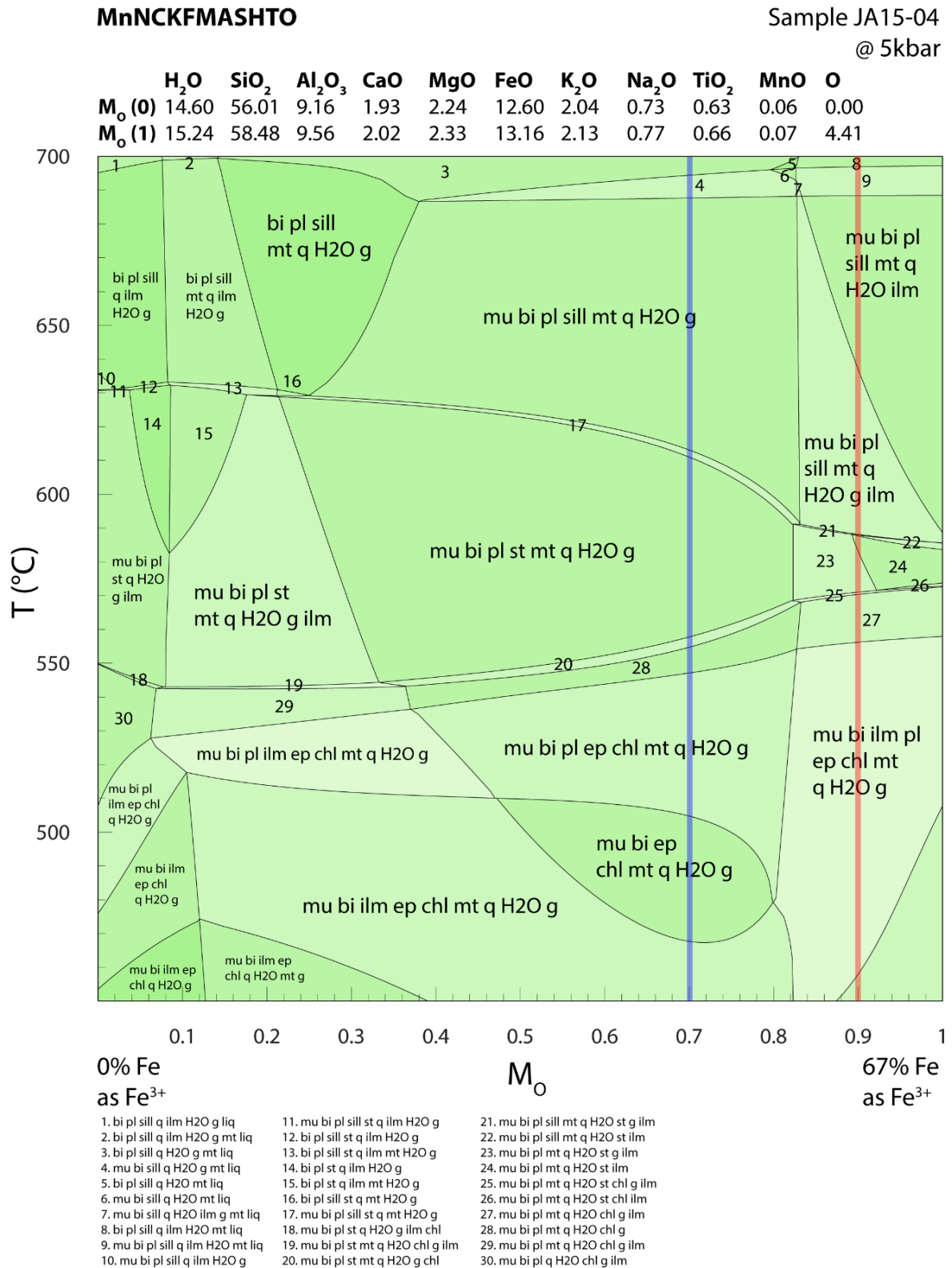


Figure 15. *T*-*M*₀ pseudosection for sample JA15-04 (and by proxy JA15-43). Compositions given are in mol%. The red line for JA15-04 represents the Fe₂O₃ value used for *P*-*T* modelling of sample JA15-04, while the blue line represents the Fe₂O₃ value used for *P*-*T* modelling of sample JA15-43.

The T - M_O pseudosection calculated for Ali Gneiss sample JA15-36 (Fig. 14) shows the interpreted peak field of muscovite–biotite–ilmenite–plagioclase–K-feldspar–quartz–sillimanite–melt occurring between ~ 680 – 690 °C and $M_O = \sim 0.28$ – 1 . The Fe_2O_3 value used for P - T modelling occurs at $M_O = 0.65$. Figure 15 displays the T - M_O pseudosection calculated for JA15-04, and by proxy JA15-43. It shows a complex diagram highlighting the sensitivity of mineral stability to changing oxidation states. The interpreted peak field for JA15-04 of muscovite–biotite–plagioclase–sillimanite–magnetite–quartz–ilmenite– H_2O occurs between ~ 600 – 690 °C and $M_O = \sim 0.84$ – 1 , while the interpreted peak field for JA15-43 of muscovite–biotite–plagioclase–sillimanite–magnetite–quartz–garnet– H_2O occurs between ~ 600 – 690 °C and $M_O = \sim 0.25$ – 0.84 . The Fe_2O_3 value used for P - T modelling occurs at $M_O = 0.9$ for sample JA15-04 and $M_O = 0.7$ for sample JA15-43.

Temperature–Amount (H₂O) Pseudosections

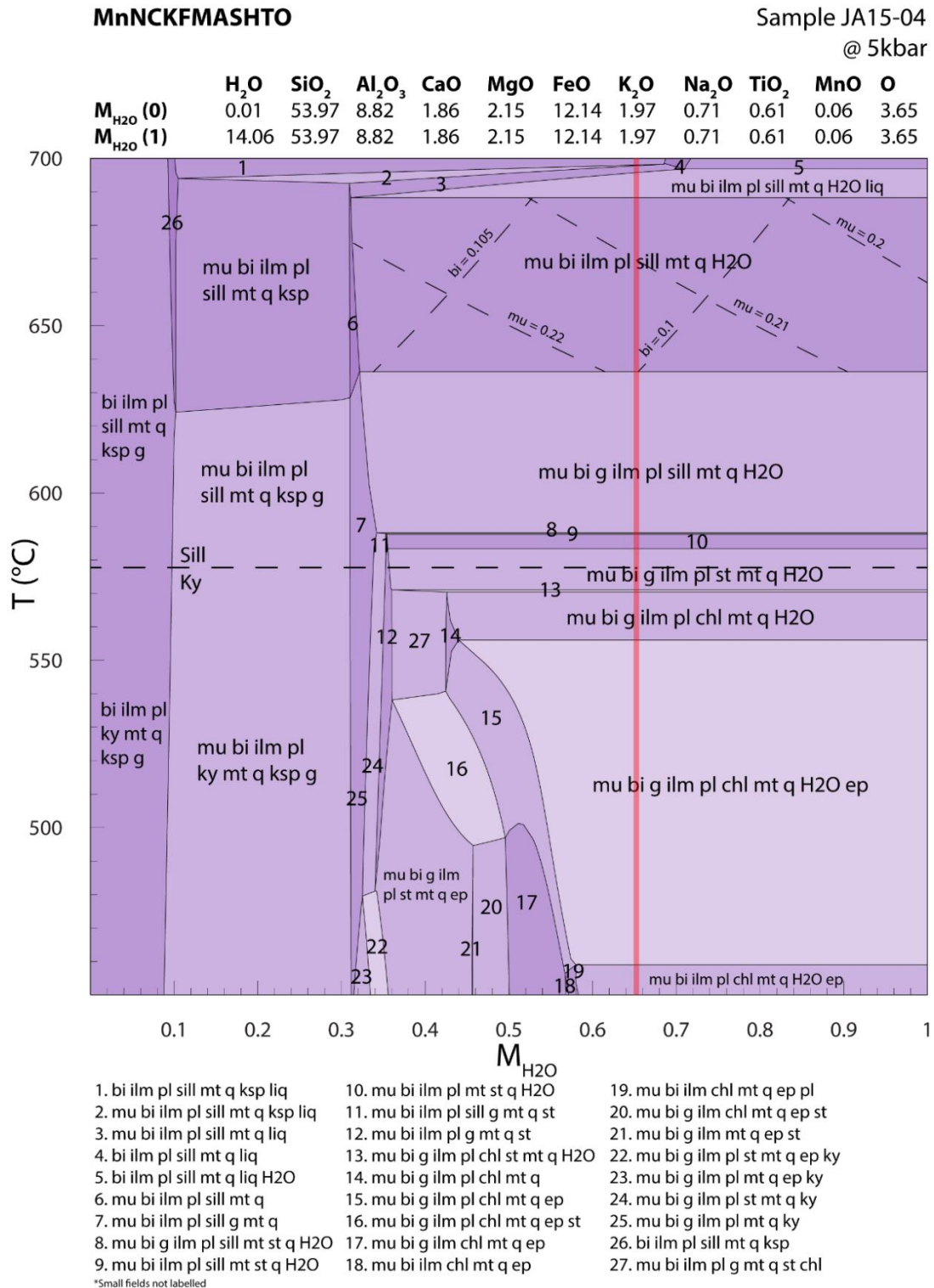


Figure 16. *T*–*M*_{H₂O} pseudosection calculated for samples JA15-04. Compositions given are in mol%. The red line represents the H₂O value used for *P*–*T* modelling of sample JA15-04. Abundance contours for muscovite and biotite are plotted within the interpreted peak field, and show that this assemblage is compositionally relatively insensitive to the amount of H₂O present.

MnNCKFMASHTO

Sample JA15-43
@ 5kbar

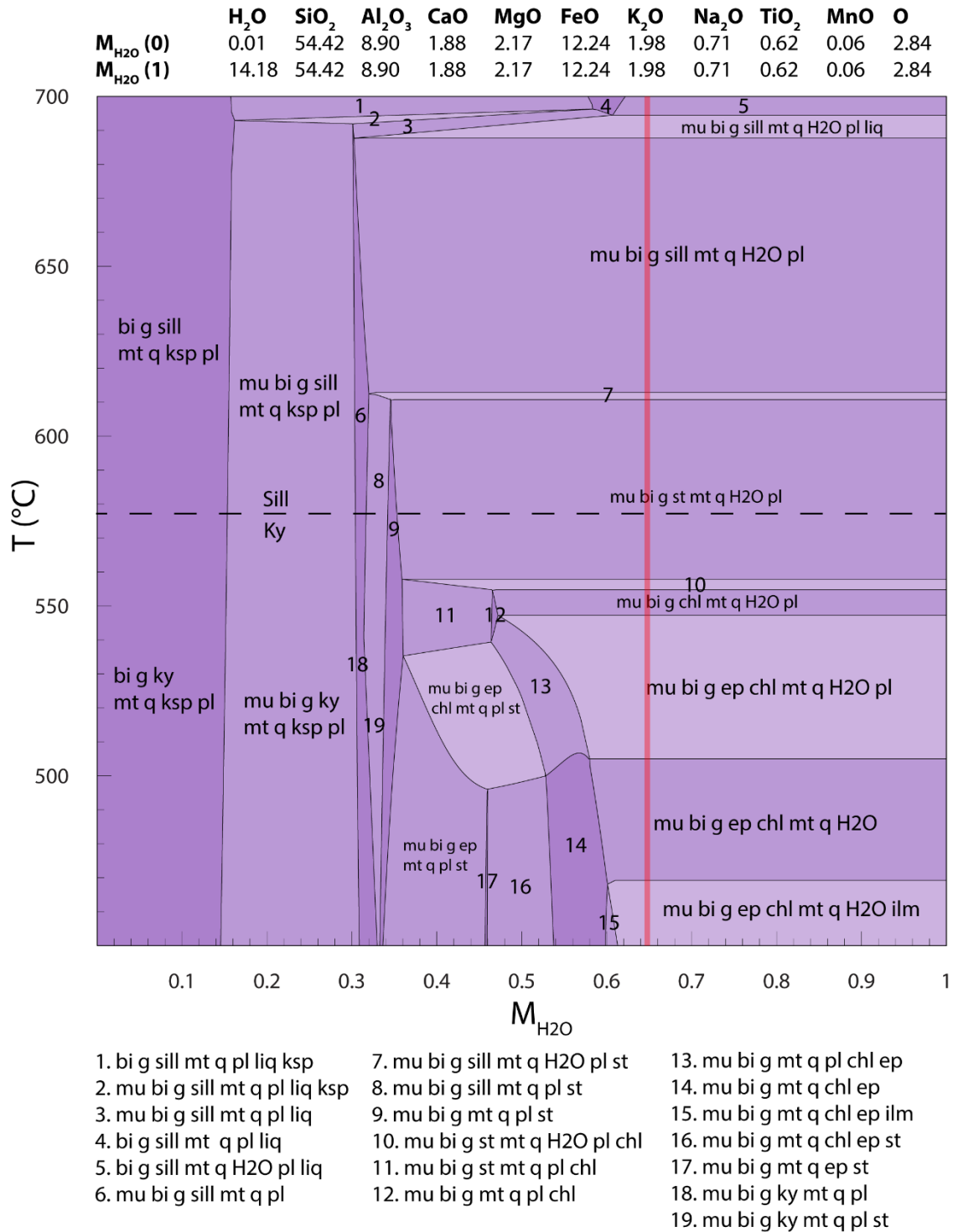


Figure 17. T - M_{H_2O} pseudosection calculated for samples JA15-43. Compositions given are in mol%. The red line represents the H_2O value used for P - T modelling of sample JA15-43.

MnNCKFMASHTO

Sample JA15-36
@ 5kbar

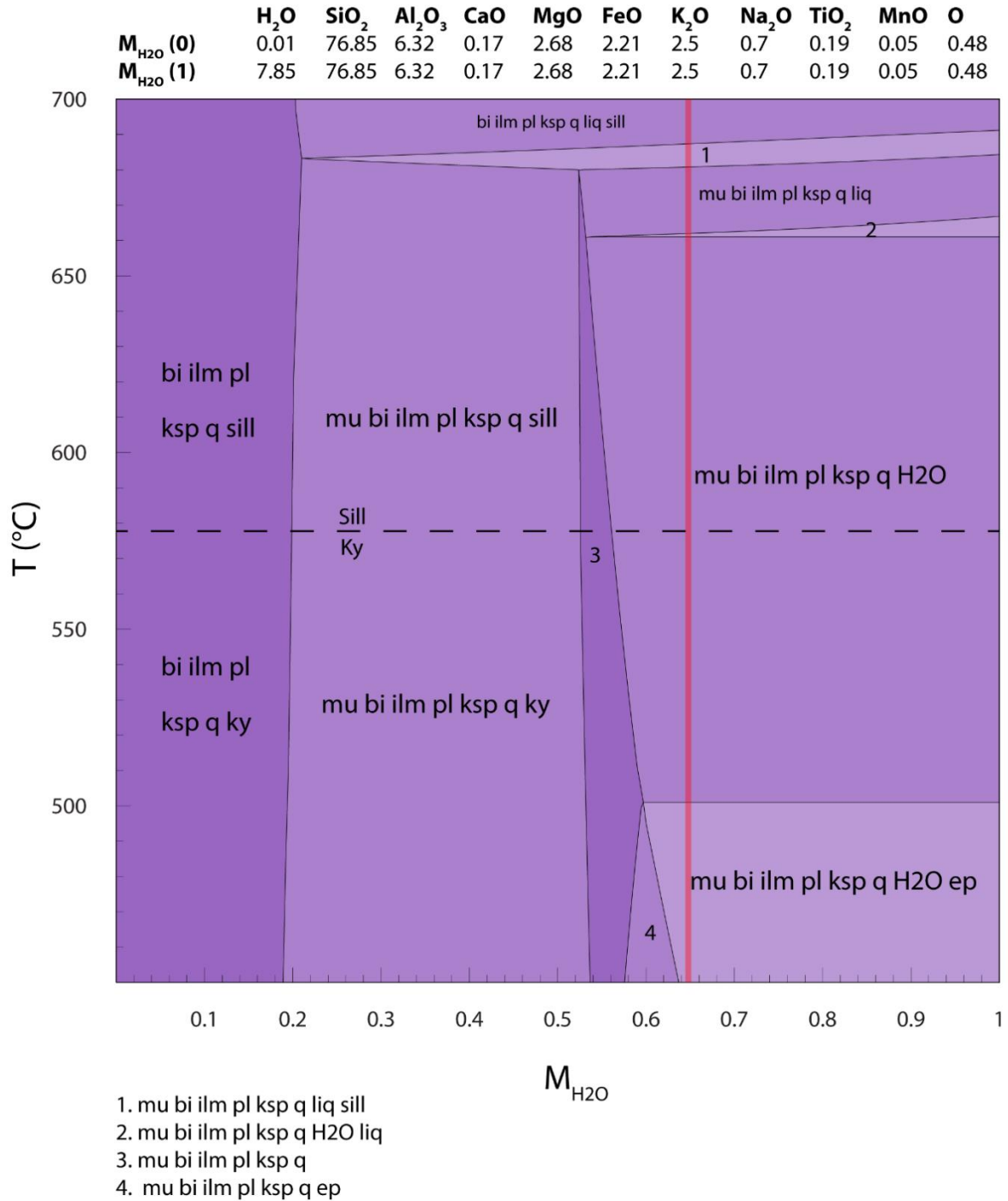


Figure 18. T - M_{H_2O} pseudosection calculated for samples JA15-36. Compositions given are in mol%. The red line represents the H_2O value used for P - T modelling of sample JA15-36.

T - $M_{\text{H}_2\text{O}}$ diagrams calculated for Hassan Schist samples JA15-04 (Fig. 16) and JA15-43 (Fig. 17) show many similarities to each other. The peak fields for both samples occur between $M_{\text{O}} = \sim 0.32$ –1, though at different temperatures, between ~ 615 – 690 °C for JA15-43 and between ~ 640 – 690 °C for JA15-04. Both samples have H_2O values selected for further P - T modelling that occur around $M_{\text{O}} = 0.65$. The T - $M_{\text{H}_2\text{O}}$ diagram calculated for Ali Gneiss sample JA15-36 (Fig. 18), shows the interpreted peak field occurring between ~ 680 – 690 °C and $M_{\text{O}} = \sim 0.2$ –1. Similarly to the Hassan Schist samples, the H_2O value selected for further P - T modelling occurs around $M_{\text{O}} = 0.65$.

PRESSURE-TEMPERATURE PSEUDOSECTIONS

P - T pseudosections were calculated for two samples from the Hassan Schist and one sample of the Ali Gneiss, with the aim of interpreting a P - T path and thermal gradient for rocks in the Jebel Ja'alan area.

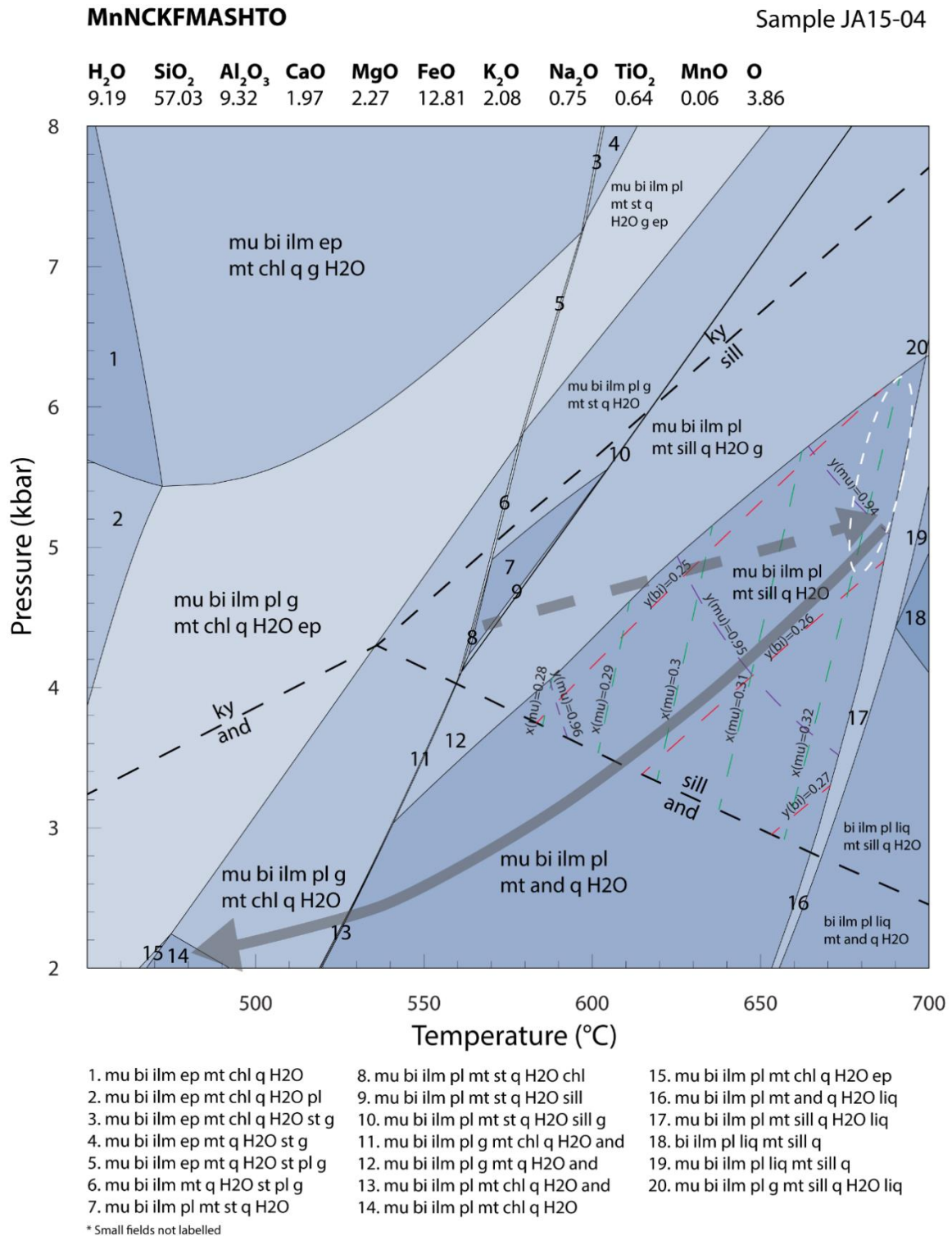


Figure 19. Calculated P – T pseudosection for sample JA15-04 from Hassan Schist. Bulk composition used for modelling is given in the top of the diagram and expressed as mole%. The field muscovite–biotite–ilmenite–plagioclase–magnetite–sillimanite–quartz–H₂O indicates the peak assemblage, with the dashed white oval indicating inferred peak P – T conditions based on the measured chemistry of muscovite. Interpreted prograde and retrograde P – T paths are shown by the grey arrows, with a solid line indicating increased confidence of path trajectory. Coloured dashed lines represent compositional variable contours of muscovite $x(\mu)$ ($= \text{Fe}^{2+}/(\text{Fe}^{2+} + \text{Mg})$ cations), $y(\mu)$ ($= \text{Al}^{\text{VI}}$) and biotite $y(\text{bi})$ ($= \text{Al}^{\text{VI}}$).

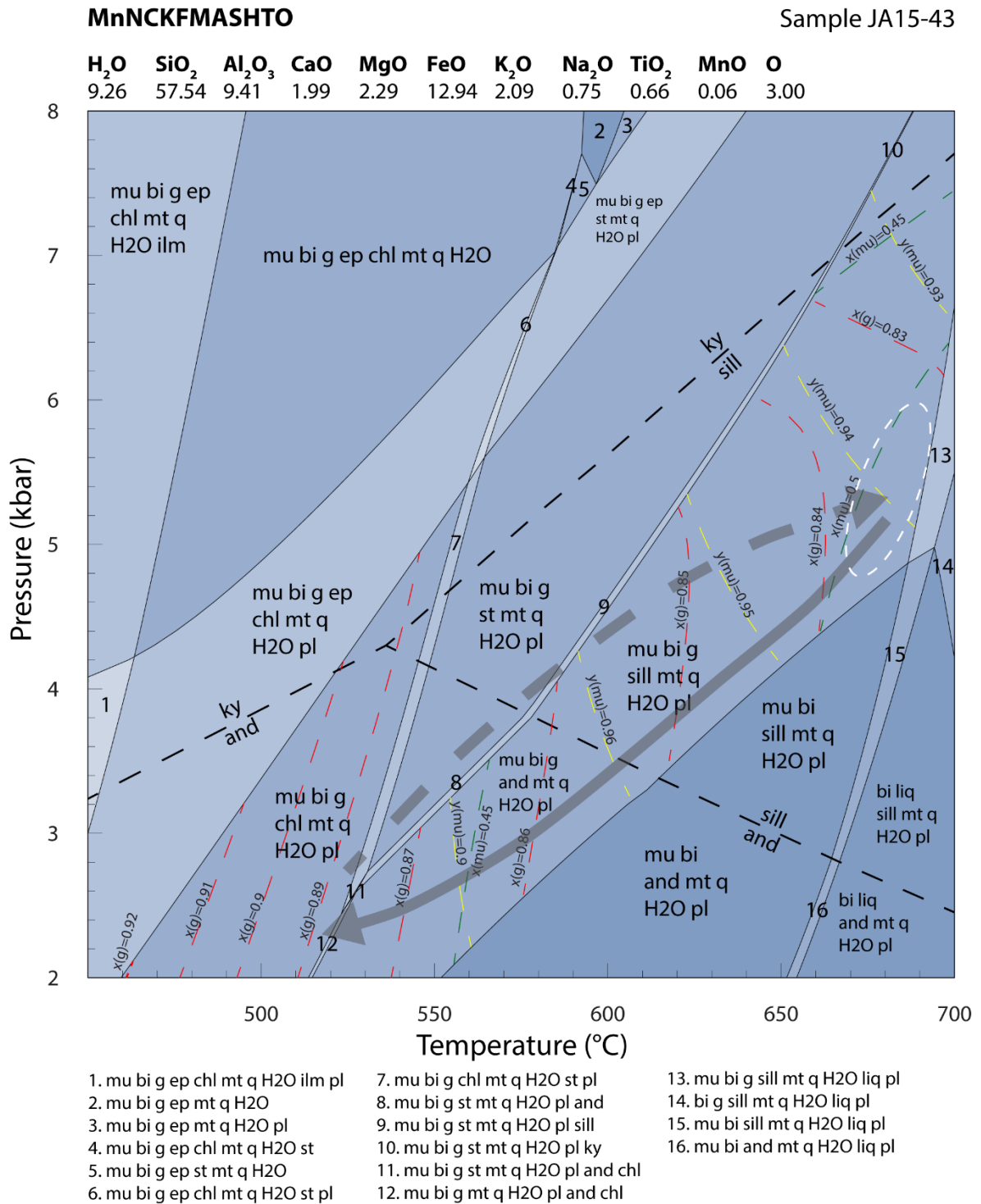


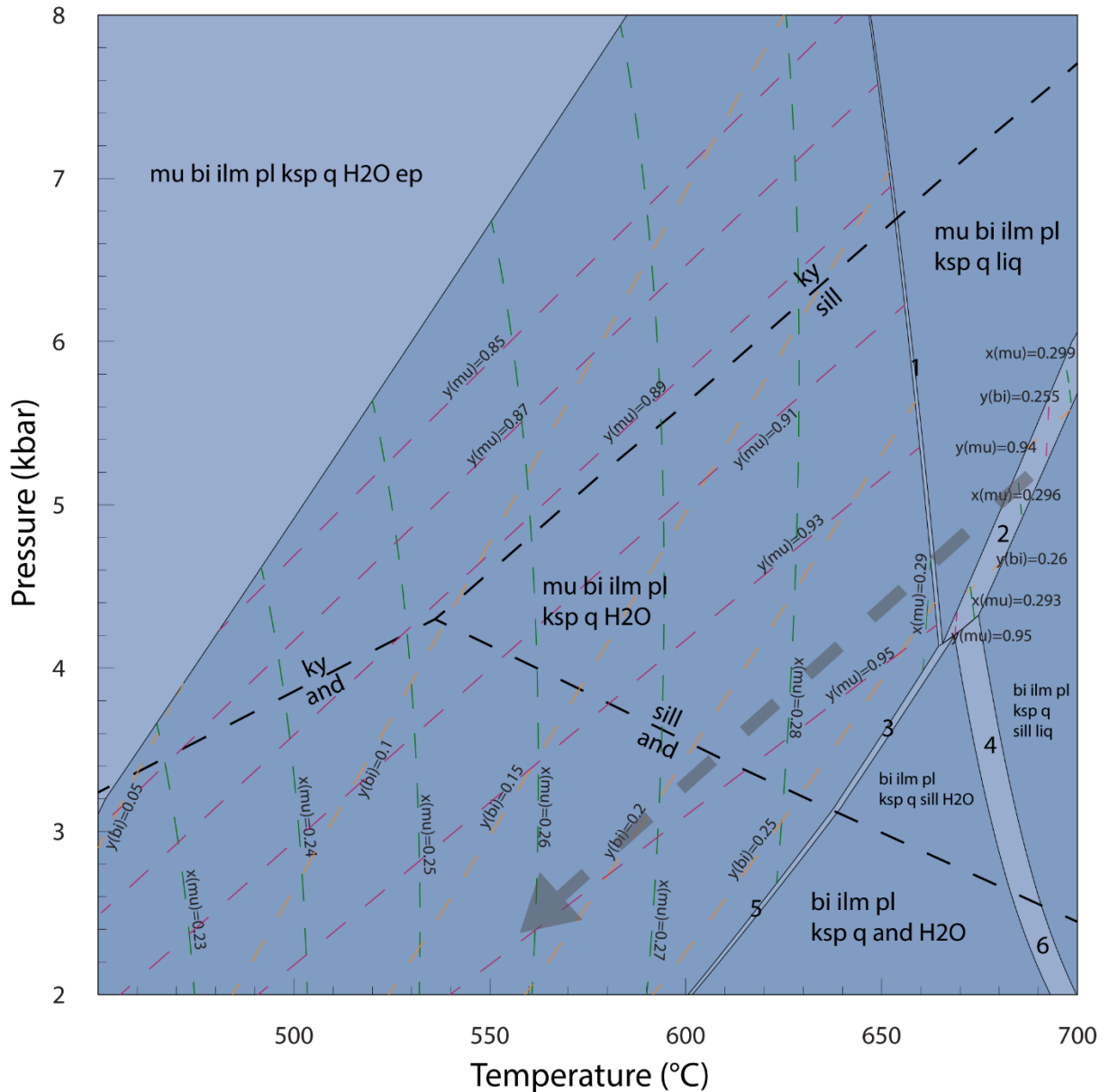
Figure 20. Calculated P - T pseudosection for sample JA15-43 from Hassan Schist. Bulk composition used for modelling is given in the top of the diagram and expressed as mole percent. The field muscovite–biotite–ilmenite–plagioclase–magnetite–sillimanite–garnet–quartz–H₂O corresponds to the peak assemblage, with the dashed white oval indicating inferred peak P - T conditions. Interpreted prograde and retrograde P - T paths are shown by the grey arrows, with a solid line indicating increased confidence of path trajectory. Coloured dashed lines represent compositional variable contours of muscovite $x(\mu)$ ($= \text{Fe}^{2+}/(\text{Fe}^{2+} + \text{Mg})$ cations), $y(\mu)$ ($= \text{Al}^{\text{VI}}$) and garnet $x(\text{g})$ ($= \text{Fe}^{2+}/(\text{Fe}^{2+} + \text{Mg})$ cations).

Pseudosections calculated for Hassan Schist samples JA15-04 (Fig. 19) and JA15-43 (Fig. 20) share a degree of resemblance, which is consistent with the similarities in mineralogy and textural relationships observed in both samples. The staurolite stability field is 'v' shaped and is stable above ~2.5 kbar for sample JA15-43 and above ~4.1 kbar for sample JA15-04, with the range of stable temperatures increasing with pressure. The stability of garnet varies between pseudosections. In sample JA15-04 garnet is unstable below 6.3 kbar and above 520 °C, as well as above 3.9 kbar and below 475 °C. Additionally, garnet is unstable within an area in the centre of the pseudosection, between ~560–605 °C and 4.2–5.6 kbar. In contrast, garnet is stable throughout most of the pseudosection for sample JA15-43, with stability generally increasing with decreasing temperature. The interpreted peak mineral assemblage quartz–plagioclase–muscovite–sillimanite–biotite–ilmenite–magnetite for JA15-04 is stable within the P – T range ~570–695 °C at 2.8–6.3 kbar. Similarly, the interpreted peak mineral assemblage quartz–plagioclase–muscovite–sillimanite–biotite–ilmenite–magnetite–garnet for JA15-43 is stable within the P – T range ~580–700 °C at 3.2–7.6 kbar.

MnNCKFMASHTO

Sample JA15-36

H ₂ O	SiO ₂	Al ₂ O ₃	CaO	MgO	FeO	K ₂ O	Na ₂ O	TiO ₂	MnO	O
5.07	79.17	6.51	0.18	2.76	2.28	2.58	0.72	0.20	0.05	0.49



1. mu bi ilm pl ksp q liq H2O
2. mu bi ilm pl ksp q liq sill
3. mu bi ilm pl ksp q sill H2O
4. bi ilm pl ksp q sill H2O liq
5. mu bi ilm pl ksp q and H2O
6. bi ilm pl ksp q and H2O liq

Figure 21. Calculated P - T pseudosection for sample JA15-36 from Ali Gneiss. Bulk composition used for modelling is given in the top of the diagram and expressed as mole percent. The field muscovite–biotite–sillimanite–ilmenite–plagioclase–K-feldspar–quartz–melt indicates the peak assemblage. The interpreted retrograde P - T path is shown by the grey arrow. Coloured dashed lines represent compositional variable contours of muscovite $x(\mu)$ ($= \text{Fe}^{2+}/(\text{Fe}^{2+} + \text{Mg})$ cations), $y(\mu)$ ($= \text{Al}^{\text{VI}}$) and biotite $y(\text{bi})$ ($= \text{Al}^{\text{VI}}$).

The pseudosection for Ali Gneiss sample JA15-36 (Fig. 21) displays a small number of broad stability fields. Andalusite first becomes stable at ~600 °C and 2 kbar, with stability increasing with temperature. Aluminosilicate stability continues to increase with temperature when stable as sillimanite. Muscovite is stable throughout much of the diagram, becoming unstable at lower pressures (< 5.6 kbar) and higher temperatures (> ~600 °C). The interpreted peak assemblage quartz–muscovite–biotite–plagioclase–sillimanite–ilmenite–K-feldspar–melt is stable within the P – T range ~665–700 °C at 4.2–6 kbar.

DISCUSSION

The aim of this study is to unravel the relationship between the structural and metamorphic evolution of basement rocks within Jebel Ja'alan, in order to expand the current framework of understanding for this region.

Pressure–Temperature–time evolution

Mineralogical and textural features, as well as compositional variations in muscovite, biotite and garnet provide constraints on the metamorphic history of rocks in Jebel Ja'alan. In Hassan Schist sample JA15-04 the measured compositions of muscovite and biotite are inconsistent with those calculated within the interpreted peak field, being greater than the calculated values though are suggestive of peak metamorphic conditions being towards the higher temperature portion of the peak assemblage, around 670–700 °C at 4.5–6 kbar. The field outcrop shows no evidence for having melted near this sample (i.e. leucosomes are absent), so the P – T conditions must not have reached the solidus (Fig. 19). A prograde P – T path is difficult to infer from this sample alone, however the presence of staurolite in sample JA15-06, located approximately 50 m

away from JA15-04 (Appendix A) can be used to broadly constrain a path passing through the staurolite stability field. The absence of garnet in the sample suggests that this prograde path is likely to have only briefly passed through the garnet stability field, thus providing some constraint on the inferred P – T path. The separation of peak muscovite and biotite by chlorite is indicative of a retrograde P – T path passing into the chlorite stability field, with the absence of epidote and garnet observed in the stable retrograde mineral assemblage further constraining the trajectory of the P – T path. In sample JA15-43 (Fig. 20), the measured composition of muscovite is again inconsistent with that calculated for the interpreted peak assemblage field, but likewise suggests peak conditions being located in the higher temperature portion of the peak field, around 665–695 °C at 4.2–6.2 kbar. Measured compositions of garnet in sample JA15-43 show decreasing Mg from the core to rim of grains, and increasing Mn from core to rim (Figure 13; Table 5). These patterns have been previously suggested by Tuccillo *et al.* (1990) to represent a diffusional retrograde effect, where resorption of garnet to form biotite enriches garnet in Fe relative to Mg. Additionally, as Mn does not easily incorporate into biotite this forms an enrichment of Mn on the garnet rim. These variations in mineral chemistry are reflected in the measured $x(g)$ ($= \text{Fe}^{2+}/(\text{Fe}^{2+} + \text{Mg})$ cations) values, and are able to be correlated with the calculated $x(g)$ values for sample JA15-43 to constrain the retrograde P – T conditions and path trajectory. The trajectory of the retrograde path is further constrained by the absence of staurolite in the sample, suggesting that retrograde P – T conditions were not favourable to the growth of this mineral. The measured $x(g)$ values, when compared to the calculated values, suggest that the sample decreased to between 510–540 °C and 2–2.6 kbar after peak metamorphism, which is corroborated by the presence of chlorite in the stable

retrograde assemblage. A prograde path is difficult to infer for this sample, though based on similarities to samples JA15-04 and JA15-06, a prograde path passing briefly through the staurolite stability field is possible.

Modelling of the Ali Gneiss (Fig. 21) indicates similar peak metamorphic conditions to that of the Hassan Schist, with peak assemblages likely forming within the range ~665–700 °C at 4.2–6 kbar. As discussed by Corfu *et al.* (2003), these P – T conditions are favourable to metamorphosing zircon, with a fluid rich system able to produce euhedral shaped grains. This may explain the low spread of ages and igneous appearance of zircon grains reported by Thorpe (2015). The lack of retrograde mineral development, in addition to the measured composition of muscovite and biotite being largely inconsistent with those calculated for this sample, make inferring a P – T path problematic. The observation of sillimanite occurring exclusively in the peak assemblage, and the inferred P – T paths of the Hassan Schist samples, allows for a loosely inferred P – T path at best that is similar to that interpreted for the Hassan Schist, with P – T conditions returning below the solidus.

Discrepancy between the measured and calculated compositions of muscovite and biotite grains within collected samples may be attributed to one or both of the following: 1) ferric iron present in analysed grains that cannot be accounted for by cation calculation procedures. Ferric iron will cause measured $y(\mu)$ and $y(\text{bi})$ values to increase; 2) for natural biotite, cation calculation (and hence calculation of variables such as $y(\text{bi})$) is made difficult due to the complex, coupled way in which Ti substitutes into the lattice (Waters & Charnley 2002).

U–Pb age data from matrix monazite grains from three Hassan Schist samples preserve ages of 845 ± 19 Ma, 838 ± 11 Ma and 830 ± 7 Ma. These ages are within error of each

other and a weighted mean of them yields an age of 833 ± 15 Ma (MSWD = 1.6). This age is interpreted to reflect near peak metamorphic conditions, as monazite has been shown to grow in metapelites from ~ 525 °C (Wing *et al.* 2003, Corrie & Kohn 2008), remaining closed to lead loss at or above sillimanite stability (Smith & Barreiro 1990). ^{40}Ar – ^{39}Ar age data from muscovite grains located within the Hassan Schist suggest a similar timing of peak metamorphism, yielding a plateau age of 830 ± 6 Ma. ^{40}Ar – ^{39}Ar age data from muscovite grains within the Ja'alan Granite display a plateau age of 831 ± 15 Ma, suggesting that emplacement and crystallisation of the granite was approximately coeval with peak metamorphism.

Thermal Gradient and Tectonic Setting

The interpreted peak P – T conditions experienced by the Hassan Schist and Ali Gneiss are in agreement with what was inferred by Gass *et al.* (1990) on the basis of mineralogical observations. Inferred P – T paths, constrained by linking the measured compositions of minerals to calculated phase compositions, as well as via petrographic observations related to mineral stability fields, suggest a clockwise P – T path for rocks in Jebel Ja'alan, with increasing pressure and temperature conditions along a Barrovian thermal gradient, approximately 116.7–148.9 °C/kbar or 38.9–49.6 °C/km. Such a thermal gradient is consistent with what is associated with an active arc setting, as shown in a variety of locations (e.g. Bard 1983, Zhao *et al.* 2001, Brown 2007b, Abu El-Enen 2011, Jarrar *et al.* 2013). However, it should also be noted that these calculated gradients can also be attributed to collisional orogenic settings unrelated to an arc environment, as shown by Brown (1993) in addition to Kelsey and Hand (2015). The calculated thermal gradient in this instance is attributed to metamorphism occurring within an arc environment, which is in agreement with both current and previous work

documenting the geochemistry of basement rock in Oman (e.g. Gass *et al.* 1990, Worthing 2005, Murray 2015).

Structural regime and timing

It can be seen from the data collected that foliation measurements of the Hassan Schist are dominantly northeast dipping, while the opposite holds true for the Ali Gneiss. This is interpreted to represent measurements of these lithologies being taken on opposing limbs of E-W trending folds in the area, suggesting that near horizontal planes have been measured in close proximity to a fold hinge. Measurements of minor fold axial planes from the Ali Gneiss are broadly E-W striking and are consistent with this phase of folding. However N-S striking axial planes from the Hassan Schist are interpreted as being related to a second phase of N-S trending folding. Mineral aggregate lineation data from both lithologies correlate reasonably well with the plunge and plunge direction of the fold hinges calculated from foliation measurements (12→237 for the Hassan Schist, 08→230 for the Ali Gneiss), though can be seen to consistently trend in a more southerly direction (~200°). It is interpreted that this discrepancy between aggregate mineral lineations and calculated fold hinges may be the result of shearing that has occurred prior to the folding of both units. Restoring these measurements to pre-folding values gives an approximate trend of 55→115 for plunge and plunge direction.

The structures observed in the study area are indicative of multiple regional scale deformation events affecting the region. It is likely that the area has been affected by at least two main deformation events, interpreted to occur both during and post metamorphism. The aggregate mineral lineations observed in the Hassan Schist and Ali Gneiss are interpreted to have originally formed as a result of shearing that occurred

prior to these main deformation events. The first deformation event (D_1) involved the top to the NNE thrusting of the Ali Gneiss over the Hassan schist, creation of approximately E-W trending folds (F_1), and generation of the foliation planes (S_1) observed within the study area. Both field (Fig. 2) and petrographic (Fig. 11) observations are suggestive of this deformation occurring at high temperatures, and thus this event is interpreted to be contemporaneous with or slightly postdating peak metamorphism (c. 830 Ma). The second deformation event (D_2) resulted in a series of structures interpreted to have formed within an E-W compressional stress regime. It is during this period of deformation that top to the east thrusting of the Hassan Schist over the Ali Gneiss is interpreted to have occurred. This is in addition to the creation of the two broad, approximately N-S trending folds (F_2) and a heterogeneously developed crenulation cleavage (S_2) observed to the north of the study area. The timing of this second deformational period is difficult to constrain, however Filbrandt *et al.* (1990) describes observing E-W compressional structures within the overlying Simsima formation, which would constrain the age of deformation to being younger than the Maastrichtian if belonging to the same deformation event.

Implications for the Arabian-Nubian Shield and Omani basement

As discussed previously, several authors have interpreted that the basement of Oman formed on the juvenile crust of the Mozambique Ocean, in an arc setting (e.g. Gass *et al.* 1990, Meert 2003, Rantakokko *et al.* 2014). P - T paths and thermal gradients interpreted from phase diagrams calculated in this study are not able to directly support these interpretations, as they are consistent with a variety of collisional settings (Brown 1993, 2007b, Abu El-Enen 2011, Jarrar *et al.* 2013). As such, the interpreted conditions of metamorphism cannot be shown to discredit any previous interpretations of the Jebel

Ja'alan basement forming within an arc environment. Although metamorphic conditions have not yet been studied in detail for other areas of basement in Oman it would be likely that these areas experienced similar thermal gradients during metamorphism, based on the noted similarity between basement exposures and interpreted setting of formation (Gass *et al.* 1990, Johnson & Woldehaimanot 2003, Mercogli *et al.* 2006, Allen 2007, Rantakokko *et al.* 2014). It is noted that the P - T paths and thermal gradients interpreted in this study, while generally of lower peak metamorphic grade, can be seen to follow clockwise paths similar to a variety of locations belonging to the Arabian-Nubian Shield as well as the Mozambique Belt (Fig. 22). It can further be seen in Figure 22 that the thermal gradient experienced by rocks in Jebel Ja'alan are comparable to those interpreted for the rocks in these other locations, suggesting a similar setting of metamorphism. As noted by Stern and Johnson (2010) and shown in the summary of previous geochronological data provided in Table 1, the basement rocks in Jebel Ja'alan are interpreted to be older than those found within Mirbat, in the country's south. The geochronological data gathered in this study is supportive of metamorphosed basement in Jebel Ja'alan being ~20 Ma older than that encountered in Mirbat. Possibly reflecting the progressive accretion of arc terranes during the Tonian. As noted by several authors, it is not currently possible to directly constrain the relationship between basement rock in Oman and the terranes observed in the Arabian-Nubian Shield, due to the presence of cover sequences between the two locations (Johnson & Woldehaimanot 2003, Collins & Pisarevsky 2005, Rantakokko *et al.* 2014). However, it can be observed that in the Arabian-Nubian shield there is accretion of juvenile arcs to the eastern margin of a growing African continent, containing rocks of similar metamorphic grade (Blasband *et al.* 1997, Jarrar *et al.* 2013) and much younger

age to those in Oman. During this time of accretion in the ANS we instead see the deposition of sedimentary sequences in Oman, interpreted to signify the cessation of arc accretion (Fig. 23). This suggests the margin of Neoproterozoic India had transitioned to a passive margin by the Cryogenian, with consumption of the Mozambique Ocean instead occurring at the African margin.

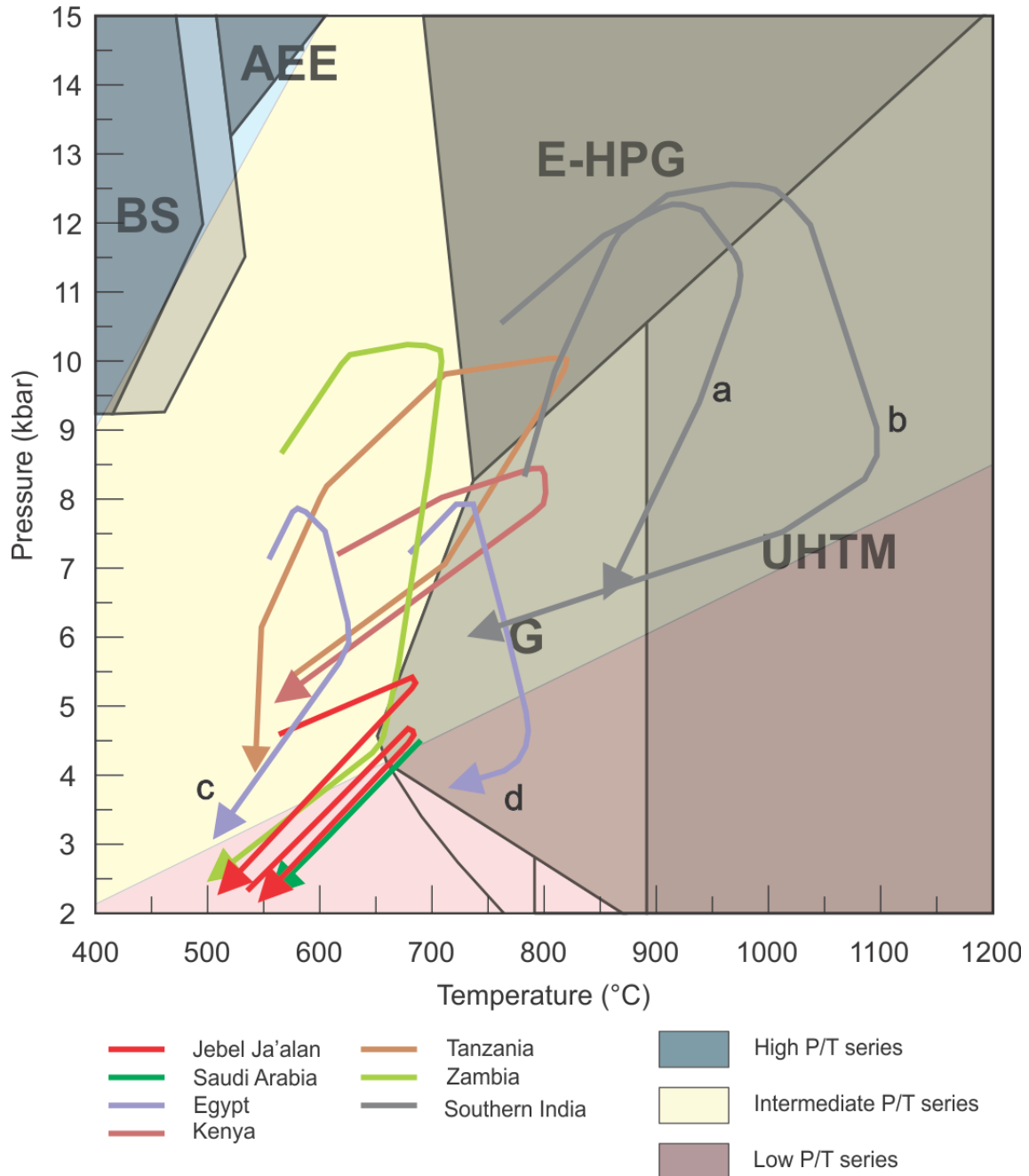


Figure 22. Summary of interpreted P - T paths from the Arabian-Nubian Shield, Oman, and locations related to the Mozambique belt. Paths are displayed upon background adapted from (Brown 2007a). Abbreviations: BS = blueschist; AEE = amphibole-epidote-eclogite facies; E-HPG = eclogite-high-pressure granulite; G = granulite facies; UHTM = ultrahigh-temperature metamorphic part of the granulite facies. P - T path references: Saudi Arabia: Abu-Alam *et al.* (2014); Kenya: Hauzenberger *et al.* (2004); Tanzania: Herms and Schenk (1998); Zambia: John *et al.* (2004); Southern India (a): Collins *et al.* (2007); Southern India (b): Brandt *et al.* (2011); Egypt (c): Fritz *et al.* (2002); Egypt (d): Abu El-Enen (2011).

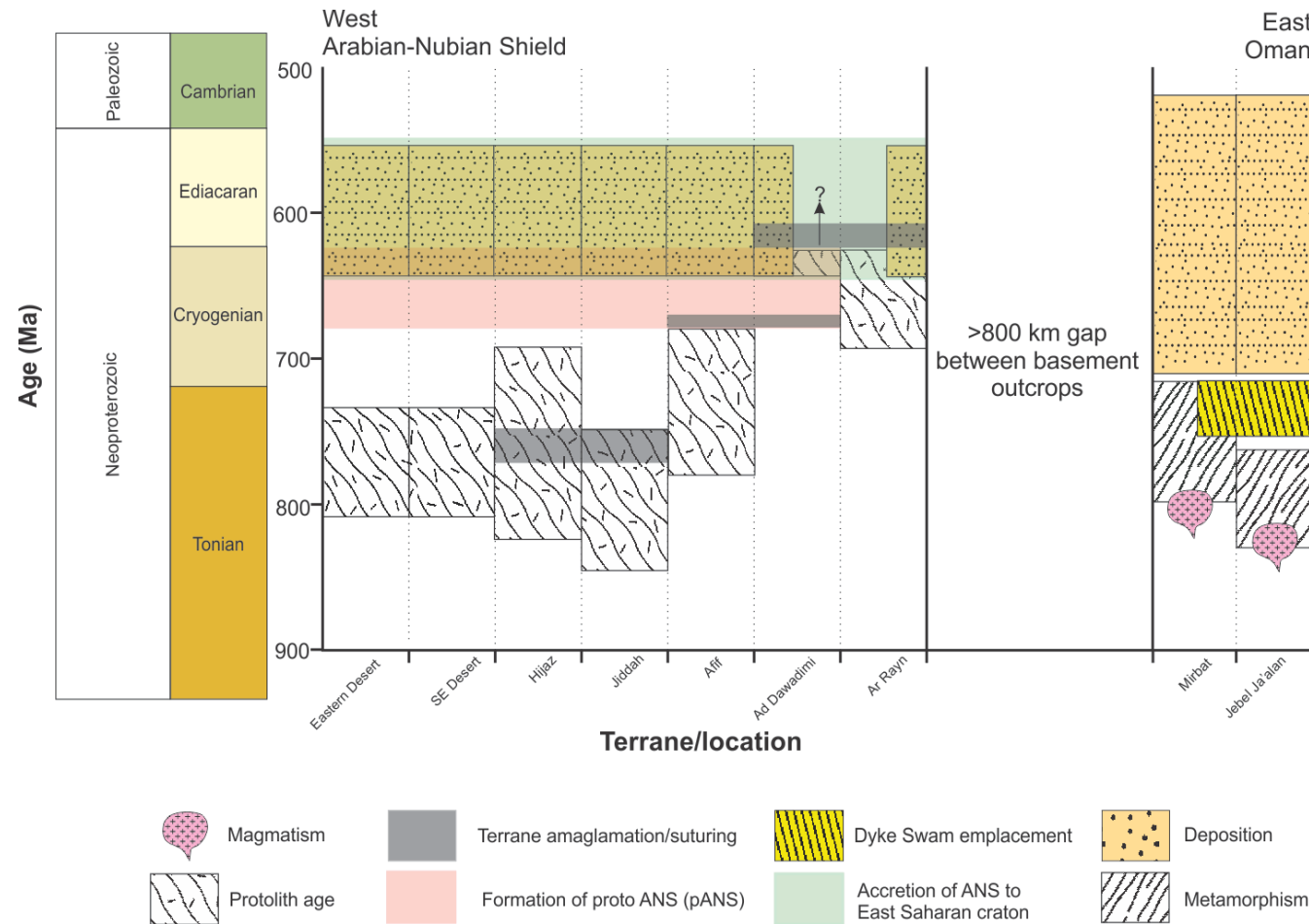


Figure 23. Time-space plot for Terranes in the Arabian-Nubian Shield and locations within Oman, with a gap between locations signifying a >800 km gap between the closest basement outcrops. A location map of terranes displayed in the plot is presented in Figure 24. It can be observed that both protolith ages and timing of suturing of terranes decreases to the modern day east of the ANS, reflecting amalgamation of younger arc terranes. The opposite trend can be seen within the Omani basement, with ages decreasing towards the modern day west. Furthermore, it can also be seen that accretion in Oman finished earlier than in the ANS, reflected in the earlier deposition of sediments. Ages in the ANS are from Johnson *et al.* (2011), Mirbat ages from Rantakokko *et al.* (2014)



Figure 24. Location map of the Arabian-Nubian Shield (ANS) and Oman (adapted from Blades *et al.* (2015)). The map shows terranes and locations used for the time-space plot presented in Figure 23.

CONCLUSIONS

Phase equilibria modelling in conjunction with U–Pb and ^{40}Ar – ^{39}Ar geochronological data suggests that basement rock in Jebel Ja'alan (east Oman) experienced a clockwise P – T path during the Tonian, reaching peak metamorphic conditions of c. 670–700 °C and 4.5–6 kbar. A calculated thermal gradient of approximately 116.7–148.9 °C/kbar is consistent with the basement forming in an active arc environment (though not exclusive to this setting), as suggested by previous authors (Gass *et al.* 1990, Worthing 2005). Results regarding the P – T conditions experienced by rocks in Jebel Ja'alan are the first of their kind for basement rock in Oman and are interpreted to be representative of other basement outcrops within the country. U–Pb monazite age data dates near peak P – T conditions of the Hassan Schist between ~845–830 Ma. ^{40}Ar – ^{39}Ar muscovite age data suggests a similar age of peak metamorphism, and also shows that this event was approximately coeval with emplacement and crystallisation of the Ja'alan Granite. The older age of metamorphic rocks from Jebel Ja'alan compared to similar rocks from Mirbat may be suggestive of a continual process of arc accretion.

The structures present within Jebel Ja'alan are indicative of two main deformational events occurring within the region. The first event resulted in structures indicative of a north-south compressional regime, which was contemporaneous with or slightly postdating peak metamorphism. In contrast, the second event involved an east–west compressional regime, the timing of which is difficult to constrain, though is likely to have occurred after the Maastrichtian due to the presence of similarly orientated structures being reported in the overlying sedimentary units.

ACKNOWLEDGMENTS

Supervisors Prof. Alan Collins and Dr David Kelsey are thanked for their invaluable support and guidance throughout this project. Morgan Blades is also thanked for her support, both emotional and academic, throughout the year. Prof Salah Al-Khribash from Sultan Qaboos University is thanked for logistical support provided during fieldwork in Oman. A. Prof. Fred Jourdan from Curtin University is thanked for the ^{40}Ar - ^{39}Ar work he conducted on samples. Aoife Mcfadden and Dr Ben Wade from Adelaide Microscopy are thanked for their help and support with SEM imaging, in addition to electron microprobe and LA-ICP-MS analyses.

REFERENCES

- ABU-ALAM T., HASSAN M., STÜWE K., MEYER S. & PASSCHIER C. 2014. Multistage Tectonism and Metamorphism During Gondwana Collision: Baladiyah Complex, Saudi Arabia. *Journal of Petrology*, egu046.
- ABU EL-ENEN M. M. 2011. Geochemistry, provenance, and metamorphic evolution of Gabal Samra Neoproterozoic metapelites, Sinai, Egypt. *Journal of African Earth Sciences* **59**, 269-282.
- ALLEN P. A. 2007. The Huqf Supergroup of Oman: basin development and context for Neoproterozoic glaciation. *Earth-Science Reviews* **84**, 139-185.
- ALLMENDINGER R. W., CARDOZO N. & FISHER D. M. 2011. *Structural geology algorithms: Vectors and tensors*. Cambridge University Press.
- BARD J. P. 1983. Metamorphism of an obducted island arc: example of the Kohistan sequence (Pakistan) in the Himalayan collided range. *Earth and Planetary Science Letters* **65**, 133-144.
- BLADES M. L., COLLINS A. S., FODEN J., PAYNE J. L., XU X., ALEMU T., WOLDETINSAE G., CLARK C. & TAYLOR R. J. 2015. Age and Hafnium Isotopic Evolution of the Didesa and Kemashi Domains, Western Ethiopia. *Precambrian Research*.
- BLASBAND B., BROOIJMANS P., DIRKS P., VISSER W. & WHITE S. 1997. A Pan-African core complex in the Sinai, Egypt. *Geologie en Mijnbouw* **76**, 247-266.
- BOWRING S. A., GROTZINGER J. P., CONDON D. J., RAMEZANI J., NEWALL M. J. & ALLEN P. A. 2007. Geochronologic constraints on the chronostratigraphic framework of the Neoproterozoic Huqf Supergroup, Sultanate of Oman. *American Journal of Science* **307**, 1097-1145.
- BRANDT S., SCHENK V., RAITH M., APPEL P., GERDES A. & SRIKANTAPPA C. 2011. Late Neoproterozoic PT evolution of HP-UHT granulites from the Palni Hills (South India): New constraints from phase diagram modelling, LA-ICP-MS zircon dating and in-situ EMP monazite dating. *Journal of Petrology* **52**, 1813-1856.
- BROWN M. 1993. P-T-t evolution of orogenic belts and the causes of regional metamorphism. *Journal of the Geological Society* **150**, 227-241.
- BROWN M. 2007a. Metamorphic conditions in orogenic belts: a record of secular change. *International Geology Review* **49**, 193-234.
- BROWN M. 2007b. Metamorphism, Plate Tectonics, and the Supercontinent Cycle. *Earth Science Frontiers* **14**, 1-18.
- CARDOZO N. & ALLMENDINGER R. W. 2013. Spherical projections with OSXStereonet. *Computers & Geosciences* **51**, 193-205.

- COLLINS A. S., CLARK C., SAJEEV K., SANTOSH M., KELSEY D. E. & HAND M. 2007. Passage through India: the Mozambique Ocean suture, high-pressure granulites and the Palghat-Cauvery shear zone system. *Terra Nova* **19**, 141-147.
- COLLINS A. S. & PISAREVSKY S. A. 2005. Amalgamating eastern Gondwana: the evolution of the Circum-Indian Orogens. *Earth-Science Reviews* **71**, 229-270.
- CORFU F., HANCHAR J. M., HOSKIN P. W. & KINNY P. 2003. Atlas of zircon textures. *Reviews in mineralogy and geochemistry* **53**, 469-500.
- CORRIE S. L. & KOHN M. J. 2008. Trace-element distributions in silicates during prograde metamorphic reactions: Implications for monazite formation. *Journal of Metamorphic Geology* **26**, 451-464.
- FILBRANDT J., NOLAN S. & RIES A. 1990. Late Cretaceous and early Tertiary evolution of Jebel Ja'alan and adjacent areas, NE Oman. *Geological Society, London, Special Publications* **49**, 697-714.
- FITTON J. & GILL R. 1970. The oxidation of ferrous iron in rocks during mechanical grinding. *Geochimica et Cosmochimica Acta* **34**, 518-524.
- FRITZ H., DALLMEYER D. R., WALLBRECHER E., LOIZENBAUER J., HOINKES G., NEUMAYR P. & KHUDEIR A. A. 2002. Neoproterozoic tectonothermal evolution of the Central Eastern Desert, Egypt: a slow velocity tectonic process of core complex exhumation. *Journal of African Earth Sciences* **34**, 137-155.
- GASS I., RIES A., SHACKLETON R. & SMEWING J. 1990. Tectonics, geochronology and geochemistry of the Precambrian rocks of Oman. *Geological Society, London, Special Publications* **49**, 585-599.
- HAUZENBERGER C., BAUERNHOFER A., HOINKES G., WALLBRECHER E. & MATHU E. 2004. Pan-African high pressure granulites from SE-Kenya: petrological and geothermobarometric evidence for a polycyclic evolution in the Mozambique belt. *Journal of African Earth Sciences* **40**, 245-268.
- HERMS P. & SCHENK V. 1998. Fluid inclusions in high-pressure granulites of the Pan-African belt in Tanzania (Uluguru Mts): a record of prograde to retrograde fluid evolution. *Contributions to Mineralogy and Petrology* **130**, 199-212.
- HOLLAND T. & POWELL R. 2011. An improved and extended internally consistent thermodynamic dataset for phases of petrological interest, involving a new equation of state for solids. *Journal of Metamorphic Geology* **29**, 333-383.
- IMMENHAUSER A., SCHREURS G., GNOS E., OTERDOOM H. W. & HARTMANN B. 2000. Late Palaeozoic to Neogene geodynamic evolution of the northeastern Oman margin. *Geological Magazine* **137**, 1-18.
- JACKSON S. E., PEARSON N. J., GRIFFIN W. L. & BELOUSOVA E. A. 2004. The application of laser ablation-inductively coupled plasma-mass spectrometry to in situ U-Pb zircon geochronology. *Chemical Geology* **211**, 47-69.
- JARRAR G. H., THEYE T., YASEEN N., WHITEHOUSE M., PEASE V. & PASSCHIER C. 2013. Geochemistry and P-T-t evolution of the Abu-Barqa Metamorphic Suite, SW Jordan, and implications for the tectonics of the northern Arabian-Nubian Shield. *Precambrian Research* **239**, 56-78.
- JOHN T., SCHENK V., MEZGER K. & TEMBO F. 2004. Timing and PT evolution of whiteschist metamorphism in the Lufilian Arc-Zambezi Belt orogen (Zambia): implications for the assembly of Gondwana. *The Journal of geology* **112**, 71-90.
- JOHNSON P., ANDRESEN A., COLLINS A., FOWLER A., FRITZ H., GHEBREAB W., KUSKY T. & STERN R. 2011. Late Cryogenian-Ediacaran history of the Arabian-Nubian Shield: a review of depositional, plutonic, structural, and tectonic events in the

- closing stages of the northern East African Orogen. *Journal of African Earth Sciences* **61**, 167-232.
- JOHNSON P. R. & WOLDEHAIMANOT B. 2003. Development of the Arabian-Nubian Shield: perspectives on accretion and deformation in the northern East African Orogen and the assembly of Gondwana. *Geological Society, London, Special Publications* **206**, 289-325.
- JOURDAN F. & RENNE P. R. 2007. Age calibration of the Fish Canyon sanidine $^{40}\text{Ar}/^{39}\text{Ar}$ dating standard using primary K–Ar standards. *Geochimica et Cosmochimica Acta* **71**, 387-402.
- KELSEY D. E. & HAND M. 2015. On ultrahigh temperature crustal metamorphism: Phase equilibria, trace element thermometry, bulk composition, heat sources, timescales and tectonic settings. *Geoscience Frontiers* **6**, 311-356.
- KIL Y. & JUNG H. 2015. LA-ICP-MS analysis of natural rock samples using XRF glass beads. *Geosciences Journal* **19**, 45-52.
- KRÖNER A. & STERN R. J. 2004. Pan-African Orogeny. *Encyclopedia of Geology* **1**, 1-12.
- LEE J.-Y., MARTI K., SEVERINGHAUS J. P., KAWAMURA K., YOO H.-S., LEE J. B. & KIM J. S. 2006. A redetermination of the isotopic abundances of atmospheric Ar. *Geochimica et Cosmochimica Acta* **70**, 4507-4512.
- LI Z.-X., BOGDANOVA S., COLLINS A., DAVIDSON A., DE WAELE B., ERNST R., FITZSIMONS I., FUCK R., GLADKOCHUB D. & JACOBS J. 2008. Assembly, configuration, and break-up history of Rodinia: a synthesis. *Precambrian Research* **160**, 179-210.
- MEERT J. G. 2003. A synopsis of events related to the assembly of eastern Gondwana. *Tectonophysics* **362**, 1-40.
- MEERT J. G. & LIEBERMAN B. S. 2008. The Neoproterozoic assembly of Gondwana and its relationship to the Ediacaran–Cambrian radiation. *Gondwana Research* **14**, 5-21.
- MERCOLLI I., BRINER A. P., FREI R., SCHÖNBERG R., NÄGLER T. F., KRAMERS J. & PETERS T. 2006. Lithostratigraphy and geochronology of the Neoproterozoic crystalline basement of Salalah, Dhofar, Sultanate of Oman. *Precambrian Research* **145**, 182-206.
- MORRISSEY L. J., HAND M. & KELSEY D. E. 2015. Multi-stage metamorphism in the Rayner–Eastern Ghats Terrane: P–T–t constraints from the northern Prince Charles Mountains, east Antarctica. *Precambrian Research* **267**, 137-163.
- MURRAY G. 2015. The Geochemistry of the Neoproterozoic Basement of Jebel Ja'alan, East Oman. Honors Thesis. *University of Adelaide (Unpublished)*.
- PAYNE J., HAND M., BAROVICH K. & WADE B. 2008. Temporal constraints on the timing of high-grade metamorphism in the northern Gawler Craton: implications for assembly of the Australian Proterozoic. *Australian Journal of Earth Sciences* **55**, 623-640.
- PISAREVSKY S. A., MURPHY J. B., CAWOOD P. A. & COLLINS A. S. 2008. Late Neoproterozoic and Early Cambrian palaeogeography: models and problems. *Geological Society, London, Special Publications* **294**, 9-31.
- POWELL R., WHITE R., GREEN E., HOLLAND T. & DIENER J. 2014. On parameterizing thermodynamic descriptions of minerals for petrological calculations. *Journal of Metamorphic Geology* **32**, 245-260.

- RANTAKOKKO N. E., WHITEHOUSE M. J., PEASE V. & WINDLEY B. F. 2014. Neoproterozoic evolution of the eastern Arabian basement based on a refined geochronology of the Marbat region, Sultanate of Oman. *Geological Society, London, Special Publications* **392**, 107-127.
- RENNE P. R., MUNDIL R., BALCO G., MIN K. & LUDWIG K. R. 2010. Joint determination of 40 K decay constants and 40 Ar*/40 K for the Fish Canyon sanidine standard, and improved accuracy for 40 Ar/39 Ar geochronology. *Geochimica et Cosmochimica Acta* **74**, 5349-5367.
- RIES A. & SHACKLETON R. 1990. Structures in the Huqf-Haushi Uplift, east Central Oman. *Geological Society, London, Special Publications* **49**, 653-663.
- RIEU R., ALLEN P. A., COZZI A., KOSLER J. & BUSSY F. 2007. A composite stratigraphy for the Neoproterozoic Huqf Supergroup of Oman: integrating new litho-, chemo- and chronostratigraphic data of the Mirbat area, southern Oman. *Journal of the Geological Society* **164**, 997-1009.
- ROLANDONE F., LUCAZEAU F., LEROY S., MARESCHAL J.-C., JORAND R., GOUTORBE B. & BOUQUEREL H. 2013. New heat flow measurements in Oman and the thermal state of the Arabian Shield and Platform. *Tectonophysics* **589**, 77-89.
- SHACKLETON R. & RIES A. 1990. Tectonics of the Masirah fault zone and eastern Oman. *Geological Society, London, Special Publications* **49**, 715-724.
- SMITH H. A. & BARREIRO B. 1990. Monazite U-Pb dating of staurolite grade metamorphism in pelitic schists. *Contributions to Mineralogy and Petrology* **105**, 602-615.
- STERN R. J. & JOHNSON P. 2010. Continental lithosphere of the Arabian Plate: a geologic, petrologic, and geophysical synthesis. *Earth-Science Reviews* **101**, 29-67.
- THORPE B. 2015. The Structure and Provenance of the Neoproterozoic Basement of Jebel Ja'alan, East Oman. Honors Thesis. *University of Adelaide (Unpublished)*.
- TUCCILLO M., ESSENE E. & VAN DER PLUIJM B. 1990. Growth and retrograde zoning in garnets from high-grade, metapelites: Implications for pressure-temperature paths. *Geology* **18**, 839-842.
- WATERS D. & CHARNLEY N. 2002. Local equilibrium in polymetamorphic gneiss and the titanium substitution in biotite. *American mineralogist* **87**, 383-396.
- WHITE R., POWELL R., HOLLAND T., JOHNSON T. & GREEN E. 2014. New mineral activity–composition relations for thermodynamic calculations in metapelitic systems. *Journal of Metamorphic Geology* **32**, 261-286.
- WHITNEY D. L. & EVANS B. W. 2010. Abbreviations for names of rock-forming minerals. *American mineralogist* **95**, 185.
- WING B. A., FERRY J. M. & HARRISON T. M. 2003. Prograde destruction and formation of monazite and allanite during contact and regional metamorphism of pelites: petrology and geochronology. *Contributions to Mineralogy and Petrology* **145**, 228-250.
- WORTHING M. 2005. Petrology and geochronology of a Neoproterozoic dyke swarm from Marbat, South Oman. *Journal of African Earth Sciences* **41**, 248-265.
- WÜRSTEN F., FLISCH M., MICHALSKI I., LE MÉTOUR J., MERCOLLI I., MATTHÄUS U. & PETERS T. 1991. The Uplift History of the Precambrian Crystalline Basement of the Jabal J'alan (Sur Area). In, *Ophiolite Genesis and Evolution of the Oceanic Lithosphere*, pp 613-626, Springer.

ZHAO G., WILDE S. A., CAWOOD P. A. & SUN M. 2001. Archean blocks and their boundaries in the North China Craton: lithological, geochemical, structural and P–T path constraints and tectonic evolution. *Precambrian Research* **107**, 45-73.

APPENDIX A: SAMPLE SUMMARY

Seventeen samples were collected from the Jebel Ja'alan area in NE Oman, for use with petrographic, geochemical and geochronological analytical techniques. Samples were selected in the field to be made into thin sections for petrographic analysis based on the abundance of metamorphic minerals able to be observed in hand specimen, in order to assist in determining a P – T path when assemblages are plotted on a pseudosection.

Table 1. List of samples collected from Jebel Ja'alan, Oman. GPS references refer to WGS84 (zone 40N) and UTM coordinates.

Sample Number	Lithology	Weight (kg)	GPS	
JA15-02	Hassan Schist	0.55	742350	2460414
JA15-03	Ja'alan Granite	1.05	742350	2460414
JA15-04	Hassan Schist	0.35	742563	2460600
JA15-06	Hassan Schist	0.7	742573	2460575
JA15-08	Kamil Granodiorite	1.7	742899	2460099
JA15-09	Kamil Granidiorite	1.8	742927	2460090
JA15-10a	Ali Gneiss	1.65	742948	2460028
JA15-12	Kamil Granidiorite	1.25	744781	2451023
JA15-26	Ali Gneiss	1.55	743437	2459614
JA15-27	Hassan Schist	0.85	743645	2459110
JA15-28	Para-Amphibolite	1.1	743626	2458943
JA15-36	Ali Gneiss	0.4	743707	2459687
JA15-37	Ali Gneiss	1	743757	2459678
JA15-38	Para-Amphibolite	0.6	744439	2459934
JA15-40	Hassan Schist	1.15	741746	2460114
JA15-41	Hassan Schist	0.2	741483	2459925
JA15-43	Hassan Schist	0.3	741148	2460019

Mineral identification

HAND SPECIMEN

Samples were initially identified via visual inspection.

OPTICAL MICROSCOPY

A detailed petrographic analysis of the samples collected was undertaken using an Olympus BH-2 transmitting light optical microscope.

SCANNING ELECTRON MICROSCOPE

A Phillips XL30 scanning electron microscope (SEM) was used to determine the location and identity of in-situ monazite grains. This was done by observing and imaging thin sections in the backscattered electron mode of the microscope. Energy-dispersive X-ray spectroscopy (EDS) was undertaken using an EDAX EDS detector in order to correctly identify monazite grains.

A single sample (JA15-06) was identified using a Mineral Liberation Analysis (MLA) detector attached to a FEI Quanta 600 SEM, in order to determine the location and relationship of monazite to the rest of the minerals in the sample.

APPENDIX B: GEOCHRONOLOGY

Preparation

SAWING

1. Turn water supply to rock saw on.
2. For geochemistry: cut sample into no greater than approximately 5cmX5cmX4cm sections to run through jaw crusher.
3. For thin sections: cut sample into approximate 5cmX3cmX.5cm portions to be sent away.
4. Dry sample, either by leaving to dry on paper towels, or by placing on a hotplate with a paper towel between the sample and plate.
5. Place dried sample in labelled sample bag.

THIN SECTIONS

Seventeen samples were sent to Continental instruments (India). Thin-sections were made polished and uncovered. The following method was used.

1. First, a small slab is cut, approximately 25mm x 50mm, x 5mm thick, using a 250mm diameter rock-cutting saw blade with a continuous diamond rim. Four samples were impregnated with epoxy, due to their tendency to fracture.
2. A top surface on the slab, is manually ground flat on a bench-mounted, horizontal diamond grinding wheel Habit-brand, grit size 64.
3. The coarse ground top surface is warmed on a hot plate (at 50°C), and the top coarse-ground surface is impregnated with an epoxy mix of Araldite LC191 resin, with HY951 hardener, ratio 8:1. This surface is then manually more finely ground flat using 600 SiC grit, on a zinc-lap or glass plate, using water as

a lubricant. This flat finely ground surface is cleaned, checked manually for “perfection”, (if open porosity is still exposed another veneer of epoxy is applied), is then glued onto a clean, dry glass slide, ground to a known thickness, using a UV curing, cyanoacrylate liquid adhesive “Loctite Impruv 36331”. Exposure to a UV light of the glued interface through the back of the glass slide cures the adhesive in 2 to 3 minutes. This is a permanent bond, and the rock (or eventual wafer) cannot be ever separated from the glass.

4. The block mounted on glass is then cut off using a trim saw with a thin continuous diamond rimmed sawblade (Diatrenn E2-G), to leave a thickness of about 1mm of the sample slab (glued onto the glass slide), with the top surface exposed for further processing.
5. The 1mm slab thickness is further ground down on a diamond wheel (Habit D76) held within a special jig attachment by vacuum, using water as a lubricant. This reduces the slab thickness stuck on the glass, to a wafer of about 120 micron (0.12mm).
6. The glass slide of known thickness with the glued-on rock wafer is then loaded and held in place on the face of a special jig, and lapped flat on a Logitech machine, to a final petrographic thickness of the rock wafer, of 30 micron, using 600 SiC grit as the grinding abrasive, and water as a lubricant.
7. When the Logitech lapping cycle is finished, the quality of the wafer on the glass is assessed, also optically checked for the required 30 micron thickness, and when confirmed as correct, the section is cleaned and covered with a glass coverslip, using the same UV curing adhesive as listed above. Again this is a permanent fix, i.e. the coverslip cannot be removed. The final thin section is then again cleaned and labelled.

IMAGING

Thin sections were imaged using the backscattered electron mode of a Phillips XL30 scanning electron microscope. Low magnification images were taken to make a mosaic of the thin sections, while higher magnification images were taken of individual monazite grains to accompany the mosaic.

U–PB DATING

U–Pb data for in-situ monazites was obtained using LA-ICP-MS. The instruments used were an Agilent 7500cs and a New Wave UP213 Laser Ablation System. Monazite data were reduced using *GLITTER* software (Jackson *et al.* 2004). Elemental fractionation and mass bias were corrected using the monazite MADel (c. 518 Ma; Payne *et al.* 2008). Data accuracy was monitored using monazite standard 94-222/Bruna-NW (c. 450 Ma; Payne *et al.* 2008). Standard analyses are given in Table 7.

The following method from Adelaide Microscopy was used for obtaining U–Pb data:

Turning on the gases and inserting samples

1. Ensure ICP-MS is in standby mode.
2. Start ICP-MS top program and select the tune menu from the 'instrument' menu.
3. Loosen the screws on the laser ablation chamber door and slide the door to the left. The sample holder will then slide out.
4. Clean your samples and place them in the cell, ensuring they are held tightly.
5. Insert the cell into the chamber, close the door and tighten the screws.
6. Start ICP-MS top program (middle computer).
7. Select 'instrument control' from the instrument menu.
8. Select 'maintenance menu' then 'sample introduction'.
9. Check box 'optional gas' and type 60% for 'optional gas' and click on enter.
10. Open 'laser ablation' program on the NewWave computer (far right computer).
11. Click on 'evacuate' a dialogue box will pop up with a status bar, indicating number of cycles. The laser ablation chamber and then refilled with He in cycles.
12. Once finished click on 'evacuate' twice more. The system needs to do 30 cycles to remove all the air from the chamber.
13. Once finished ensure 'online' is selected in the laser ablation program.
14. Close 'sample introduction' dialogue in the ICP-MS top program. This action will reset the optional gas to 0%

Turning on the plasma

1. Select instrument > tune.
2. Select 'optional gas' slider bar (probably set at around 58%) and turn it down to 20%.
3. Select instrument > instrument control.
4. Select instrument > instrument control > start plasma.
5. Wait until the plasma is fully operational (all gauges green, approximately 2 minutes).
6. Go back to instrument > tune and turn optional gas back up to correct value (usually 58-59%).
7. Perform a maintenance log by carrying out the following steps:
 - a. On the 'instrument control' screen select the 'diagnostics log' menu and then 'log book'.
 - b. Make a note of the 'plasma on' time, then exit.
 - c. On the 'Instrument control' screen select the 'maintenance log' menu then 'log book'.
 - d. Double click on one of the previous logs, select and copy the information in the 'comments' box. Click close.
 - e. Click 'record log' and paste copied data into the 'comments' box, then add in today's details including the 'plasma on' time you made a note of.
 - f. Click 'ok' then 'exit'.
8. Select instrument > tune

Load method

1. On the Chemstation computer select the methods menu, load.
2. For example select BenZirc.M for zircon dating, or BenMnz.M for monazite dating, etc and click ok.
3. Choose the equivalent calibration file (with a C extension) and click ok.
4. In laser ablation mode (compared to solution ICP-MS) the calibration file is not used however the software will still require this file, if no equivalent calibration file can be found then select Default.C

PA factor

The PA factor allows the ICP-MS software to process signals acquired by the detector in pulse count mode and analogue mode with seamless/linear calibration. This transition in the way the signal is measured occurs when counts per second exceed approximately one million. Thus the PA factor is not required every time the system is run, only when you expect cps to exceed approximately one million in your unknown (note: always perform a PA factor if attempting geochronology, as counts in zircon and monazite typically exceed one million). When conducting a PA factor what we are attempting to do is trip the detector into analogue counting mode by obtaining over a million counts in at least two elements at opposite ends of the mass spectrum you are analysing. We do this by increasing the spot size and intensity of the laser, and ablate a high concentration NIST glass.

1. Move to Nist 610 (High concentration NIST, dark blue glass).
2. Initially, change the beam to 65 μm and increase frequency to 10Hz.
3. To view the counts on the detector of specific isotopes click on the 'Acq. Params' menu, acquisition parameters, and tick 80, 206, 248/232, 207, 208, 204, 238, 220, click ok. These isotopes will now appear on the tune screen.
4. Start laser firing, click start on the tune screen.
5. When over one million counts in ^{238}U and ^{208}Pb click stop on the tune panel, select tune > P/A factor > click 'load masses from Acq. Method' > run. (Note: If unable to obtain over one million counts, try an 80 μm beam diameter. If sensitivity continues to be too low, try increasing the beam intensity).
6. When the notepad automatically pops up, check that ^{238}U and ^{208}Pb are in detection range (they will have a number next to them, usually about 0.9), then click 'yes' to a new P/A factor, click save. (Note: if there are no numbers next to any of the masses, and you did have over a million counts in the tune screen, it could be that you didn't perform step 5 fast enough and the counts dropped below a million. Simply repeat step 5).
7. Stop laser firing, close shutter.
8. Turn the settings back to normal, 5Hz for laser fire rate, and 15 μm (monazite) or 30-50 μm (zircon) for spot size and 65% intensity.

Setting up the laser ablation system

1. Open 'laser ablation' program on the NewWave computer.
2. Turn up light intensity and choose COAX mode of sample illumination.

3. Choose 5Hz for laser fire frequency/rate.
4. Select a laser spot size dependent on your method of analysis (e.g 8-15 μm for monazite, 30 μm for zircon).
5. Select a power rating (e.g. 70-80% for monazite, 60-80% for zircon). This value is a percentage of the maximum power available, and the value you choose will be dependent on your required spot size and concentration of elements of interest in your sample. Ask an AM staff member if unsure.
6. In order to view the sample surface, the user can adjust the optical zoom. To locate samples use a zero value for the optical zoom, when using the laser increase this zoom to 50% (zircon or thin sections) or 75% (monazite).

Running the method

The analytical method for laser ablation starts with the user running a number of standards. The first of these standards will be recognized by the '*Glitter*' software and when loaded into a '*Glitter*' processing session will be assigned with a star (*) and data associated with them.

The standards allow the calibration of laser ablation data in two ways:

- These standards will be used to measure the ablation yield i.e. the amount of material ablated by the laser settings selected.
- Drift in signal over the period of the analyses and degree of fractionation.

Some standards (internal standards) are run as "unknowns". By analysing material of known composition or age, we can evaluate whether or not our selected standard analyses are valid.

Manual Acquisition

1. Firstly ICP-MS top must be configured for manual acquisition. Close out of ICP-MS top and open up 'configuration' from the desktop. Under 'remote start' check on 'do not use'. Click save and then reopen ICP-MS top.
2. A folder on D: drive needs to be created to store your data. If not already created, create a folder. Within this folder is where all your data will now be stored, however you should create a new folder within this one for each new sample.
3. Move the laser ablation cell x- and y- location to the first standard, ensure the laser shutter is closed.
4. To run the method select 'method' > 'run' from the *Chemstation* software.
5. Enter the path of the data where the files are going to be stored, this path can be copied and pasted from Microsoft explorer. At the end of this path is where you enter the name of the spot analysis (*Chemstation* creates a folder of data with this name for each laser ablation analysis).
6. Thus for every spot after that for this specific sample you would only need to modify the spot name, and leave the path directory as it is.
7. Click 'run method' and view the time elapsed value displayed on the screen. The first part of the run will be the background. The laser shutter is then opened and the laser fired. (Ask AM staff for assistance with background collection time and acquisition time).

8. The method must run to its full completion for the acquired data to be saved, thus if for example you drill through your material, you can stop the laser firing however you must let the method run to completion for the data to be stored.
9. Once the method has finished it will exit back to the tune screen. Stop the laser firing and close the shutter ready for the next analysis.
10. The data is now ready to be viewed in the glitter program.

Using Glitter

1. Open the *Glitter* program from the desktop of the far left computer.
2. Choose 'isotope ratios' when conducting geochronology.
3. To load your data files into glitter, select 'file' > 'load data', and navigate to the I: drive. This is taking the data from the central computer across the network. Then navigate to the root directory of where all your spot analyses are being stored (e.g. D:\username\samplename\), then click ok.
4. A window will then pop up in which the user must set the detector dwell times which have been setup in the method on Chemstation, e.g. for zircon and monazite dating the following dwell times are common and need to be changed in the glitter standards window for each new glitter session. It is critical that the dwell times in the ICP method match those in the glitter standards window.
5. Dwell times for zircon and monazite dating:
 - a. Isotope: 204 Dwell time in msec: 10
 - b. Isotope: 206 Dwell time in msec: 15
 - c. Isotope: 207 Dwell time in msec: 30
 - d. Isotope: 208 Dwell time in msec: 10
 - e. Isotope: 232 Dwell time in msec: 10
 - f. Isotope: 238 Dwell time in msec: 15
6. Click accept, and accept again, and then ok to the next box that pops up.
7. Then choose 'display' > 'age estimates' to display the spot ages.
8. Select 'review signal selection' from the 'window' pull down menu. This window is where you choose to integrate both the background counts, and signal counts from.
9. If conducting standards check that the ages/concentrations match those from the standard block section.
10. After a series of standards have been analysed the glitter program will prompt the user for a different routine for processing the standard/calibration data. To begin with choose 'linear fit to ratios' in the windows options drop down list and then click the close options window. The user may wish to select 'tie standard markers to analyses' in the second drop down list.

Table 2. U–Pb ages for monazite standards analysed during collection of data.

JA15-04						
Analysis	Pb²⁰⁷/Pb²⁰⁶ age		Pb²⁰⁶/U²³⁸ age		Pb²⁰⁷/U²³⁵ age	
STDMAD01	617.6	31.35	513.5	7.04	532.8	7.06
STDMAD02	479.5	29.33	514	6.83	507.5	6.29
STDMAD03	485.1	29.74	488	6.51	487.3	6.15
22204	415.9	31.92	439	6.02	435.1	6
22205	439.4	31.07	424.6	5.83	426.7	5.84
22206	491.8	33.12	427.9	5.95	437.9	6.2
STDMAD07	497.6	28.14	545.8	7.07	536.5	6.32
STDMAD08	524.1	36.35	515.6	7.27	516.9	7.61
STDMAD09	465.5	30.8	546.8	7.34	531.2	6.77
22210	543.5	41.02	513.5	7.48	518.7	8.45
STDMAD23	478.1	31.08	530.6	7.2	520.6	6.76
STDMAD24	518.7	43.21	505	7.44	507.3	8.66
STDMAD25	1518.5	32.63	523.8	7.68	754.5	10.47
22226	437.6	37.06	428.3	6.15	429.7	6.75
22227	487.4	36.08	417	5.93	428	6.51
22228	522.8	32.67	465.6	6.52	475.2	6.64
STDMAD29	486	32.14	515.5	7.06	509.9	6.83
STDMAD30	489.8	32.3	502.6	6.91	500.2	6.77
JA15-06						
Analysis	Pb²⁰⁷/Pb²⁰⁶ age		Pb²⁰⁶/U²³⁸ age		Pb²⁰⁷/U²³⁵ age	
STDMAD01	472.8	45.49	518.7	8	510.1	9.04
STDMAD02	499.8	40.91	525.6	7.99	520.6	8.63
STDMAD03	511.8	42.4	507.1	7.76	507.8	8.63
22201	615.6	51.07	601.3	9.57	603.9	11.56
22202	576.6	41.67	577.9	8.91	577.3	9.58
22203	478.3	43.04	440.9	6.89	446.9	7.9
22204	506.4	42.51	444.7	6.95	454.7	7.97
22205	446.2	40.98	436.9	6.74	438.3	7.55
STDMAD04	501.3	42.32	522.8	8.21	518.7	8.85
STDMAD05	484	43.33	523.2	8.25	515.9	8.97
STDMAD06	483	45.49	509	8.08	504.3	9.15
22206	430.4	46.84	456.4	7.3	452	8.6
22207	450.8	57.16	444.7	7.44	445.6	9.97
22208	377.9	52.19	453.9	7.37	441.5	9.07
22209	445.5	52.27	462.3	7.59	459.4	9.52
JA15-40						
Analysis	Pb²⁰⁷/Pb²⁰⁶ age		Pb²⁰⁶/U²³⁸ age		Pb²⁰⁷/U²³⁵ age	
STDMAD01	492.3	47.68	525.5	8.28	519.3	9.68
STDMAD02	471.9	48.25	515	8.11	507.1	9.5

STDMAD03	402.9	48.14	506.7	7.99	488.2	9.26
STDMAD04	492.8	47.97	512.6	8.11	508.9	9.6
22201	484.3	48.12	451.6	7.17	456.9	8.8
22202	475	50.33	450.9	7.21	454.9	9.05
22203	514.9	47.15	439.9	6.99	452	8.61
STDMAD05	471.8	42.42	530.8	8.36	519.7	8.92
STDMAD06	412.4	59.52	516.7	8.68	497.8	11.27
STDMAD07	497.9	43.69	508.9	8.1	506.8	9.06
STDMAD08	485.4	53.16	516.4	8.58	510.6	10.58
22204	443.4	47.92	452.8	7.27	451.1	8.78
22205	519.5	43.99	446.3	7.06	458.2	8.32
22206	468	48.46	444.5	7.17	448.3	8.75
22207	470.5	58.3	441	7.41	445.7	10.15
JA15-43						
Analysis	Pb²⁰⁷/Pb²⁰⁶ age		Pb²⁰⁶/U²³⁸ age		Pb²⁰⁷/U²³⁵ age	
STDMAD01	510.9	37.2	522.8	7.66	520.5	7.93
STDMAD02	489.8	36.33	518.9	7.56	513.5	7.66
STDMAD03	494.7	37.19	508.2	7.44	505.7	7.73
22204	444.4	35.18	443	6.48	443.1	6.73
22205	438.6	36.41	442.9	6.51	442.1	6.88
22206	446.4	31.76	434.9	6.3	436.5	6.24
STDMAD14	476.5	43.82	545.8	8.39	532.4	9.18
STDMAD15	870.6	29.93	539.8	8.04	607.9	8.22
STDMAD16	2984.9	22.17	737.4	10.87	1565.4	14.15
STDMAD17	555.1	33.98	517.1	7.84	521.2	7.93
STDMAD18	629.5	51.74	521.5	8.57	532.8	11.28
22219	491.6	40.75	455.7	7.03	461.6	7.9
22220	420.7	45.09	457.3	7.21	451.2	8.43
22221	459	43.35	456.5	7.15	456.7	8.18

Table 3. U-Pb monazite ages for unknown samples presented in concordia diagrams.

JA15-04													
Analysis	Pb207/U235		Pb206/U238		rho	Concordancy	Recalc Rho	Pb206/U238		Pb207/U235		Pb206/Pb207	
12	1.33192	0.02062	0.14272	0.00201	0.909705	100	0.643194	860	11.36	859.7	8.98	860	25.7
13	1.26803	0.02474	0.13783	0.00209	0.777199	100	0.522299	832.4	11.83	831.5	11.08	831.5	35.87
15	1.34049	0.02022	0.14394	0.00202	0.930363	100	0.663482	866.9	11.39	863.4	8.77	856.2	24.7
16	1.24976	0.02184	0.13514	0.00196	0.829939	101	0.570596	817.1	11.12	823.3	9.86	841	30.92
17	1.33906	0.02092	0.14558	0.00204	0.896947	98	0.635568	876.1	11.49	862.8	9.08	830	26.47
22	1.29123	0.02094	0.13804	0.00198	0.884478	101	0.629678	833.6	11.23	841.8	9.28	864.9	27.27
19	1.38903	0.02417	0.15069	0.00222	0.846649	98	0.595599	904.8	12.46	884.3	10.27	835.2	30.07
20	1.29736	0.02044	0.14079	0.002	0.90165	99	0.644398	849.1	11.31	844.6	9.03	833.9	26.3
JA15-06													
Analysis	Pb207/U235		Pb206/U238		rho	Concordancy	recalc rho	Pb206/U238		Pb207/U235		Pb207/Pb206	
3	1.24723	0.0236	0.13641	0.00213	0.825217	100	0.586722	824.3	12.1	822.2	10.66	817.6	32.92
4	1.23597	0.02264	0.13508	0.00213	0.860835	100	0.626438	816.8	12.09	817.1	10.28	819	30.74
5	1.22285	0.02285	0.1343	0.00211	0.840801	100	0.60915	812.4	11.99	811.1	10.44	808.6	31.98
6	1.28005	0.02421	0.13972	0.00219	0.828739	99	0.596956	843.1	12.42	836.9	10.78	821.6	32.66
7	1.20648	0.02306	0.13445	0.00212	0.824966	99	0.595289	813.2	12.06	803.6	10.61	778	33.26
8	1.23844	0.02318	0.13854	0.00217	0.836847	98	0.602347	836.4	12.3	818.2	10.51	769.8	32.33
9	1.27288	0.02803	0.14014	0.00227	0.735577	99	0.493613	845.5	12.86	833.7	12.52	803	40.95
10	1.27394	0.02936	0.14066	0.00231	0.712581	98	0.47548	848.4	13.05	834.2	13.11	797.3	43.52
11	1.27775	0.02659	0.13941	0.00223	0.768667	99	0.537665	841.3	12.64	835.9	11.86	822.4	37.61

12	1.24836	0.02555	0.13686	0.00219	0.781838	99	0.553416	826.9	12.44	822.7	11.54	812.3	36.67
13	1.24895	0.02842	0.13733	0.00225	0.720009	99	0.484634	829.5	12.75	822.9	12.83	805.6	42.68
JA15-40													
Analysis	Pb207/U235		Pb206/U238		rho	Concordancy	recalc rho	Pb206/U238		Pb207/U235		Pb207/Pb206	
1	1.30596	0.03128	0.1399	0.00233	0.695347	100	0.451965	844.1	13.16	848.3	13.77	860.4	45.25
2	1.26809	0.03142	0.1394	0.00235	0.680376	99	0.440172	841.2	13.28	831.5	14.06	806.4	47.54
3	1.27879	0.03131	0.13833	0.00232	0.684996	100	0.447048	835.2	13.14	836.3	13.95	840	46.59
4	1.17925	0.02415	0.13185	0.00212	0.785135	99	0.56103	798.4	12.08	791	11.25	771.3	36.69
5	1.23739	0.02913	0.12934	0.00215	0.706109	104	0.464443	784.1	12.26	817.7	13.22	911	43.85
6	1.30244	0.02857	0.13787	0.00224	0.740672	102	0.501124	832.6	12.71	846.8	12.6	885	40.06
7	1.28671	0.03026	0.13834	0.00228	0.700808	101	0.468407	835.2	12.94	839.8	13.44	852.9	44.13
JA15-43													
Analysis	Pb207/U235		Pb206/U238		rho	Concordancy	recalc rho	Pb206/U238		Pb207/U235		Pb207/Pb206	
10	1.38545	0.02308	0.14649	0.00221	0.905606	100	0.670442	881.3	12.4	882.8	9.83	887.9	26.48
11	1.29439	0.02324	0.13748	0.0021	0.850763	102	0.614763	830.4	11.9	843.2	10.28	878.5	30.25
13	1.29062	0.0215	0.14167	0.00212	0.898293	99	0.65037	854.1	11.95	841.6	9.53	809.7	27.52

⁴⁰AR-³⁹AR DATING

Four samples of muscovite separate were sent away for ⁴⁰Ar/³⁹Ar dating at the Western Australian Argon Isotope Facility, Curtin University, Perth, Australia. Mica was separated by using the “paper shaking” technique on grains >79 μm. This method involves shaking grains on an inclined sheet of paper, mica grains will stick to the sheet while other grains will fall. Muscovite was then hand-picked from the separate, with the grains picked ideally being inclusion free.

The following method was used for obtaining ⁴⁰Ar/³⁹Ar data:

Samples were loaded into wells and bracketed by small wells that included Fish Canyon sanidine (FCs) used as a neutron monitor for which an age of 28.305 ± 0.036 Ma (1σ) was assigned (Renne *et al.* 2010) based on the calibration by Jourdan and Renne (2007). The discs are irradiated for x hours in the Hamilton McMaster University nuclear reactor (Canada). The mean J-values computed from standard grains within the small pits was $0.01058900 \pm 0.00000635$ determined as the average and standard deviation of J-values of the small wells for each irradiation disc. Mass discrimination was monitored using an automated air pipette and provided a mean value of 1.00646 ± 0.00238 per dalton (atomic mass unit) relative to an air ratio of 298.56 ± 0.31 (Lee *et al.* 2006). The correction factors for interfering isotopes were $(^{39}\text{Ar}/^{37}\text{Ar})\text{Ca} = 7.30 \times 10^{-4}$ ($\pm 11\%$), $(^{36}\text{Ar}/^{37}\text{Ar})\text{Ca} = 2.82 \times 10^{-4}$ ($\pm 1\%$) and $(^{40}\text{Ar}/^{39}\text{Ar})\text{K} = 6.76 \times 10^{-4}$ ($\pm 32\%$). The samples were step-heated using a 110 W Spectron Laser Systems, with a continuous Nd-YAG (IR; 1064 nm) laser. Ar isotopes were measured in static mode using a MAP 215-50 mass spectrometer (resolution of ~500 unit resolution; sensitivity of 4×10^{-14} mol/V) with a Balzers SEV 217 electron multiplier mostly using 9 to 10 cycles of peak-hopping. ⁴⁰Ar blanks range from 1×10^{-16} to 2×10^{-16} mol. Individual errors are given at the 1σ . The plateaus must include at least 70% of ³⁹Ar. The plateau should be distributed over a minimum of 3 consecutive steps agreeing at 95% confidence level and satisfying a probability of fit (P) of at least 0.05. Plateau ages are given at the 2σ level and are calculated using the mean of all the plateau steps, each weighted by the inverse variance of their individual analytical error. Mini-plateaus are defined similarly except that they include between 50% and 70% of ³⁹Ar. Integrated ages (2σ) are calculated using the total gas released for each Ar isotope. Inverse isochrons include the maximum number of steps with a probability of fit ≥ 0.05 (Jourdan & Renne 2007).

Table 4. Summary of ^{40}Ar - ^{39}Ar geochronological data for Ja'alan Granite sample JA15-03

JA15-03																			
Relative Abundances		36Ar [V]	% 1s	37Ar [V]	% 1s	38Ar [V]	% 1s	39Ar [V]	% 1s	40Ar [V]	% 1s	40(r)/39 (k)	$\pm 2s$	Age $\pm 2s$ (Ma)	40Ar (r) (%)	39Ar(k) (%)	K/Ca	$\pm 2s$	
5M38967D	60 °C 4	0.0000173	39.318	0.0000292	489.312	0.0000186	25.256	0.0008699	1.184	0.0527685	0.168	54.73523	± 4.84212	826.63 ± 58.69	90.23	12.05	12.8	± 125.4	
5M38968D	61 °C 4	0.0000168	43.191	0.0000181	663.176	0.0000264	16.411	0.0022223	0.720	0.1262498	0.190	54.54942	± 2.11717	824.37 ± 25.69	96.02	30.78	52.7	± 698.4	
5M38969D	61 °C 4	0.0000016	435.948	0.0000315	469.014	0.0000337	13.856	0.0027369	0.890	0.1519948	0.091	55.71253	± 1.83879	838.43 ± 22.14	100.32	37.91	37.4	± 350.8	
5M38974D	63 °C 4	0.0000058	123.568	0.0001871	66.156	0.0000075	56.729	0.0005081	1.337	0.0282885	0.246	52.24558	± 8.47821	796.20 ± 104.51	93.87	7.04	1.2	± 1.5	
5M38975D	67 °C 4	0.0000045	170.023	0.0000706	181.263	0.0000133	33.356	0.0008813	1.155	0.0502160	0.162	55.44972	± 5.33353	835.27 ± 64.34	97.32	12.21	5.4	± 19.5	
S		0.0000427	37.593	0.0001789	166.174	0.0000994	10.069	0.0072185	0.461	0.4095176	0.076								

Table 5. Summary of ^{40}Ar - ^{39}Ar geochronological data for Hassan Schist sample JA15-04

JA15-04																			
Relative Abundances		^{36}Ar [V]	% 1s	^{37}Ar [V]	% 1s	^{38}Ar [V]	% 1s	^{39}Ar [V]	% 1s	^{40}Ar [V]	% 1s	$^{40}(\text{r})/^{39}$ (k)	$\pm 2\text{s}$	Age $\pm 2\text{s}$ (Ma)	^{40}Ar (r) (%)	^{39}Ar (k) (%)	K/Ca	$\pm 2\text{s}$	
JA15-04																			
5M3895 1D	60 °C	4	0.0000 054	97.68 1	0.0000 742	154.28 4	0.0000 183	18.5 65	0.0018 316	0.81 3	0.1015 696	0.09 6	54.57517 \pm 1.92406	824. 69 \pm 23.35	98.42	16.86	10.6	\pm 32.7	
5M3895 2D	60 °C	4	0.0000 044	124.6 24	0.0000 090	1129.1 17	0.0000 878	4.65 5	0.0068 412	0.36 4	0.3757 115	0.10 3	55.10993 \pm 0.63401	831. 16 \pm 7.67	100.35	62.97	325. 6	\pm 7352. 7	
5M3895 3D	61 °C	4	0.0000 058	88.65 6	0.0000 746	158.58 3	0.0000 110	27.5 96	0.0004 504	1.91 6	0.0245 609	0.43 6	58.35593 \pm 7.19419	869. 99 \pm 85.14	107.03	4.15	2.6	\pm 8.2	
5M3895 5D	61 °C	4	0.0000 033	163.0 00	0.0001 368	91.241	0.0000 091	40.1 00	0.0007 134	1.25 2	0.0393 807	0.27 2	56.56043 \pm 4.74415	848. 62 \pm 56.81	102.48	6.57	2.2	\pm 4.1	
5M3895 6D	61 °C	4	0.0000 010	606.3 94	0.0000 866	124.51 0	0.0000 084	35.5 72	0.0007 438	1.29 4	0.0402 594	0.30 9	54.53469 \pm 5.00433	824. 19 \pm 60.74	100.75	6.85	3.7	\pm 9.2	
5M3895 8D	61 °C	4	0.0000 011	505.6 61	0.0000 316	329.37 9	0.0000 092	51.5 20	0.0002 831	1.81 1	0.0154 932	0.46 7	55.85214 \pm 11.5100 0	840. 12 \pm 138.4 8	102.06	2.61	3.9	\pm 25.4	
S			0.0000 102	130.4 71	0.0001 764	155.78 5	0.0001 437	6.30 0	0.0108 636	0.30 7	0.5969 753	0.07 5							

APPENDIX C: BULK ROCK AND MINERAL GEOCHEMISTRY

Preparation

SAWING

Samples undergoing geochemical analysis are first prepared by sawing before crushing. The sawing method is outlined in the geochronology preparation section in Appendix B.

CRUSHING

1. Make sure that the rocks are dry and clean. This entails ensuring that there is no lichen/soil or texta left on the rocks.
2. Any contaminants are to be cleaned off with a wire brush and compressed air.
3. Clean the jaw crusher before and after use.
 - a. Open crusher.
 - b. Spray from top to bottom with compressed air to remove dust and loose rock.
 - c. Scrub crusher with steel brush, paying particular attention to areas directly in contact with sample.
 - d. Spray from top to bottom with compressed air.
 - e. Clean crusher with ethanol and paper towels, once again paying attention to areas in direct contact.
 - f. Spray from top to bottom with compressed air.
 - g. Spray bottom tray with compressed air.
 - h. Clean tray with ethanol and paper towels.
 - i. Reassemble crusher.
4. Line the tray of the crusher with butcher paper to ensure that the samples are not contaminated.
5. Run sample through jaw crusher, collect crushed sample from butcher paper at bottom of crusher.
6. If samples are undergoing both geochemistry and mineral separation, the sample must be split after being run through the jaw crusher. This is done by portioning off half the sample with a ruler cleaned with paper towels and ethanol. The crusher distributes grain sizes evenly, keeping the sample representative.
7. After it has been through the jaw crusher, the sample is placed into the ring mill using the tungsten carbide rings. The ring mill is cleaned with compressed air and ethanol.
8. A quartz blank is first used to ensure contamination is kept at a minimum. The quartz is run for 1 minute.
9. The ring mill is again cleaned with compressed air and ethanol.
10. The samples are then placed into the tungsten carbide mill and run for 1 minute.
11. This fraction is then placed in a sample bag for later requirements.

FUSED XRF DISKS

Two samples were pre made into fused disks to be sent away for analysis via X-ray fluorescence, the following method was used:

1. All vials (including lids) and ceramic crucibles to be used in creation of the disks must first be thoroughly washed and dried.
 - a. Scrub vials/crucibles in warm soapy water, using a steel scourer for vials, and a soft cloth for crucibles.
 - b. Transfer vials/crucibles into cold water, making sure that any detergent is washed off.
 - c. Rinse the vials/crucibles thoroughly in RO water.
 - d. Dry the vials/crucibles overnight in an oven at 40°C
2. Loss on ignition needs to be calculated for each sample, this is done by first weighing 4g of each sample into a clean crucible, which are then weighed together.
3. The weighed samples are then transferred to a furnace and heated to 1100°C.
4. After ignition, the crucibles are then weighed again. The difference in weight between the ignited and unignited crucibles is used to calculate the LOI value of each sample.
5. To make the disks, the sample must be mixed with a lithium tetraborate flux.
 - a. Measure out one gram of ignited sample into a clean vial.
 - b. Measure out four grams of Lithium Tetraborate flux into the same vial.
 - c. Place the cap on the vial and shake thoroughly to mix the two components.
6. The disks are set in a Pt-Au crucible using the following procedure.
 - a. The sample/flux mixture is transferred to a Pt-Au crucible.
 - b. This crucible is placed on a propane burner and left for two minutes.
 - c. After two minutes have elapsed a small spatula worth of Ammonium Nitrate is added to the sample.
 - d. After adding the Ammonium Nitrate, the sample must be stirred occasionally by swirling the crucible with tongs.
 - e. After six minutes have elapsed since adding the ammonium nitrate, the sample is poured from the crucible to a disk mould which has been preheated on a second propane burner.
 - f. Once the sample is transferred to the mould, the burner is turned off and compressed air is blown onto the bottom of the mould for two minutes.
 - g. When two minutes have elapsed, the mould is transferred to a cooling brick, once cool to touch, the fused disk may be removed from the mould.

STANDARDS

Samples sent away for geochemical analysis have had standards included with the unknowns to verify data quality.

DUPLICATE SAMPLES

Samples sent away have had duplicates of unknown samples included to verify data quality.

MAJOR ELEMENT GEOCHEMISTRY

Whole-rock geochemical analyses for phase equilibria modelling of two samples were undertaken using XRF analysis at Bureau Veritas Minerals, Perth, Western Australia. Major elements were analysed on fused beads using a lithium tetraborate flux, as described by (Kil & Jung 2015). Iron content was determined by wet chemistry methods. Two additional samples were made into fused XRF disks and also sent away for whole-rock geochemical analysis. These samples were analysed via XRF analysis at a CSIRO laboratory, University of Adelaide (Waite campus), South Australia.

Table 6. Whole rock geochemistry for samples used in calculation of phase diagrams.

	JA15-36	JA15-04
LOI	2.36	4.73
Total	97.64	97.22
SiO ₂	76.994	60.53
TiO ₂	0.251	0.91
Al ₂ O ₃	10.745	16.79
Fe ₂ O ₃	2.938	-
Fe	-	6.33
MnO	0.064	0.08
MgO	1.798	1.62
CaO	0.163	1.95
Na ₂ O	0.727	0.817
K ₂ O	3.932	3.46
P ₂ O ₅	0.022	-
SO ₃	0.006	-
Cl	<10	-

MINERAL CHEMISTRY

A CAMECA SX 5 was used for microprobe analysis of mineral chemistry using the method from Adelaide Microscopy (outlined below). Calibration was done on natural and synthetic mineral standards following the standard protocols at Adelaide Microscopy.

Sample loading

1. To place a sample into the microprobe: Sample exchange-Transfer sample into microprobe. Follow the prompts. Next, turn the extraction handle on the airlock to the extract symbol.

2. Open the airlock (push airlock handle in and swing up). Note that handle locks and rotates slightly. Push extraction handle in all the way, then pull out to remove sample block. Close the airlock (rotate handle and swing down). Note that handle locks and moves out slightly.
3. Follow the prompts on the screen.
4. After a minute or so, the airlock is vented. Open the airlock door by depressing the latch button and remove the sample cassette by pushing the sample block onto the extraction handle until it clicks and releases the sample block.
5. Change the samples as needed on the sample preparation pad.
6. Place the sample on the sample preparation pad and change samples and standard mounts as necessary. Be sure to document sample placement and identification by filling out the sample mount map in one of the 3 ring binders. Be sure to orient the sample block correctly. The small hole goes to the front of the sample mount. See the sample location chart for the correct orientation.
7. Place the prepared sample block back in the airlock: When ready, open the airlock door (depress the spring latch) and turn the extraction handle to the insert symbol. Then slide the sample block onto the extraction handle rails until it clicks.
8. Close the airlock door. During this time, the system may request that the gun valve be turned to position 2. If this is requested, turn the gun valve to position 2 and wait for the Vacuum ready message, if not, then the arlk command can be given immediately. When ready, pump out the airlock: Now open the airlock (push airlock handle in and swing up). Note that handle locks and rotates slightly. Push extraction handle in all the way, then pull the empty extraction handle back out all the way. Close the airlock (rotate handle and swing down). Note that handle locks and moves out slightly. Wait until the system is ready as seen on the screen.
9. Turn the beam on via the beam and set up tab. Ensuring that the scanning is 'on' focus the beam on both the back scattered image and the reflected light
10. To navigate use the joystick to move around the slide. To check the composition of the mineral, turn the scanning to 'off'. Click on the EES screen and hit 'Acquire'. Drag the line to the peaks to determine what the mineral is composed of.
11. Imaging is done via the SEM tab with a frame time of 15.32. Tick the box and press save and display. Once this is done, un-tick the box and return to 0.32 for the frame time.
12. To store points, ensure that the reflected image is focused. Move the white cross to desired position. On the left hand screen where the software is displayed, click 'digitize'. Type in the name of the file. Finally, click add new unknown. Adding a single point is done by clicking 'single point'
13. Once all points have been selected, select all. Click sample set up, then yes. Finally, to start the acquisition, press the button 'run samples'.

Table 7. Mineral chemistry data for samples from Jebel Ja'alan.

Mineral	mu	mu	mu	mu	mu	ksp	ksp	ksp	ksp
	JA15-36	JA15-36	JA15-36	JA15-36	JA15-36	JA15-36	JA15-36	JA15-36	JA15-36
	Area1	Area1	Area1	Area1	Area1	Area 2	Area 2	Area 2	Area 2
Analysis	Muscovite	Muscovite	Muscovite	Muscovite	Muscovite	Kfeldspar	Kfeldspar	Kfeldspar	Kfeldspar
SiO2	45.8277	45.4842	46.1179	46.8683	47.4913	63.6086	63.752	65.139	63.8942
TiO2	0.235187	0.109961	0.021932	0.000412	0	0.004378	0.006784	0.002592	0.005758
Al2O3	35.9181	35.1512	36.0037	31.9662	33.2307	18.6576	18.6456	19.65	18.7884
Cr2O3	0	0.002873	0.005985	0	0.006337	0.008383	0.006765	0	0
FeO	2.63547	2.55701	2.50552	2.57812	2.90772	0	0	0.025426	0
MnO	0	0.014899	0.012132	0.027078	0.041991	0.00044	0.007828	0.022909	0
MgO	1.03987	1.15267	1.06099	4.44906	3.83242	0	0.008749	0.050597	0
ZnO	0.001233	0.020622	0.002434	0.001382	0.032564	0.026556	0	0.07668	0
CaO	0.027331	0.017532	0.004516	0.030818	0.093734	0.038313	0.01453	0.098694	0.018886
Na2O	0.654366	0.5831	0.67527	0.161036	0.226926	1.46086	1.22507	1.80777	1.68526
K2O	8.74799	8.82654	8.45882	7.98765	7.45351	14.8541	15.152	13.0437	14.7512
Cl	0.040364	0.01577	0.028768	0.009806	0.013882	0.017038	0.012396	0.036854	0.012088
F	0	0.024832	0.008138	0.213417	0.167667	0	0	0	0
Total	95.12	93.95	94.90	94.20	95.43	98.67	98.83	99.95	99.15
Compositional Variables									
y(bi)	-	-	-	-	-	-	-	-	-
ca(pl, ksp)	--	--	--	--	--	0.001881	0.000717	0.005222	0.000915
k(pl)	--	--	--	--	--	--	--	--	--
na(ksp)	--	--	--	--	--	0.129791	0.109356	0.173082	0.147811
x(mu)	0.587039	0.554416	0.569807	0.245296	0.29852	--	--	--	--
y(mu)	0.750482	0.738546	0.755115	0.411386	0.460522	--	--	--	--
x(gt)	--	--	--	--	--	--	--	--	--

bi JA15-36 Area 3 Biotite	bi JA15-36 Area 3 Biotite	bi JA15-36 Area 3 Biotite	sil JA15-36 Area 3 Sillimanite	sil JA15-36 Area 3 Sillimanite	mu JA15-36 Area 3 Muscovite	ksp JA15-36 Area 3 Kfeldspar	ksp JA15-36 Area 3 Kfeldspar	ksp JA15-36 Area 3 Kfeldspar	bi JA15-36 Area 4 Biotite	bi JA15-36 Area 4 Biotite
39.0866	36.995	36.1115	49.8129	47.5507	63.6665	63.7978	63.1058	63.4142	35.3898	36.1021
1.28846	1.81683	1.70532	0.111496	0.08532	0.000182	0.002893	0	0.002502	1.59838	1.63864
26.6284	20.3212	19.9855	35.2436	37.7361	18.8889	18.662	18.6481	18.4461	19.3685	19.6444
0	0.006594	0.013324	0	0	0.008774	0.004101	0	0.014414	0.00521	0
10.2407	12.792	13.0126	1.16577	0.735628	0.166362	0	0	0.017883	13.5255	13.1214
0.311096	0.420882	0.452178	0	0	0	0	0	0	0.413622	0.422485
9.52139	13.8395	13.1238	1.73717	0.80193	0.021096	0.00354	0.006734	0.004978	13.48	13.4621
0.133774	0.262436	0.231196	0.018179	0	0	0.046911	0	0.028168	0.253049	0.162073
0.005005	0.032629	0	0.070174	0.045673	0.001061	0.002655	0.020374	0.013357	0.014	0.000271
0.168295	0.209617	0.193038	0.077373	0.033535	0.656131	1.45066	1.17256	1.11741	0.23619	0.225278
6.5673	9.55637	9.51348	1.34665	0.956669	15.4406	14.997	15.1893	15.3601	9.11099	9.17548
0.016781	0.021718	0.018339	0.008786	0.011457	0	0.011953	0.000929	0.003673	0.032054	0.024732
0.43361	0.487126	0.514158	0.191824	0	0	0	0	0	0.463603	0.420292
94.22	96.55	94.65	89.70	87.95	98.85	98.98	98.14	98.42	93.69	94.22
0.98936	0.420445	0.428043	-	-	-	-	-	-	0.380495	0.413764
--	--	--	--	--	--	0.00013	0.001007	0.000657	--	--
--	--	--	--	--	--	--	--	--	--	--
--	--	--	--	--	--	0.128155	0.104901	0.099492	--	--
--	--	--	--	--	0.815606	--	--	--	--	--
--	--	--	--	--	0.989053	--	--	--	--	--
--	--	--	--	--	--	--	--	--	--	--

bi JA15-36 Area 4 Biotite	bi JA15-36 Area 4 Biotite	bi JA15-36 Area 4 Biotite	sil JA15-36 Area 4 Sillimanite	sil JA15-36 Area 4 Sillimanite	sil JA15-36 Area 4 Sillimanite	sil JA15-36 Area 5 Sillimanite	sil JA15-36 Area 5 Sillimanite	sil JA15-36 Area 5 Sillimanite	sil JA15-36 Area 5 Sillimanite	bi JA15-36 Area 5 Biotite
41.5534	36.1331	36.6684	47.5508	46.9763	46.2073	45.771	45.2576	46.0347	47.021	35.878
1.43736	1.53448	1.59526	0.02503	0.021906	0.014369	0.019819	0.007642	0	0	1.6398
17.3456	19.9011	20.3287	38.6326	38.6268	38.3755	37.8311	37.6441	37.8824	38.162	19.248
0.016611	0.00744	0.013993	0	0	0	0	0.002516	0.000382	0	0
12.3301	12.969	12.9622	0.313579	0.317264	0.208882	0.172778	0.149503	0.297736	0.273103	12.935
0.387255	0.381619	0.407808	0	0	0	0	0	0	0	0.466394
11.9367	13.6082	13.705	0.345392	0.278259	0.147098	0.419155	0.146661	0.241525	0.170494	13.4204
0.147749	0.212877	0.189985	0	0	0	0	0	0	0	0.158734
0.081723	0	0.027992	0.026498	0	0.040021	0.037681	0.01896	0.679517	0.067075	0.019777
0.303532	0.196672	0.222907	0.039151	0.03546	0.052898	0.017386	0.024036	0.03676	0.052213	0.203632
8.49965	9.61743	9.52561	0.128421	0.141202	0.05231	0.213412	0.093087	0.114634	0.073496	9.14263
0.034413	0.015775	0.032416	0.008217	0.008201	0.016717	0.001213	0.001286	0.022535	0.009188	0.022887
0.378683	0.465089	0.467435	0.00929	0	0	0	0	0.002835	0	0.446665
94.29	94.84	95.94	87.07	86.40	85.11	84.48	83.35	85.31	85.83	93.39
0.518457	0.415338	0.430144	-	-	-	-	-	-	-	0.401359
--	--	--	--	--	--	--	--	--	--	--
--	--	--	--	--	--	--	--	--	--	--
--	--	--	--	--	--	--	--	--	--	--
--	--	--	--	--	--	--	--	--	--	--
--	--	--	--	--	--	--	--	--	--	--
--	--	--	--	--	--	--	--	--	--	--

bi	ksp	ksp	ksp	mu	mu	mu	mu	gt	gt	gt
JA15-36	JA15-36	JA15-36	JA15-36	JA15-36	JA15-36	JA15-36	JA15-36	JA15-43	JA15-43	JA15-43
Area 5	Area 6	Area 6	Area 6	Area 6	Area 6	Area 7	Area 7	Area 1	Area 1	Area 1
Biotite	Kfeldspar	Kfeldspar	Kfeldspar	Muscovite	Muscovite	Muscovite	Muscovite	Garnet	Garnet	Garnet
								traverse	traverse	traverse
36.5399	63.8329	63.4307	63.5318	51.2205	45.3865	64.1274	63.754	36.8581	36.2142	36.4717
1.57475	0	0	0.005703	0.764474	0.348608	0.012159	0.007832	0.00207	0	0.023338
19.906	18.6925	18.8081	18.5623	33.9647	34.8805	18.8614	18.8016	20.9539	20.5831	20.6163
0.007471	0	0	0.009267	0.014554	0	0.004616	0.009629	0.01605	0.030854	0.037014
13.0127	0	0	0.020007	2.06894	3.03557	0	0.020552	29.6723	30.1153	30.151
0.378473	0	0	0	0.004925	0	0	0	9.46169	8.65913	8.34571
13.7728	0.006113	0	0	0.832536	0.961735	0.001499	0	2.16123	2.35804	2.40836
0.219725	0	0.008101	0.00322	0	0	0.020715	0	0	0.005192	0.017191
0	0.033424	0.001121	0	0.001071	0	0.025711	0.013204	0.824056	0.797329	0.782824
0.235487	1.85918	0.689667	1.49886	0.459076	0.53284	1.45305	1.77493	0.00112	0.009044	0.004212
9.45344	14.2512	15.5135	14.8688	9.29711	8.27698	14.4231	14.4533	0	0.000362	0
0.016707	0.001417	0.021279	0.001478	0.011619	0.007793	0.003052	0	0	0	0.008967
0.441455	0	0	0	0.009728	0	0	0	0.033398	0.045873	0.028982
95.37	98.68	98.47	98.50	98.64	93.43	98.93	98.84	99.97	98.80	98.88
0.41428	-	-	-	-	-	-	-	-	-	-
--	0.001641	5.68E-05	0	--	--	--	--	--	--	--
--	--	--	--	--	--	--	--	--	--	--
--	0.165196	0.063286	0.132855	--	--	--	--	--	--	--
--	--	--	--	0.582267	0.639037	0	1	--	--	--
--	--	--	--	0.810844	0.731504	0.998881	0.998899	--	--	--
--	--	--	--	--	--	--	--	0.885066	0.875037	0.874725

gt JA15-43 Area 1 Garnet traverse	gt JA15-43 Area 1 Garnet traverse	gt JA15-43 Area 1 Garnet traverse	gt JA15-43 Area 1 Garnet traverse	gt JA15-43 Area 1 Garnet traverse	gt JA15-43 Area 1 Garnet traverse	gt JA15-43 Area 1 Garnet traverse	gt JA15-43 Area 1 Garnet traverse	gt JA15-43 Area 1 Garnet traverse	gt JA15-43 Area 1 Garnet traverse	gt JA15-43 Area 1 Garnet traverse	gt JA15-43 Area 1 Garnet traverse
35.746	36.0838	36.4492	36.4891	37.3736	35.8209	36.2985	36.2121	36.3421	36.5266	36.6046	
0.010686	0	0	0.010767	0.01228	0.009179	0.001945	0.000362	0.007256	0.016535	0.000748	
20.2737	20.4859	20.9152	20.7342	21.7252	20.3876	20.7314	20.5044	20.5773	20.5982	20.8076	
0.013757	0.00899	0.027576	0.039151	0.00828	0.021163	0.009985	0.008102	0.026119	0.006602	0.038743	
29.9315	30.5147	30.5375	30.4766	30.2289	30.5784	30.8305	30.0432	30.3746	30.3058	30.122	
8.00626	8.08174	8.29498	8.17961	8.05419	8.20001	8.25208	8.23834	8.44551	8.57882	9.00029	
2.35857	2.42643	2.48248	2.43038	2.50733	2.32836	2.41422	2.36234	2.36763	2.36027	2.27563	
0	0	0.009828	0.002316	0	0.024294	0	0	0	0.062243	0	
0.759256	0.790081	0.774764	0.78996	0.77291	0.807228	0.76832	0.762433	0.764417	0.795637	0.840049	
0.024797	0.012993	0	0.019878	0.051327	0.032634	0.030718	0.016952	0	0.023728	0.005921	
0.000215	0.006161	0	0.004116	0.018804	0.007849	0.001501	0.000021	0.000313	0.005863	0.005805	
0.00092	0	0	0.003605	0.013343	0.003823	0	0.002719	0	0	0	
0.016902	0.039487	0.016643	0.044037	0.070525	0.082464	0.087816	0.054733	0.030707	0	0.050898	
97.14	98.43	99.50	99.20	100.80	98.27	99.39	98.18	98.92	99.28	99.73	
-	-	-	-	-	-	-	-	-	-	-	
--	--	--	--	--	--	--	--	--	--	--	
--	--	--	--	--	--	--	--	--	--	--	
--	--	--	--	--	--	--	--	--	--	--	
--	--	--	--	--	--	--	--	--	--	--	
0.87495	0.872859	0.870775	0.874103	0.871171	0.876564	0.874343	0.876559	0.87603	0.875523	0.879722	

gt JA15-43 Area 1 Garnet traverse	mu JA15-43 Area 2 Muscovite	mu JA15-43 Area 2 Muscovite	mu JA15-43 Area 2 Muscovite	mu JA15-43 Area 2 Muscovite	bi JA15-43 Area 2 Biotite	bi JA15-43 Area 2 Biotite	bi JA15-43 Area 2 Biotite	bi JA15-43 Area 2 Biotite	pl JA15-43 Area 3 Plag traverse	pl JA15-43 Area 3 Plag traverse
36.4128	47.7697	46.9922	46.8127	48.0109	33.4392	34.7782	35.9968	33.4918	64.1277	63.4194
0.009393	0.233443	0.232242	0.069574	0.162081	2.6192	2.61852	2.27468	2.82671	0	0.007628
20.6263	37.2876	36.345	37.6001	35.8094	19.828	20.7432	24.1027	18.2635	21.0048	22.6427
0.023539	0.034183	0	0.039861	0.028459	0.050226	0.030128	0.026481	0.045878	0.014473	0.000532
29.8058	1.35673	1.27406	1.08262	1.74824	19.8795	19.2676	17.8536	22.1207	0.00087	0
9.32993	0	0.011986	0.012156	0.009164	0.207546	0.128737	0.171321	0.192283	0	0.017817
2.07323	0.690172	0.913138	0.644617	1.14169	6.42063	6.69245	5.87039	7.53049	0	0.00167
0.023051	0.008637	0	0	0	0.031817	0	0.069859	0	0.097845	0.022646
0.845711	0.009603	0.043141	0.024684	0.040495	0.068962	0.068375	0.049663	0.005713	2.02568	3.19236
0.014783	0.387702	0.326642	0.442842	0.303377	0.136516	0.126695	0.111499	0.150725	10.835	10.0935
0.001826	8.00553	7.76122	8.186	7.95312	6.98149	7.13628	5.25349	8.76525	0.214306	0.134884
0	0	0.01386	0.011614	0.026048	0.041	0.034932	0.026602	0.038868	0.018951	0.000039
0.083318	0	0.042525	0.005689	0.016699	0.197427	0.19122	0.166444	0.2878	0	0
99.21	95.78	93.93	94.93	95.24	89.81	91.73	91.90	93.59	98.34	99.53
-	-	-	-	-	0.550182	0.604744	0.861211	0.33215	-	-
--	--	--	--	--	--	--	--	--	0.092547	0.147669
--	--	--	--	--	--	--	--	--	0.011658	0.007429
--	--	--	--	--	--	--	--	--	--	--
--	0.524396	0.439017	0.485068	0.462041	--	--	--	--	--	--
--	0.859195	0.838923	0.876995	0.792617	--	--	--	--	--	--
0.888806	--	--	--	--	--	--	--	--	--	--

pl JA15-43 Area 3 Plag traverse	pl JA15-43 Area 3 Plag traverse	pl JA15-43 Area 3 Plag traverse	pl JA15-43 Area 3 Plag traverse	pl JA15-43 Area 3 Plag traverse	pl JA15-43 Area 3 Plag traverse	pl JA15-43 Area 3 Plag traverse	pl JA15-43 Area 3 Plag traverse	pl JA15-43 Area 3 Plag traverse	pl JA15-43 Area 3 Plag traverse	pl JA15-43 Area 3 Plag traverse	pl JA15-43 Area 3 Plag traverse
62.1339	62.0866	62.1456	68.0832	62.3543	62.8565	62.2967	54.7725	64.56	67.552	63.5012	
0.002971	0.001599	0.004789	0.001616	0.013129	0.004794	0	0.100582	0.011526	0	0.010806	
23.4076	23.322	23.511	23.368	26.5122	25.6405	23.3678	30.1874	24.6135	22.96	23.6078	
0.019778	0.016863	0.011802	0	0.011688	0.015356	0.021964	0.004668	0.007237	0.00845	0.012346	
0.022537	0	0	0.041967	0.237656	0.251466	0.001396	0.340439	0.081248	0.025283	0.194108	
0	0.008147	0	0.010167	0.005003	0	0.030982	0.226423	0	0.005927	0.015516	
0	0	0.013137	0.039234	0.199179	0.150415	0	0.117245	0.120989	0.016611	0.192639	
0.043247	0	0.002267	0	0	0	0.059106	0	0.010858	0	0.0116	
4.03792	4.19346	4.08359	1.30522	0.437418	1.94487	4.13024	0.728065	2.04679	0.68571	1.53038	
9.76398	9.5244	9.48021	11.3702	8.20883	9.06184	9.4976	4.76253	9.65829	11.0588	9.34705	
0.215424	0.29374	0.281362	0.476371	3.17888	2.25237	0.248884	5.63554	1.08246	0.758916	1.388	
0.003999	0	0.001659	0.01678	0.007718	0.005279	0.00526	0.016773	0.011717	0.012188	0.000979	
0	0	0	0	0	0.000779	0	0	0	0	0.001162	
99.65	99.45	99.54	104.71	101.16	102.18	99.66	96.89	102.20	103.08	99.81	
-	-	-	-	-	-	-	-	-	-	-	
0.183847	0.192549	0.189282	0.058144	0.022929	0.092502	0.191095	0.045344	0.09834	0.031744	0.076147	
0.011678	0.016059	0.015528	0.025267	0.198402	0.127552	0.013711	0.417902	0.061923	0.041831	0.08223	
--	--	--	--	--	--	--	--	--	--	--	
--	--	--	--	--	--	--	--	--	--	--	
--	--	--	--	--	--	--	--	--	--	--	
--	--	--	--	--	--	--	--	--	--	--	

pl JA15-43 Area 3 Plag traverse	pl JA15-43 Area 3 Plag traverse	pl JA15-43 Area 3 Plag traverse	pl JA15-43 Area 3 Plag traverse	pl JA15-43 Area 3 Plag traverse	pl JA15-43 Area 3 Plag traverse	mu JA15-43 Area 3 Muscovite	mu JA15-43 Area 3 Muscovite	mu JA15-43 Area 4 Muscovite	mu JA15-43 Area 4 Muscovite	mu JA15-43 Area 4 Muscovite
63.0258	62.5866	63.6309	66.0313	64.6947	65.4442	46.3257	66.9517	45.589	45.6938	46.9605
0.009984	0.005353	0.003874	0.003161	0.000835	0	0.009086	0.002092	0.947449	0.187529	0.386305
25.4323	24.0558	24.4247	23.7765	25.2488	23.2489	35.9956	23.605	37.1302	36.9965	38.727
0.005491	0.006791	0.003093	0	0	0.005296	0	0.019304	0.059555	0.025895	0.028825
0.120307	0.099457	0.057109	0.064168	0.037383	0.126766	1.66301	0.442616	1.22813	1.19448	1.00111
0	0	0.010026	0	0.004555	0	0.030287	0.020297	0	0	0
0.072515	0.034203	0.031046	0.218065	0.062932	0.077246	0.97537	0.099916	0.504597	0.519018	0.34201
0	0.048441	0.006018	0	0.003343	0	0.009134	0	0.015771	0.0109	0
1.42419	3.01935	2.34661	0.981229	1.21214	0.447646	0.02955	0.398945	0.090657	0.025553	0.029765
8.98105	9.41854	9.71933	10.0551	9.23602	9.82257	0.455896	0.387884	0.455928	0.39821	0.564625
2.17779	0.498233	1.1239	1.37663	1.93393	1.39453	7.7319	5.90264	8.21495	8.46369	8.3691
0.01202	0.002723	0.013022	0.02219	0.001435	0.019009	0.0109	0.00332	0	0.010877	0.00366
0	0	0	0	0	0	0.038086	0	0	0.001532	0
101.26	99.77	101.37	102.52	102.44	100.58	93.26	97.83	94.24	93.52	96.41
-	-	-	-	-	-	-	-	-	-	-
0.070263	0.146169	0.110309	0.047138	0.059923	0.022514	--	--	--	--	--
0.127927	0.028719	0.062905	0.078741	0.113832	0.083508	--	--	--	--	--
--	--	--	--	--	--	--	--	--	--	--
--	--	--	--	--	--	0.488836	0.71303	0.577192	0.56348	0.621471
--	--	--	--	--	--	0.807784	0.967367	0.881243	0.881079	0.912977
--	--	--	--	--	--	--	--	--	--	--

mu JA15-43 Area 4 Muscovite	bi JA15-43 Area 4 Biotite	bi JA15-43 Area 4 Biotite	bi JA15-43 Area 4 Biotite	bi JA15-43 Area 4 Biotite	bi JA15-43 Area 4 Biotite	bi JA15-43 Area 4 Biotite
46.4136	25.0309	24.2593	24.4525	24.9249	26.7171	32.7952
1.27531	2.7735	0.211559	0.216076	1.03072	0.486164	1.75786
37.0829	22.1985	22.1322	22.0586	22.4515	21.4027	19.4081
0.023219	0.05104	0.015981	0.028509	0.01462	0.029617	0.049312
1.00731	24.0126	27.8961	27.7911	27.422	26.6368	21.6326
0	0.263721	0.364689	0.386588	0.306025	0.306417	0.191873
0.570536	9.37005	11.615	11.0066	11.4497	11.2557	8.99584
0	0.022533	0.054958	0.013811	0.020097	0	0.026056
0	0.050941	0.001752	0.007531	0.009272	0.061609	0.168224
0.588188	0.023322	0.034958	0.011753	0.003538	0.060732	0.07658
7.59806	0.059672	0.102388	0.028107	0.046554	0.784228	5.09327
0	0.01709	0.017679	0.011405	0.012541	0.009257	0.051442
0	0.072188	0.041785	0.053348	0.065083	0.121309	0.187241
94.56	83.91	86.73	86.04	87.73	87.82	90.34
-	0.396974	0.287628	0.322783	0.2971	0.322684	0.433225
--	--	--	--	--	--	--
--	--	--	--	--	--	--
--	--	--	--	--	--	--
0.497558	--	--	--	--	--	--
0.888784	--	--	--	--	--	--
--	--	--	--	--	--	--

mu JA15-04 Area 1 Muscovite	mu JA15-04 Area 1 Muscovite	mu JA15-04 Area 1 Muscovite	mu JA15-04 Area 1 Muscovite	mu JA15-04 Area 1 Muscovite	bi JA15-04 Area 1 Biotite	bi JA15-04 Area 1 Biotite	bi JA15-04 Area 1 Biotite
46.7625	46.5749	46.2321	47.5583	55.5953	33.3892	33.8192	34.0545
0.210291	0.661557	0.622797	0.266358	0.016417	2.43173	2.52926	2.53894
38.2884	37.5351	37.7691	38.0804	25.5903	18.9203	19.0755	19.0691
0	0.020453	0.016636	0.035891	0.003135	0.031653	0.022019	0.007474
0.853261	0.929975	0.93769	0.897884	0.095836	21.7897	22.0532	21.9806
0	0	0	0	0.008768	0.20118	0.19065	0.228012
0.332769	0.501645	0.555696	0.556887	0.055359	6.96526	7.03378	7.22743
0	0	0	0	0.059046	0.0221	0.046208	0.068479
0.021918	0	0.008926	0.007352	4.44781	0.028739	0.06074	0.010576
0.927633	0.990993	0.9228	1.0792	8.0922	0.314137	0.39431	0.358841
8.26836	8.21022	7.53519	7.62876	0.190735	8.90834	8.76984	9.24242
0.019101	0	0.019987	0.030345	0.040813	0.035457	0.044771	0.017403
0	0	0	0.002334	0	0.299163	0.27691	0.260786
95.68	95.42	94.62	96.14	94.19	93.20	94.19	94.95
-	-	-	-	-	0.399552	0.397522	0.387359
--	--	--	--	--	--	--	--
--	--	--	--	--	--	--	--
--	--	--	--	--	--	--	--
0.58986	0.509758	0.486246	0.474884	0.492643	--	--	--
0.921245	0.900262	0.89412	0.897943	0.986127	--	--	--
--	--	--	--	--	--	--	--

bi	bi	sil	sil	sil	mu	mu	mu	mu	mu	sil
JA15-04	JA15-04	JA15-04	JA15-04	JA15-04	JA15-04	JA15-04	JA15-04	JA15-04	JA15-04	JA15-04
Area 1	Area 1	Area 1	Area 1	Area 1	Area 2	Area 2	Area 2	Area 2	Area 2	Area 2
Biotite	Biotite	Sillimanite	Sillimanite	Sillimanite	Muscovite	Muscovite	Muscovite	Muscovite	Muscovite	Sillimanite
33.9383	34.0476	29.9617	30.4764	27.1539	46.749	45.736	39.4298	46.0554	46.1961	45.3993
2.53701	2.54321	0.054394	0.129043	0.236703	0.191814	0.192059	0.103896	0.125111	0.092514	0
19.1396	19.2066	26.4254	26.6214	25.52	37.8031	38.7965	43.4295	38.2133	38.4621	39.0976
0.026367	0.049468	0	0.000456	0.01754	0.035551	0.009477	0.050456	0	0.035212	0.035108
21.4804	21.5053	12.8639	2.51756	24.0709	0.903207	0.749915	0.813741	0.78473	0.820448	0.170473
0.176637	0.156409	0.119231	0	0.301629	0	0	0.025539	0	0	0
7.13531	7.1144	5.00672	1.12522	9.09113	0.44199	0.390422	0.460336	0.310313	0.298196	0.351561
0.063173	0	0	0	0.0068	0	0.003714	0	0	0	0
0.003913	0.011646	0.068058	0.989494	0.012547	0.008806	0.054143	0.129733	0.015176	0.013357	0.111298
0.315902	0.287032	0.087273	0.060592	0.059111	0.862936	1.0234	0.952002	0.926687	0.957144	0.098045
9.04562	8.94906	0.061766	0.059374	0.037338	7.99489	8.01883	7.33487	7.99096	8.42323	0.24148
0.027315	0.024677	0.315616	0.373292	0.042607	0.005464	0.042617	0.038063	0.02385	0.016323	0.115288
0.26864	0.236295	0	0	0.02712	0.012363	0	0	0	0	0.049174
94.04	94.03	74.89	62.27	86.56	95.00	95.01	92.76	94.44	95.31	85.62
0.411081	0.420603	-	-	-	-	-	-	-	-	-
--	--	--	--	--	--	--	--	--	--	--
--	--	--	--	--	--	--	--	--	--	--
--	--	--	--	--	--	--	--	--	--	--
--	--	--	--	--	0.534056	0.518617	0.497864	0.586503	0.606798	--
--	--	--	--	--	0.907426	0.920542	0.906313	0.926307	0.925983	--
--	--	--	--	--	--	--	--	--	--	--

bi	bi	bi	bi	bi	sil	sil	sil	gt JA15-41 Area 1 Garnet Traverse	gt JA15-41 Area 1 Garnet Traverse	gt JA15-41 Area 1 Garnet Traverse
JA15-04 Area 2 Biotite	JA15-04 Area 2 Biotite	JA15-04 Area 2 Biotite	JA15-04 Area 2 Biotite	JA15-04 Area 2 Biotite	JA15-04 Area 3 Sillimanite	JA15-04 Area 3 Sillimanite	JA15-04 Area 3 Sillimanite			
32.7701	34.0752	33.8517	33.5337	33.8977	44.7189	38.3049	44.5323	35.3024	36.4846	36.4178
2.73116	2.6524	2.50912	2.40095	2.59514	0.027019	0.065833	0.062727	0.016101	0.014345	0.011702
18.4	19.0801	19.1341	19.0275	19.195	38.3578	33.0698	36.4575	20.5053	20.7654	21.0181
0.080258	0.010493	0.033245	0.026891	0.027241	0.009152	0.00742	0.038435	0	0	0.005585
21.502	21.5755	21.7736	21.8634	21.7256	2.31762	5.91443	0.455584	33.5394	33.5027	33.9965
0.162907	0.136267	0.177208	0.190694	0.179432	0	0.073263	0.022034	5.22114	4.95735	4.82391
6.71833	7.11457	7.09131	6.95508	7.12837	0.391581	2.48341	0.366296	2.42076	2.51727	2.57097
0	0.054952	0.016696	0.031647	0.040649	0	0	0.03676	0	0	0.038373
0.029497	0.026689	0.018229	0.047353	0.006244	0.107135	0.114478	0.085369	0.83905	0.858641	0.88168
0.423863	0.361786	0.364661	0.364321	0.302663	0.155196	0.132877	0.081012	0.153737	0.072211	0.016062
9.06652	9.09757	9.23273	8.98662	9.28552	0.096638	0.072657	0.079935	0.030472	0.013607	0
0.046388	0.044952	0.046123	0.07871	0.012182	0.063179	0.053397	0.068397	0.073037	0.022517	0.003488
0.327917	0.258739	0.293067	0.269479	0.219056	0	0	0.020462	0.028223	0.03599	0.04021
92.11	94.37	94.41	93.65	94.52	86.23	80.28	82.28	98.10	99.22	99.81
0.366313	0.402762	0.398645	0.402628	0.402475	-	-	-	-	-	-
--	--	--	--	--	--	--	--	--	--	--
--	--	--	--	--	--	--	--	--	--	--
--	--	--	--	--	--	--	--	--	--	--
--	--	--	--	--	--	--	--	--	--	--
--	--	--	--	--	--	--	--	--	--	--
--	--	--	--	--	--	--	--	0.8778	0.879773	0.878086

gt JA15-41 Area 1 Garnet Traverse	gt JA15-41 Area 1 Garnet Traverse	gt JA15-41 Area 1 Garnet Traverse	gt JA15-41 Area 1 Garnet Traverse	gt JA15-41 Area 1 Garnet Traverse	gt JA15-41 Area 1 Garnet Traverse	gt JA15-41 Area 1 Garnet Traverse	gt JA15-41 Area 1 Garnet Traverse	gt JA15-41 Area 1 Garnet Traverse	gt JA15-41 Area 1 Garnet Traverse	gt JA15-41 Area 1 Garnet Traverse	gt JA15-41 Area 1 Garnet Traverse
36.3079	31.9538	36.4612	36.368	36.2657	36.4852	27.3233	26.7318	33.3901	36.4813	36.4857	
0.035302	0.021349	0.020574	0.027824	0.016343	0.015453	0.066662	0	0.182933	0.032493	0.006334	
20.8283	21.8515	20.672	20.7247	20.5981	20.7458	34.6365	18.4482	21.959	20.7965	20.813	
0.012773	0	0.016307	0.017254	0.016	0.009121	0.014934	0	0	0	0.022985	
33.6949	30.3072	33.7699	33.9181	34.0697	34.2909	24.966	29.2871	32.9233	34.2547	33.8628	
4.76738	3.40493	4.66812	4.5658	4.50572	4.36703	3.05748	2.94251	3.8832	4.46746	4.9547	
2.58085	2.30119	2.56224	2.49207	2.6497	2.61404	1.92986	2.20462	2.56643	2.63596	2.58772	
0.043295	0.003203	0	0.002848	0.023809	0	0	0	0	0	0	
0.888776	0.79756	0.931109	0.901236	0.817751	0.822242	0.80325	0.704038	0.914912	0.873989	0.815214	
0.006155	0.252672	0.013191	0.010091	0.019166	0.016128	0.27479	0.368417	0.578589	0	0.022107	
0	0.105475	0.000843	0	0	0.003699	0.186874	0.093137	0.063696	0.003681	0.00538	
0	0.070197	0.004019	0	0.008453	0.006229	0.091082	0.217595	0.324619	0.000349	0.004848	
0.077224	0	0.047896	0.033691	0.015485	0.052498	0	0.02652	0.076794	0.022765	0.031309	
99.21	91.05	99.15	99.05	99.00	99.40	93.33	80.96	96.76	99.56	99.60	
-	-	-	-	-	-	-	-	-	-	-	
--	--	--	--	--	--	--	--	--	--	--	
--	--	--	--	--	--	--	--	--	--	--	
--	--	--	--	--	--	--	--	--	--	--	
--	--	--	--	--	--	--	--	--	--	--	
0.877983	0.873405	0.879236	0.882511	0.874824	0.878301	0.872332	0.85243	0.861604	0.876614	0.877252	

gt JA15-41 Area 1 Garnet Traverse	gt JA15-41 Area 1 Garnet Traverse	gt JA15-41 Area 1 Garnet Traverse	gt JA15-41 Area 1 Garnet Traverse	mu JA15-41 Area 1 Muscovite	mu JA15-41 Area 1 Muscovite	mu JA15-41 Area 1 Muscovite	gt JA15-41 Area 2 Garnet traverse
36.5266	36.4359	36.7788	38.59	46.411	43.2079	44.4458	35.7901
0.0126	0.021011	0.012121	0.022583	0.039008	0.1819	0.003707	0.005279
20.9178	20.7647	20.8898	30.774	34.3853	33.1463	34.1543	20.3772
0.002903	0	0.009814	0.00923	0.012693	0	0.024001	0.032723
34.0857	33.318	33.6791	6.91834	1.57965	1.45567	1.57108	32.7186
5.41782	5.57219	5.86486	0.060565	0	0.004705	0.034493	6.23857
2.4819	2.33919	2.34447	1.00025	1.01879	0.71852	0.45658	2.16352
0	0.016857	0.085775	0	0	0	0.022074	0
0.84091	0.816777	0.823055	0.128352	0.05673	0.047858	0	0.828062
0.01106	0.004092	0.007026	0.411488	0.484648	0.688093	0.523483	0.030049
0.001742	0	0.002699	5.89022	10.4654	10.3384	10.0523	0.017733
0.001561	0.003005	0	0.084121	0.02672	0.027628	0.010747	0.023074
0.055315	0.070672	0.052	0	0.038234	0.053656	0.031005	0.083791
100.33	99.33	100.53	83.87	94.50	89.84	91.31	98.27
-	-	-	-	-	-	-	-
--	--	--	--	--	--	--	--
--	--	--	--	--	--	--	--
--	--	--	--	--	--	--	--
--	--	--	--	0.465146	0.531906	0.658704	--
--	--	--	--	0.809309	0.837311	0.858267	--
0.881321	0.887715	0.887274	0.795059	--	--	--	0.89164

gt JA15-41 Area 2 Garnet traverse	gt JA15-41 Area 2 Garnet traverse	gt JA15-41 Area 2 Garnet traverse	gt JA15-41 Area 2 Garnet traverse	gt JA15-41 Area 2 Garnet traverse	gt JA15-41 Area 2 Garnet traverse	gt JA15-41 Area 2 Garnet traverse	gt JA15-41 Area 2 Garnet traverse	gt JA15-41 Area 2 Garnet traverse	gt JA15-41 Area 2 Garnet traverse	gt JA15-41 Area 2 Garnet traverse	gt JA15-41 Area 2 Garnet traverse
36.1906	36.3907	36.3865	36.2678	36.4858	36.6188	36.4901	36.576	36.525	36.3971	36.3952	
0.014825	0.011967	0.007559	0	0.001762	0.004052	0.00392	0.007431	0.010997	0	0.022605	
20.5986	20.7708	20.8926	20.8206	20.8077	20.6009	20.9593	20.8241	20.7882	20.8537	20.803	
0.010166	0.013464	0.013872	0.006909	0.005865	0.027685	0.010914	0.021884	0.005769	0.019604	0.013918	
32.778	33.4754	33.4014	33.6372	33.7126	33.9341	33.5368	33.9281	33.4571	33.3126	32.845	
6.07011	5.71193	5.38277	4.90772	4.89743	4.80877	4.77599	5.00747	5.37427	5.52774	5.88244	
2.23223	2.34738	2.37012	2.41254	2.63951	2.45731	2.56356	2.5226	2.43565	2.42907	2.30509	
0	0	0	0.000582	0.01967	0	0	0.038703	0.007317	0.022814	0	
0.782236	0.734505	0.754597	0.751514	0.730727	0.742112	0.721852	0.748737	0.773264	0.78232	0.804213	
0.175885	0.0644	0.018241	0.090472	0.006178	0.026277	0.11244	0.07345	0.007228	0	0.043326	
0.05	0.004269	0.006932	0.033712	0.003076	0.006656	0.034733	0.010576	0.001298	0.002716	0.005218	
0.089595	0.019193	0.001284	0.037402	0.00675	0.006684	0.052477	0.028791	0.010317	0	0.001284	
0.028544	0.029857	0.031221	0.047097	0.012614	0	0.076459	0.026107	0.082563	0.018093	0.071902	
98.99	99.56	99.25	98.99	99.32	99.23	99.29	99.80	99.44	99.36	99.16	
-	-	-	-	-	-	-	-	-	-	-	
--	--	--	--	--	--	--	--	--	--	--	
--	--	--	--	--	--	--	--	--	--	--	
--	--	--	--	--	--	--	--	--	--	--	
--	--	--	--	--	--	--	--	--	--	--	
0.887783	0.885792	0.886156	0.884282	0.875322	0.88424	0.8786	0.879962	0.884342	0.882847	0.887759	

gt JA15-41 Area 2 Garnet traverse	gt JA15-41 Area 2 Garnet traverse	gt JA15-41 Area 2 Garnet traverse	mu JA15-41 Area 2 Muscovite	mu JA15-41 Area 2 Muscovite	mu JA15-41 Area 2 Muscovite	sil JA15-41 Area 2 Sillimanite	sil JA15-41 Area 2 Sillimanite	mu JA15-41 Area 3 Muscovite	mu JA15-41 Area 3 Muscovite	mu JA15-41 Area 3 Muscovite
34.9081	34.8737	36.5845	44.7722	45.3973	43.0325	43.2829	44.4077	44.7193	45.2842	44.8121
0.00786	0.001724	0.002581	0.220839	0.143571	0.12163	0.152076	0	0.153185	0.1588	0.277015
20.1885	20.125	20.9451	35.003	34.4085	33.9767	35.5032	36.7395	35.1806	34.4977	35.7491
0.004999	0.014929	0	0.033483	0	0.018962	0.023384	0	0.001768	0.0211	0.038098
31.6295	31.8643	32.0758	1.27199	1.4032	1.50768	0.470473	0.454446	1.32789	1.2527	0.999779
6.42692	6.89519	7.02199	0	0	0.000361	0.00665	0.013039	0.002772	0	0
1.89038	1.90643	2.14336	0.669415	0.831144	0.808692	0.466405	0.225686	0.668553	0.775901	0.4428
0.041256	0	0.002711	0	0	0.016562	0.012678	0	0	0	0
0.768584	0.81693	0.849452	0.045316	0.018896	0.055235	0.131406	0.085039	0.041077	0.026553	0.012477
0.020107	0.018995	0.010071	0.451917	0.505341	0.499398	0.252983	0.07252	0.376025	0.519319	0.571196
0.002118	0.009432	0.012487	10.7666	10.7727	10.415	1.81227	0.087695	10.8189	10.5083	10.5331
0.030327	0.007167	0	0.028599	0.026286	0.025508	0.086716	0.043147	0.022329	0.028106	0.010296
0.091575	0.048529	0	0.049073	0.013457	0.116244	0	0.0333	0	0.011142	0
95.96	96.56	99.65	93.29	93.51	90.54	82.18	82.14	93.31	93.07	93.44
-	-	-	-	-	-	-	-	-	-	-
--	--	--	--	--	--	--	--	--	--	--
--	--	--	--	--	--	--	--	--	--	--
--	--	--	--	--	--	--	--	--	--	--
--	--	--	0.515921	0.486373	0.511168	--	--	0.526974	0.475221	0.558774
--	--	--	0.859416	0.835862	0.825437	--	--	0.856146	0.849677	0.898455
0.902399	0.899315	0.892254	--	--	--	--	--	--	--	--

mu JA15-41 Area 3 Muscovite	sil JA15-41 Area 3 Sillimanite	sil JA15-41 Area 3 Sillimanite	sil JA15-41 Area 3 Sillimanite	pl JA15-41 Area 4 Plag traverse	pl JA15-41 Area 4 Plag traverse	pl JA15-41 Area 4 Plag traverse	pl JA15-41 Area 4 Plag traverse	pl JA15-41 Area 4 Plag traverse	pl JA15-41 Area 4 Plag traverse	pl JA15-41 Area 4 Plag traverse
44.6956	45.32	44.9912	44.7277	63.5401	61.8065	66.9827	63.1675	63.9862	66.6462	66.3399
0.258778	0.508894	0	0.088547	0.010528	0.006147	0.003763	0.008898	0.00171	0.00046	0.002824
34.5887	35.8271	37.7165	36.856	21.2206	22.9671	19.7087	20.5303	22.0411	20.207	20.8198
0.029298	0.036727	0.009866	0.051467	0.023811	0	0.006307	0	0	0.007358	0.009603
1.19728	1.55494	0.150924	0.542246	0.10624	0.154164	0.025538	0.075605	0.079742	0.021211	0.041781
0	0	0	0	0.006125	0	0	0	0	0.001603	0
0.611208	0.648205	0.109181	0.275928	0.143623	0.185173	0.008367	0.09704	0.099242	0.026392	0.104665
0.006465	0	0.028746	0	0	0.006179	0.011164	0	0	0	0
0.007357	0.099818	0.028802	0.053833	0.253073	0.25102	0.1696	0.309543	0.453454	0.085808	0.284236
0.506018	0.046908	0.060816	0.075317	10.4238	9.77101	11.9029	9.92148	10.5721	11.7683	11.3889
10.9174	1.10965	0.050384	0.472215	1.30519	1.72085	0.138565	1.93789	1.15385	0.576837	0.855316
0.010045	0.029639	0.016219	0.070945	0.031002	0.026137	0.011532	0.032192	0.027275	0.017146	0.024595
0.054825	0.015998	0	0	0	0	0	0	0	0	0
92.86	85.18	83.16	83.20	97.06	96.89	98.97	96.07	98.41	99.35	99.87
-	-	-	-	-	-	-	-	-	-	-
--	--	--	--	0.012243	0.012562	0.007753	0.015048	0.021636	0.003888	0.012972
--	--	--	--	0.075182	0.102541	0.007542	0.112166	0.06555	0.031122	0.046476
--	--	--	--	--	--	--	--	--	--	--
0.523518	--	--	--	--	--	--	--	--	--	--
0.868554	--	--	--	--	--	--	--	--	--	--
--	--	--	--	--	--	--	--	--	--	--

pl JA15-41 Area 4 Plag traverse	pl JA15-41 Area 4 Plag traverse	pl JA15-41 Area 4 Plag traverse	pl JA15-41 Area 4 Plag traverse	pl JA15-41 Area 4 Plag traverse	sil JA15-41 Area 4 Sillimanite	sil JA15-41 Area 5 Sillimanite	sil JA15-41 Area 5 Sillimanite	sil JA15-41 Area 5 Sillimanite
62.1237	59.6971	65.9262	62.7204	61.603	43.4028	44.6395	44.5986	44.8421
0	0.01431	0.007099	0.000588	0.003962	0	0	0	0.011077
22.46	23.9635	20.8047	21.438	22.8434	36.9294	37.5909	37.929	37.4796
0	0.025948	0	0	0	0	0.012637	0.032705	0
0.132548	0.093142	0.031771	0.127875	0.113364	0.211662	0.182013	0.203086	0.235065
0.00799	0	0.011151	0	0	0	0	0	0
0.192333	0.074794	0.014639	0.102278	0.082524	0.228024	0.099772	0.168066	0.150659
0	0.022767	0	0.028398	0.038003	0	0.016538	0	0
0.331402	0.352518	0.462589	0.724867	0.474552	0.095324	0.029956	0.074854	0.042323
9.71166	10.0511	11.1379	10.3426	9.38412	0.142437	0.068293	0.111627	0.0713
2.11028	0.406853	0.873658	0.86646	2.01108	0.147517	0.057762	0.119435	0.090858
0.037429	0.059397	0.019792	0.041061	0.048815	0.052438	0.007669	0.025757	0.014339
0	0	0	0	0	0	0.005949	0	0
97.10	94.75	99.29	96.38	96.59	81.20	82.71	83.26	82.93
-	-	-	-	-	-	-	-	-
0.016231	0.018529	0.021359	0.035407	0.023906	--	--	--	--
0.123057	0.025462	0.048029	0.050392	0.120626	--	--	--	--
--	--	--	--	--	--	--	--	--
--	--	--	--	--	--	--	--	--
--	--	--	--	--	--	--	--	--
--	--	--	--	--	--	--	--	--

APPENDIX D: PHASE EQUILIBRIA MODELLING

P-T pseudosections were created using the phase equilibrium modelling program *THERMOCALC* v. 3.37 with the internally consistent thermodynamic dataset of Holland and Powell (2011), ds62. Pseudosections were calculated for the geologically realistic system of MnNCKFMASHTO (MnO–Na₂O–CaO–K₂O–FeO–MgO–Al₂O₃–SiO₂–H₂O–TiO₂–Fe₂O₃). The a-x models used come from White *et al.* (2014) and Powell *et al.* (2014). Bulk compositions obtained using LA-ICP-MS or XRF analysis recalculated to molar oxide percent were used for modelling.

Table 8. Bulk compositions recalculated to molar oxide percent (mol%) used in initial phase diagram calculations

	% JA15-04 All FeO	% JA15-04 33% FeO	% JA15-36 All FeO	% JA15-36 33% FeO
H ₂ O	14.596	15.240	7.892	7.951
SiO ₂	56.009	58.478	77.213	77.791
Al ₂ O ₃	9.155	9.558	6.350	6.397
CaO	1.933	2.018	0.175	0.176
MgO	2.235	2.333	2.688	2.708
FeO	12.602	13.157	2.217	2.233
K ₂ O	2.042	2.132	2.515	2.534
Na ₂ O	0.733	0.765	0.707	0.712
TiO ₂	0.633	0.661	0.190	0.191
MnO	0.063	0.065	0.055	0.055
O	0.000	4.408	0.000	0.748

APPENDIX E: STRUCTURAL GEOLOGY

An approximately 5X10km field area (Jebel Ja'alan) was structurally mapped in NE Oman. Structural readings were taken using a compass clinometer and locations were recorded using a Garmin GPS. Maps were constructed in the field using tracing paper over a satellite image of the area, for later use with the software *CorelDRAW X7* to produce the final map.

Stereonet

Stereonet were created for structural data using the *Stereonet 9* program. The program is based on algorithms described by Cardozo and Allmendinger (2013) and Allmendinger *et al.* (2011).

Electronic Map Construction

The electronic version of the study area map was created using *CorelDRAW X7* graphics program. The map constructed in the field was scanned in along with the associated satellite images, and was then traced over using the program.

Cross Sections

N-S and E-W cross sections of the study area were made using obtained structural measurements with the electronic map. The cross sections were initially created by hand on paper and then scanned into a digital form, where they were traced over using the *CorelDRAW X7* graphics program.